

UNIVERSITY OF CALGARY

Assessment of Multi-Fidelity Tools for the Aeropropulsion Analysis of a Small-Scale  
Supersonic Unmanned Aerial Vehicle

by

Vansh Ratna Sharma

A THESIS

SUBMITTED TO THE FACULTY OF GRADUATE STUDIES  
IN PARTIAL FULFILMENT OF THE REQUIREMENTS FOR THE  
DEGREE OF MASTER OF SCIENCE

GRADUATE PROGRAM IN MECHANICAL ENGINEERING

CALGARY, ALBERTA

SEPTEMBER, 2025

© Vansh Ratna Sharma 2025

## **Abstract**

The flight capabilities of a supersonic aircraft is assessed using its aero-propulsive characteristics. A multi-fidelity approach is utilized to evaluate the aeropropulsive behavior of a small-scale supersonic uncrewed aerial vehicle (SSUAV). The multipurpose uncrewed fixed-wing advanced supersonic aircraft (MUFASA), which is being developed by the University of Calgary, is being studied. External aerodynamics and propulsion are studied independently for the development of SSUAVs; this approach does not always provide the best accuracy. A commercial off-the-shelf engine, the AMT Lynx engine, is studied with external aerodynamics integrated using numerical simulations and analytical relations. An analytical formulation was proposed to account for the effect of propulsion on the drag characteristics of the SSUAV. The comparison between propulsion integrated simulations and analytically corrected propulsion has shown limited deviation ( $<10\%$ ), providing a rapid assessment of propulsion effects.

# Preface

This thesis is an original work by the author. No part of this thesis has been previously published.

# Acknowledgements

I would like to express my gratitude to my supervisor, Dr. Craig Johansen, for his support, guidance, and encouragement throughout the course of this research. I would also like to thank the Department of Mechanical and Manufacturing Engineering, University of Calgary, for providing an excellent academic environment and for their invaluable assistance during my studies. Finally, I am deeply grateful to my family for their unwavering love, patience, and moral support. Their belief in me has been my greatest motivation.

# Table of Contents

Abstract	ii
Preface	iii
Acknowledgements	iv
Table of Contents	vii
List of Figures	ix
List of Tables	x
List of Symbols, Abbreviations, and Nomenclature	xi
<b>1 Background and Introduction</b>	<b>1</b>
1.1 Background . . . . .	1
1.2 MUFASA project . . . . .	4
1.3 Research Objective . . . . .	6
<b>2 Literature review</b>	<b>7</b>
2.1 Development of SSUAVs . . . . .	7
2.2 Aerodynamic Modelling . . . . .	9
2.2.1 Drag modeling . . . . .	11
2.2.2 Lift modeling . . . . .	12
2.3 Propulsion Modelling . . . . .	14
2.4 Air Intake Modeling . . . . .	15
2.5 Full Vehicle Simulation . . . . .	16
2.6 Trajectory optimization . . . . .	17
2.7 CFD for supersonic aircraft . . . . .	18
2.7.1 Euler Simulations . . . . .	18
2.7.2 Turbulence . . . . .	19
2.7.3 Reynolds Average Navier Stokes . . . . .	20
2.7.4 Solvers . . . . .	21
2.7.5 Summary . . . . .	22

<b>3</b>	<b>Analytical Propulsion Model</b>	<b>23</b>
3.1	Thermophysical Modeling . . . . .	23
3.2	Propulsion . . . . .	24
3.2.1	Freestream . . . . .	25
3.2.2	UAV intake . . . . .	25
3.2.3	Fanno flow . . . . .	26
3.2.4	Engine cycle . . . . .	26
3.2.5	Back pressure solution . . . . .	29
3.3	Drag corrections . . . . .	31
3.3.1	Air-intake . . . . .	31
3.3.2	Exhaust . . . . .	33
3.3.3	Top speed and stable angle . . . . .	33
3.4	Summary . . . . .	34
<b>4</b>	<b>CFD Model</b>	<b>35</b>
4.1	Geometry . . . . .	35
4.2	Mesh Generation . . . . .	36
4.3	Domain and Boundary conditions . . . . .	38
4.4	Solvers . . . . .	40
4.5	Discretization . . . . .	42
4.5.1	Temporal Discretization . . . . .	42
4.5.2	Gradient Discretization . . . . .	43
4.5.3	Convective Discretization . . . . .	43
4.5.4	Interpolation Schemes . . . . .	45
4.5.5	Laplacian Discretization . . . . .	46
4.6	Turbulence modelling . . . . .	46
4.7	Linear solver . . . . .	48
4.8	Temporal convergence . . . . .	48
4.9	Errors . . . . .	48
4.9.1	Grid uncertainty . . . . .	48
4.10	Summary . . . . .	50
<b>5</b>	<b>Results</b>	<b>52</b>
5.1	Effect of angle of attack on integral aerodynamic quantities . . . . .	53
5.1.1	Drag . . . . .	53
5.1.2	Lift . . . . .	55
5.2	Effects of Configuration on Integral Quantities . . . . .	57
5.2.1	Lift . . . . .	57
5.2.2	Drag . . . . .	64
5.3	Exhaust Correction . . . . .	66
5.4	Intake Correction . . . . .	66
5.4.1	Engine Thrust . . . . .	72
5.4.2	Top Speed and stable flight . . . . .	73
5.5	Summary . . . . .	74
<b>6</b>	<b>Conclusions and Recommendations</b>	<b>75</b>

<b>A Force Calculation</b>	<b>86</b>
A.1 Lift and Drag . . . . .	87
A.2 Aerodynamic Coefficients . . . . .	87
<b>B Fanno flow</b>	<b>89</b>
<b>C Normal Shock Relations</b>	<b>90</b>

# List of Figures

1.1	Development of supersonic flight. Reproduced from (Henne, 2003) . . . . .	2
1.2	MUFASA B. Adapted from(Fyfe, 2025) . . . . .	4
2.1	SSUAV airframes from various R&D programs. . . . .	10
2.2	Lift behavior in compressible region, adapted from (Vos & Farokhi, 2015) . .	13
3.1	Propulsion modeling procedure . . . . .	25
3.2	Back pressure calculation . . . . .	30
3.3	Nosecone Drag correction . . . . .	32
3.4	Exhaust correction . . . . .	33
4.1	MUFASA geometries . . . . .	36
4.2	Fine mesh MUFASA B.1 . . . . .	37
4.3	Computational Domain . . . . .	38
4.4	Boundary conditions on the UAV . . . . .	39
4.5	PIMPLE algorithm. Adapted from (M. V. Kraposhin et al., 2018) . . . . .	41
4.6	Computational cell for finite volume discretization for KNP scheme. Repro- duced from (Lastiwka et al., 2022) . . . . .	44
5.1	Drag coefficient values across Mach numbers (a) $B_1$ (b) $B_2$ (c) $B_3$ . . . . .	54
5.2	Lift coefficient values across Mach numbers (a) $B_1$ (b) $B_2$ (c) $B_3$ . . . . .	56
5.3	Comparison of lift between configurations . . . . .	57
5.4	$M = 0.8$ (a) Pressure plot over boat tail (b) Streamlines for $B_2$ (c) Streamlines for $B_3$ . . . . .	59
5.5	$M = 1.2$ (a) Pressure plot over boat tail (b) Streamlines for $B_2$ (c) Streamlines for $B_3$ . . . . .	59
5.6	$M = 1.5$ (a) Pressure plot over boat tail (b) Streamlines for $B_2$ (c) Streamlines for $B_3$ . . . . .	60
5.7	Wing cross section along the root chord for pressure plots . . . . .	61
5.8	Pressure plot over span $x/c = 0.2$ (a) $M = 0.8$ (b) $M = 1.2$ (c) $M = 1.5$ . . .	62
5.9	Pressure plot over span $x/c = 0.4$ (a) $M = 0.8$ (b) $M = 1.2$ (c) $M = 1.5$ . . .	63
5.10	Pressure plot over span $x/c = 0.8$ (a) $M = 0.8$ (b) $M = 1.2$ (c) $M = 1.5$ . . .	63
5.11	Pressure plot over span $x/c = 0.9$ (a) $M = 0.8$ (b) $M = 1.2$ (c) $M = 1.5$ . . .	64
5.12	Comparison of drag between configurations . . . . .	65
5.13	Pressure contours $M = 0.9$ (a) $B_1$ (b) $B_3$ . . . . .	65
5.14	Comparison of drag between $B_3$ , $B_4$ and $B_2$ . . . . .	67
5.15	Drag comparison between $B_1$ , $B_3$ and $B_5$ . . . . .	68
5.16	Comparison of analytical vs CFD computed pressure plot on intake lip, $M = 0.9$	69

5.17	Stagnation point and spillage for $M=0.9$ . . . . .	70
5.18	Pressure contours for $M = 0.9$ . . . . .	70
5.19	Comparison of analytical vs CFD computed pressure plot on intake lip, $M=1.5$	72
5.20	Comparison between analytical and CFD computed thrust . . . . .	73
A.1	Aerodynamic force calculation. Reproduced from (Anderson, 2011). . . . .	86
A.2	Force resolution for Drag and Lift adapted from (Anderson, 2011), . . . . .	87
C.1	Normal shock wave. Reproduced from (Moura & Rosa, 2013) . . . . .	90

# List of Tables

1.1	MUFASA versions, adapted from (Garcia et al., 2024) . . . . .	5
3.1	Specific heat coefficients . . . . .	24
3.2	AMT Lynx engine coefficients . . . . .	26
4.1	Boundary conditions, all the quantities are in SI units . . . . .	40
4.2	Verification and validation cases . . . . .	42
4.3	$k - \omega$ SST coefficients . . . . .	48
4.4	Refinement levels . . . . .	50
4.5	Grid convergence index . . . . .	50
5.1	MUFASA B.1, configurations simulated using high-fidelity CFD and corrected using low-fidelity analytical method . . . . .	53
5.2	Lift force on different SSUAV components for $B_2$ and $B_3$ configuration . . . . .	58
5.3	Top speed and stable angle . . . . .	73

# List of Symbols, Abbreviations, and Nomenclature

Symbol	Definition
$()_f$	Face value
$A$	Cell face area
$C_p$	Heat capacity at constant pressure
$C_v$	Heat capacity at constant volume
$F_s$	Factor of safety
$M$	Mach number
$P$	Pressure
$Pr$	Prandtl number
$R$	Gas constant
$Re$	Reynolds number
$T$	Temperature
$V$	Volume of a cell
$c$	Speed of sound
$f$	Friction factor
$h$	Specific enthalpy
$k$	Turbulent kinetic energy
$m$	Mass
$p$	Observed order of mesh convergence

$r$	Mesh refinement ratio
$t$	Time
$u$	Specific internal energy
$u$	Velocity
$w$	Work
$y_+$	Non-dimensional wall distance
$\Gamma$	Temperature ratio
$e$	Polytropic efficiency
$D_h$	Hydraulic Diameter
$\gamma$	Ratio of specific heats
$S_k$	Turbulent kinetic energy source term
$S_\omega$	Specific dissipation rate source term
$\alpha_t$	Kinematic turbulent thermal conductivity
$Q_{fuel}$	Heating Value
$S$	Invariant measure of the strain rate

## Abbreviations

## Definition

EDC

Electric Ducted Fan

CFL

Courant-Friedrichs-Lewy number

# Chapter 1

## Background and Introduction

### 1.1 Background

Supersonic transportation has been one of the major developments in aviation in the twentieth century. The first flight of X-1 in 1947 was one of the major starting points for the development of supersonic transportation. Currently, military and civilian developments for such flight vehicles are in progress. Initially, B2707 from the US Supersonic Transport Program (SST), Russia's Tu-144, and the British / French Concorde were the first attempts at civil supersonic transportation (Figure 1.1). In 1971, the U.S SST program was canceled due to economic and environmental issues. Although Tu-144 was the first of the three programs to attain supersonic flight, due to issues similar to those of the B2707, such as rising costs and technical challenges, the program was stopped in 1983. Concorde, on the other hand, was a smaller and slower aircraft compared to Tu-144 and took its first flight in 1969. The program was in operation until 2003 before its cancellation. One of the most challenging aspects observed in previous programs for supersonic transportation has been minimizing the boom supersonic signature while designing.

Interactive inverse design optimization and computational fluid dynamics (CFD) have been the main tools utilized to study these signatures (Ishikawa et al., 2008). Implementing multiple approaches, such as analytical models and CFD, these low-boom supersonic aircraft can be designed more accurately than the low-fidelity inverse design approach (Li et al.,

2010). These methods have contributed to the renewed development of supersonic transport. Aircraft components such as wings and fuselage can be optimized for longer range and higher altitude. For high-speed vehicles, swept delta wings are generally considered due to their low wave drag (R. T. Jones, 1956). Although fuselage design is highly dependent on payload and engine size, smoother shapes are generally considered to reduce pressure drag for high speeds. Many supersonic aircraft tend to have a tailless configuration, like the X-31 and X-36. Due to better controllability, the vertical tail tends to be a better choice for high-speed vehicles.

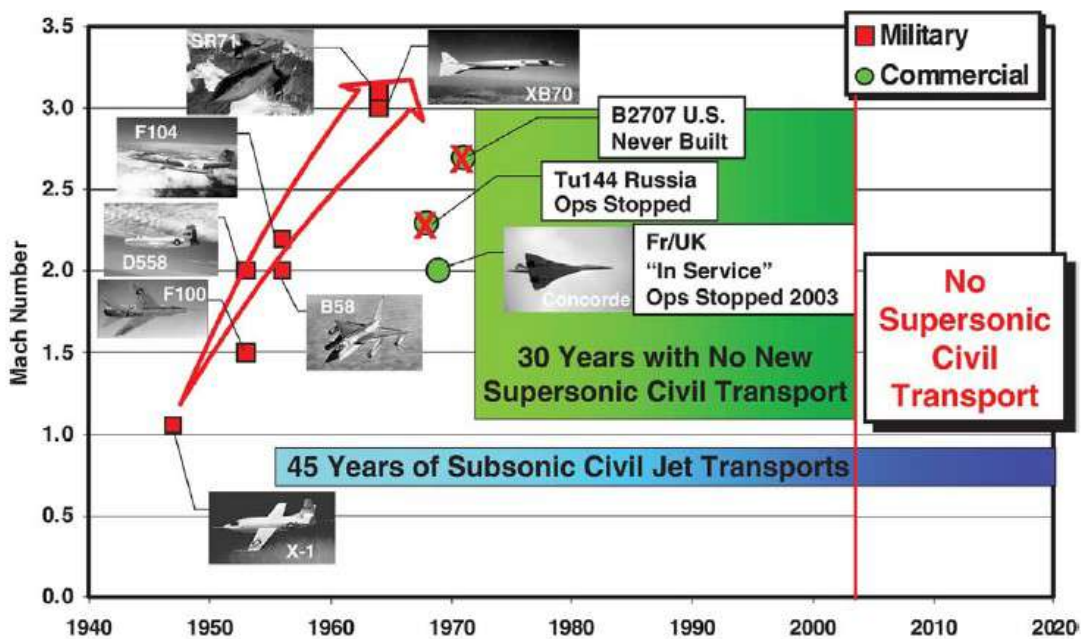


Figure 1.1: Development of supersonic flight. Reproduced from (Henne, 2003)

In recent decades, unmanned aerial vehicles (UAVs) have been an important area of research for various uses, including military and civilian applications. Due to their low development cost compared to civil transportation aircrafts, they have been widely used for scientific purposes (Cai et al., 2014; Hassanalian & Abdelkefi, 2017). The endurance of such vehicles can be up to 48 hours, with cruise speeds ranging from subsonic to supersonic speeds. In recent years, the development of small-scale UAVs is increasing for civil application, in areas such as geological surveys, fire detection, and aerial monitoring. Since the application

of such UAVs requires a range of altitude and monitoring time, the design is also required to meet certain criteria for its range of application with low development cost.

The development of small-scale UAVs was initiated in Japan in the early 2000s (Ohnuki et al., 2006; Yoshida et al., 2002). Experimental flights were conducted to study the challenges related to the design of the high-speed UAV. Various programs have been initiated by universities and research organizations, independently and jointly, to study the aerodynamics of supersonic UAVs (Livne & Nelson, 2012; Nelson et al., 2022; Walter & Starkey, 2012). These programs evaluated the handling of such UAVs at low and high speeds to advance development and improve overall performance by optimizing fuel consumption, and maximizing range and altitude. Engines used in these high-speed configurations are generally ramjets and turbojet engines for subsonic and supersonic configurations. Depending on the cruise Mach number, the air intake is designed to maximize the suction rate from the freestream to achieve the maximum efficiency of the engine for different modes of operation (Meerts et al., 2011).

A challenging aspect of supersonic vehicles is the overall aeropropulsive performance of the vehicle. This includes the drag contribution due to the propulsive system utilized. Propulsion systems can be placed at various locations in a UAV. Many UAVs are designed with integrated propulsion systems within the airframe (Barbosa et al., 2014; Walter & Starkey, 2012), as an alternative to engines placed on the wing. These integrated propulsion systems reduce the frontal area of the aircraft, hence reducing drag. But the challenge with such a design is that the flow can be affected by the propulsion system. Propulsion systems can be modeled separately using various codes (S. M. Jones, 2007; Litt, 2018). Similarly, external aerodynamics can be modeled with a forebody geometry such as a nose cone or pitot intake without accounting for propulsion (Dalman, 2021; Durante, 2023). The two independent approaches are combined in a framework to analyze the overall performance of the UAV. The combined effect of these two phenomena is not modeled in most of the previous UAV research.

## 1.2 MUFASA project

The Multipurpose Uncrewed Fixed-wing Advanced Supersonic Aircraft (MUFASA) project is a collaborative work between the University of Calgary and Atlantis Research Labs Inc. (ARL) to design and test an SSUAV, which will be propelled by a novel ramjet engine. Furthermore, various methods have been utilized to analyze the design problems of such geometries during subsonic/supersonic flight. Numerical tools such as the vortex lattice method (VLM) and analytical software such as Stanford's SUAVE were used by Dalman (2021) to analyze UAV design. Similarly, Stoldt (2021) used CFD to analyze the behavior of the delta wing in the supersonic regime. Various iterations of the design have been in development since the beginning of the project (Table 1.1). The current work focuses on the MUFASA B.1 configuration, which was introduced by Garcia et al. (2024) and was further studied by Fyfe (2025). The MUFASA B.1 geometry is shown in Figure 1.2.

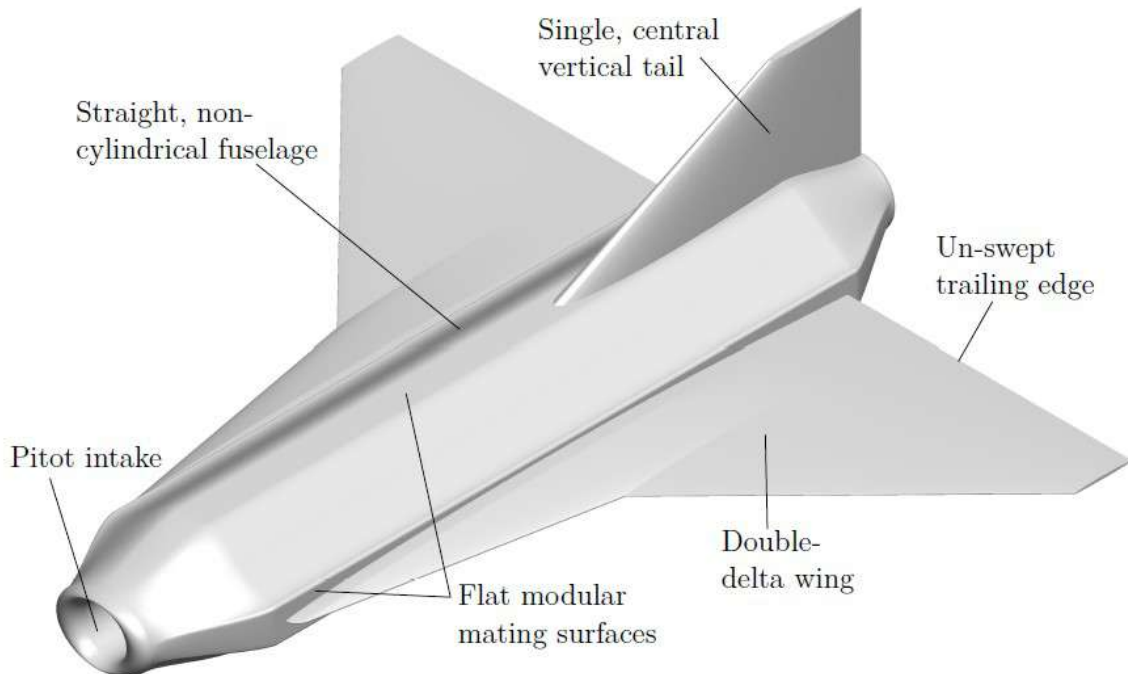


Figure 1.2: MUFASA B. Adapted from(Fyfe, 2025)

Table 1.1: MUFASA versions, adapted from (Garcia et al., 2024)

Version	Description
MUFASA A	Aerodynamic shape evaluated for scale/feasibility (Dalman, 2021)
MUFASA A.1	0.62-scale low-speed demonstrator, sub-2.5 kg, EDF power, flight tested by (Gair, 2023)
MUFASA A.2	1.0-scale, aluminum airframe, 25 kg maximum, evaluated in a flight dynamics model by (Durante, 2023)
MUFASA B	Aerodynamic and configuration improvements (Garcia et al., 2024)
MUFASA B.1	Low-speed demonstrator, sub-4.0 kg, EDF power, under evaluation in the current work (2024-2025)

Preliminary research for the MUFASA B.1 geometry has been in the incompressible regime with a high-fidelity CFD approach and turbulence taken into account (Garcia et al., 2024). Its transonic/supersonic capabilities have not been analyzed yet; with current numerical capabilities, a full vehicle analysis using a high-fidelity approach can be considered, including turbulence.

Previous studies for 3D steady compressible flow simulation using SU2 for the MUFASA A geometry were completed with Euler/Inviscid formulation with a modeled nose cone, instead of an intake. Since the design of the UAV requires a pitot intake system, accurate propulsion modeling is important for its development. The aircraft scaling performed by Dalman (2021), suggested that the AMT lynx is a good choice for supersonic transport; therefore, the AMT lynx was chosen for the MUFASA geometry. Computationally, high-fidelity CFD simulations are substantially more expensive than VLM and low-fidelity analytical methods. The choice of any method to study the performance of the SSUAV is subject to the optimizing time and accuracy.

To increase the efficiency of obtaining accurate results with minimum computations, various analytical models can be added to high-fidelity CFD simulations of a simpler geometry. Correct for a specific phenomenon, which generally produces errors when modeled separately. Different engines need to be tested, conducting simulations for all engines is an enormous task and will take more computational resources than are available. Hence, generally the propulsion system is modeled as a separate entity, and the external aerodynamics are calculated using CFD, or using low-fidelity analytical relations, and medium-fidelity methods such as VLM, and the forces are added in respective directions. This modeling approach or

framework has been used for the past decades, but investigation is required to fully evaluate how accurately this framework estimates lift and drag values when applied to an aircraft with a pitot intake, as this will be essential for analyzing the MUFASA airframe. Various software, such as SUAVE, models the UAV as a solid surface with either a pass-through tube or a nose cone. But in reality, the propulsion engine produces a back pressure that affects the flow field around the front end of the UAV. This is not captured by separately modeling external aerodynamics and propulsion. In addition, instead of the exhaust of the engine, a solid surface was modeled in previous studies.

### **1.3 Research Objective**

The previous section highlighted certain research questions that require further investigation to analyze the aeropropulsive performance of the SSUAV using high-fidelity simulations. The main objectives of this study are:

1. To evaluate engine performance in real flight conditions, using high-fidelity CFD simulation including air intake, internal ducting, and exhaust plume.
2. To reproduce the low-fidelity geometrical assumptions, with the air-intake replaced with a nosecone, the capped nozzle is modeled independently with analytical 1-D code.
3. Perform CFD simulations of two different aeropropulsive variations, forebody geometry/air-intake system, and capped/uncapped nozzle configuration. Furthermore, quantifying the differences between the two variations on the basis of the SSUAV aeropropulsive performance.

## Chapter 2

# Literature review

The chapter reviews the state-of-the-art on the modeling of SSUAVs using various methodologies. Aerodynamic and propulsion modeling using various tools such as CFD and low-fidelity analytical methods. The aerodynamic analysis of the SSUAV, or general wing-body geometry, needs high-fidelity data.

### 2.1 Development of SSUAVs

The development of small-scale UAVs requires rigorous testing for development; hence large-scale facilities both for numerical and experimental research is required. Various programs between research laboratories and university laboratories jointly work on the design and development of small-scale UAVs. The first SSUAV flight tests were initiated in 2006 by Japan's National EXperimental Supersonic Transport (NEXST-1) in Australia with design and testing beginning in 2001 (Ohnuki et al., 2006). Concurrently, the NEXST-2 project was in the testing phase, and a CFD-based inverse design method was used to analyze the natural laminar wing design of the airplane (Yoshida et al., 2002). Ishikawa et al. (2008) also conducted validation studies for flight tests using the Tohoku University Aerodynamic Simulation: TAS and Unified Platform for Aerospace Computation Simulation: UPACS CFD codes. The simulations also account for the effect of additional parts as well as aeroelastic deformation. The NEXST-1 was a larger and heavier airplane and was not suitable for all

operations. The NEXST-1 did not include an air intake engine, but was flown with rocket boosters.

The Drop test for the Simplified Evaluation of Nonsymmetrically Distributed Sonic Boom (D-SEND), another program initiated by JAXA, consisted of two tests at 30 km altitude, to understand the low-boom supersonic signature for design analysis (Honda et al., 2016; Suzuki & Ninomiya, 2018). Simulation and wind tunnel data cannot generally be compared for such geometries due to uncertainty in measurements; therefore, the noisy input Gaussian process (NIGP) was conducted on the D-SEND simulation data to add confidence intervals for comparison (Karino et al., 2020). D-SEND2 was the subsequent iteration of the initial aircraft. Using aerodynamic coefficients and flight test results, in-house developed mathematical models were used for modeling guidance and control systems (Kawaguchi et al., 2017).

Subsequently, the University of Colorado Boulder designed an SSUAV for a 50 kg category with a design speed of Mach 1.4, referred to as GOJETT (Graduate Organization Jet Engine Technology Team)(Walter & Starkey, 2012). The purpose of the development of the GOJETT was to have a design that can be used as a flight test bed for various research projects, such as sonic boom minimization and thrust vectoring. A turbojet engine was used for numerical simulations, with simulations modeling the AMT Titan, AMT Olympus, and AT-450 which are all commercial off the shelf (COTS) engines.

Another vertically-tailed equipped UAV for supersonic transport was designed at NASA and the University of Washington (Ting et al., 2022). The Supersonic Configurations at Low Speeds (SCALOS) was a joint project with the research groups of the University of Washington, the University of Michigan, Stanford University, and the Boeing Research and Technology Department (Nelson et al., 2022). This program was under NASA to provide further developments in flight handling qualities and noise challenges in low supersonic speeds. Initial tests were conducted for low speed stability (Guimarães et al., 2021; Mavriplis et al., 2022; Seraj & Martins, 2022; Ting et al., 2022).

Simultaneously, low-speed research on Research-focused Uninhibited Aerial Vehicle (R-

UAV) at the University of Washington was conducted as a capstone project (Livne & Nelson, 2012). This is similar in design to supersonic business jets such as Concorde and Tu-144, and was scaled down to  $\frac{1}{16}$  in size. The research was mainly focused on the control and stability of the UAV at low speeds (Langston, 2015; Langston et al., 2016).

The development in the respective programs is a combination of air-breathing propulsion integrated within the fuselage, or an engine nacelle integrated outside the UAV. Pohox, developed by Barbosa et al. (2014), is another SSUAV weighing 15 kg with an integrated air-propulsion system within the fuselage. The SSUAV was utilized to validate the existing analysis tools and was used as a flying test bed. Air-breathing UAVs have a significant advantage over rocket-type engine UAVs due to longer endurance. SSUAVs with air-breathing propulsion are generally modeled by separating the external aerodynamics and the propulsion system (Walter & Starkey, 2012). Various projects are represented in Figure 2.1, comprising the design of UAV with and without air-breathing propulsion systems. Many of the UAV designs of these programs do not incorporate an integrated propulsion, perhaps to keep the fuselage thin, and hence, the propulsion systems affect the flow differently. However, the effect of propulsion on flow is not considered.

## 2.2 Aerodynamic Modelling

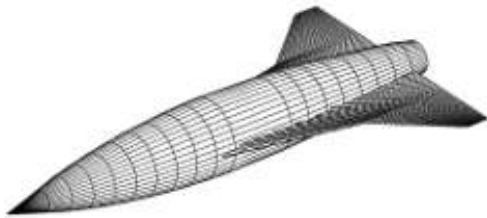
SSUAVs are generally designed to work in the transonic/supersonic regime. The modeling and design of such vehicles traditionally required wind tunnel experiments. Recent developments in computational algorithms, such as VLM and CFD, have provided good accuracy compared to other low-fidelity methods such as the Data Compendium (DATCOM) and VS-PAERO (Atik et al., 2008; Dalman, 2021). A major design challenge for supersonic aircrafts, regardless of their scale, is their drag and lift behavior.



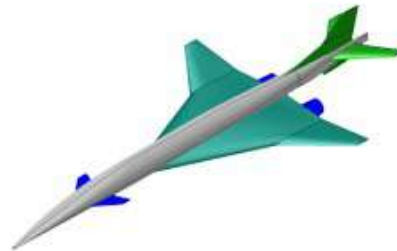
(a) NEXST-1. Adapted from (Ohnuki et al., 2006)



(b) D-SEND. Adapted from (Honda et al., 2016)



(c) GOJETT. Adapted from (Walter & Starkey, 2012)



(d) SCALOS. Adapted from (Wiersema et al., 2025)



(e) Pohox. Adapted from (Barbosa et al., 2014)

Figure 2.1: SSUAV airframes from various R&D programs.

### 2.2.1 Drag modeling

The drag force comprises two components: 1) pressure drag and 2) viscous drag (Anderson, 2011). Analytical formulations have shown that drag increases with the Mach number for a wing-body configuration and peaks near Mach 1, due to an increase in wave drag and the formation of shocks (R. T. Jones, 1956; Whitcomb, 1956). The rise in drag below freestream sonic Mach number occurs specifically when the local Mach number exceeds the speed of sound, leading to the formation of a shock wave. This is due to an effect known as drag divergence, which begins to occur when the slope of the drag coefficient versus Mach exceeds 0.1 (Vos & Farokhi, 2015).

The drag is also affected by the lift when the angle of attack is not zero. This is marked as lift-induced drag and is observed in wings (Clancy, 1975). This additional term in the total drag force increases proportionally with the square of the lift and is inversely proportional to its aspect ratio. Hence, a larger aspect ratio is preferred for higher speeds because of a lesser induced drag. Flow separation is another cause of the increase in drag that occurs at low and high speeds (Vos & Farokhi, 2015). This phenomenon occurs when an adverse pressure gradient, detaches the flow from the surface of an aircraft. The wings are usually design to prevent such separations at high angle of attack using various design approaches (Anderson, 2011).

Another important component that contributes to drag for an aircraft is the forebody geometry, such as the rocket nosecone or air-breathing inlets. The development of early supersonic aircraft involved the optimization of the nose cone for drag minimization by varying the length-to-diameter ratio and geometric profile. The further development of air-breathing systems, replacing the use of rocket engines, resulted in lower design Mach numbers due to losses at air-intake inlets (Raymer, 2012).

Modeling for drag by approximating and using a low-fidelity approach can help in rapid predictions for design using geometric characteristics of individual components. Various methods, including analytical equations as a function of the Reynolds number and Mach number, can be used to derive pressure drag relations (Polhamus, 1953). For viscous drag,

a similar approach can be utilized. Some widely used tools for drag calculation incorporate the use of panel methods based on potential flow theory. DATCOM, developed by the United States Air Force (USAF), is among the widely used software for missiles and aircraft geometries using analytical methods. The drawbacks related to such low-fidelity analytical methods are poor prediction at high angles of attack, even for slender bodies (Devan et al., 1979). The drag computation using DATCOM is inaccurate for the transonic regime, even for low angles of attack for complex geometries such as aircrafts, compared to higher-fidelity methods such as CFD or panel Methods (Ghoreyshi et al., 2009).

Another widely used software is OpenVSP, which uses both medium-fidelity VLM and low-fidelity analytical relations such as VSPAERO, but the error between medium-fidelity and high-fidelity OpenVSP solutions such as CFD for drag can be up to 20% (Dalman, 2021). The further utilization of panel methods for aerospace geometries such as delta wings and aircraft in subsonic and supersonic regimes was increasing due to computational efficiency (Levin & Katz, 1981; Soban et al., 1995). Codes such as the Athena Vortex Lattice (AVL) and Panel Aerodynamics (PANAIR) are considered higher-order panel methods, adding non-linearity for the supersonic regime. These panel methods perform poorly in the transonic regime, similar to analytical methods. The panel and analytical methods are still inaccurate due to not accounting for friction effects. The low and medium fidelity methods are useful for external aerodynamics of a solid body because of the rapid prediction capabilities.

### **2.2.2 Lift modeling**

Calculating the lift force for lift-generating surfaces such as wings and airfoils has been developing since the early 20th century. The lift force is directly related to the difference in pressure between the top and bottom surfaces of the lift generating body (Anderson, 2011). Earlier development in analytical formulations to calculate the lift force was driven by potential flow theory. Prandtl's lifting line theory provides a good analytical method for lifting calculations for incompressible flow around thin airfoils (Prandtl, 1920). Furthermore, compressibility corrections for subsonic flow were added to the existing lifting line theory by

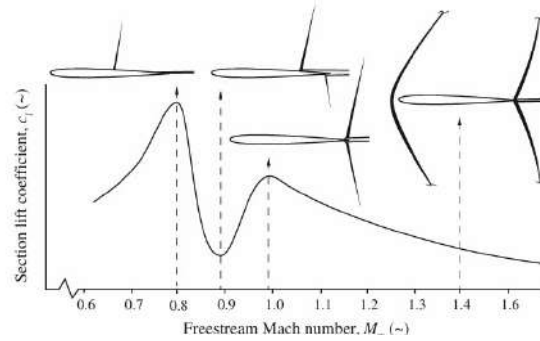


Figure 2.2: Lift behavior in compressible region, adapted from (Vos & Farokhi, 2015)

Glauert (1928) for Mach numbers up to 0.7. These analytical methods did not account for supersonic effects; further development in models provided better accuracy with experimental results for supersonic conditions. The lifting surface generally comprises delta or double delta wings with supercritical or NACA-6 series airfoil sections for supersonic aircrafts, which have shown better lift values across Mach numbers (Vos & Farokhi, 2015). The lift values generally increase with increasing Mach number. However, because of shock waves forming on the wing, a loss in lift is observed near transonic Mach numbers. Post Mach 1, a steady reduction and lift is observed as the Mach number increases, as shown in Figure 2.2.

Initially, single delta wings were analyzed using experimental methods (Lee & Ho, 1990). Separate shear forms a vortex sheet on the delta wing that produces a lower static pressure on the top surface of the wing (Lee & Ho, 1990). In addition to nonswept wings, swept delta wings have been studied by Campbell (1976), observing the limitations of the previous analytical formulation by Polhamus (1971) due to vortex breakdown. Although analytical tools have been widely used, numerical approaches like CFD have shown better accuracy for high angles of attack for such wings (Dalman, 2021). Euler simulations provide better approximations compared to analytical methods, with lower computational costs compared to viscous CFD simulations. However, viscous effects tend to become more dominant at high angles of attack because of flow separations not well predicted by Euler simulations. For such flows, Reynolds Averaged Navier Stokes (RANS) simulations are still preferred (Barton & Pulliam, 1986).

## 2.3 Propulsion Modelling

Propulsion systems for supersonic travel typically use reaction-type engines, which operate according to Newton's third law: By ejecting a small mass of combustion products at high speed, they generate an equal and opposite force that propels the aircraft forward. The first successful supersonic flight, achieved by the X-1, utilized a rocket engine, a type of reaction engine that lacks an air intake.

To extend the range and endurance of supersonic flight, subsequently the development of turbojet and turbofan engines was made. A typical turbojet engine includes an air intake, diffuser, compressor, combustion chamber, and nozzle (Farokhi, 2014). Some configurations also incorporate an afterburner to provide additional thrust. The thermodynamic behavior of the engine is commonly modeled using the Brayton cycle, which consists of two nearly isentropic processes and two processes of constant pressure.

Turbofan engines represent a significant improvement over traditional turbojets by adding a ducted fan, which increases the mass of air moved through the engine and enhances thrust efficiency. In addition, extensive research has been conducted on optimizing individual engine components to further improve overall system performance and efficiency. NASA's Toolbox for the Modeling and Analysis of Thermodynamic Systems (T-mat) is a numerical code to analyze such cycles (Litt, 2018). Another state-of-the-art numerical tool, Numerical Propulsion System Simulation (NPSS), developed by NASA, is used to efficiently model the engine cycle (S. M. Jones, 2007). Some tools also utilize a gradient-based algorithm in which the states of the coupled engine components are calculated by optimizing an objective function such as fuel consumption (Hearn et al., 2016). Coupling of analytical methods and high-fidelity CFD can also be utilized for propulsion systems. Briones et al. (2021) studied a coupled CFD and a turbojet engine, which allows to perform on- and off-design conditions without turbomachinery maps.

One of the main aspects of the propulsion system is its air intake modeling for subsonic and supersonic flows. Ideally, turbojet engines do not work under supersonic conditions in

the intake tube region; rather, the flow is subsonic ( $M \approx 0.5$ ) at the engine's compressor face (Farokhi, 2014). The air intake designed in such geometries is subjected to free-stream conditions to have the least total pressure loss. Total pressure is lost due to irreversibility across the intake and this loss in total pressure reduces the overall exergy due to an increase in entropy. Since these systems work on thermodynamic principles, various analytical solvers are sufficient for an engine cycle analysis.

## 2.4 Air Intake Modeling

The development of air-breathing engines has made substantial progress in supersonic transport aircraft. For subsonic speeds, modern engines are pretty versatile to work on all Mach numbers without compromising intake performance because of negligible total pressure loss from the freestream to the engine inlet. For supersonic speeds, due to the formation of shock waves, the intake design of these propulsion systems must change to minimize the loss of total pressure from the freestream. Initially, straight diffusers were used for such reaction engines (Kline, 1959). Further improvements in parametrization allowed for the development of curved diffusers for subsonic intakes (Fox & Kline, 1962). For the supersonic regime, diffusers are generally designed to avoid bow shocks. During the Concorde design phase, Rettie and Lewis (1968) conducted tests on different ramp angles of the compression system used for the Concorde. This resulted in an improved intake geometry, which increased the flow of captured mass into the engine and enhanced the pressure distribution on the face of the engine. Another challenge in such intake systems is the formation of oblique shocks within the diffuser. Hence, further methods to suppress the effect of such was necessary for the researchers.

For other propulsion systems, such as ramjets and scramjets, supersonic flow at the diffuser inlet can form shock trains. This phenomenon can further increase total pressure loss, reducing overall performance. Although experiments were the only way to perform analysis on such engines in the early 1970s, development in CFD codes made design and optimization

much simpler due to the axisymmetric nature of such engines. Hence, optimization of intakes using two-dimensional CFD studies for off- and on-design conditions is required for design consideration (Valorani et al., 1999). The design of such intakes for high speeds works by suppressing normal shock formation in the cowl lip to reduce pressure drag (Gounko et al., 2013). The initial design of air intakes may not be the most efficient; therefore, parametric studies on intakes using experimental and numerical data may be useful to find the best design parameters. Soltani et al. (2013) numerically simulated on three different parameters, such as free-flow Mach numbers, back pressure ratio, and spike deflection angle, resulting in reduced drag up to 9% from the base case. Similarly, the work by Sepahi-Younsi and Forouzi Feshalami (2019) using four different parameters shows that increasing the angle of the spike produces a higher drag for external compression intakes and nearly constant for mixed compression and reduces the mass flow rate for both.

Although numerical simulations provide more qualitative insight into the flow, hybrid approaches that use simulations and analytical modeling have been much more efficient in optimizing the intake geometry. Using the wake traverse method, Williams and Stevens (2006) calculated the spillage drag by accounting for the loss of momentum in the propulsion stream tube. Similarly, additional factors can be used to account for the loss of total pressure for supersonic geometries. Bravo-Mosquera et al. (2016) use such an analytical formulation to account for external loss coefficients. This formulation helped to understand the cowl angle for Mach numbers from 1.6 to 2.2, which show the highest pressure losses in the intake.

## **2.5 Full Vehicle Simulation**

Propulsion systems are generally modeled separately for aircraft and UAVs after using various methods to calculate their aerodynamic coefficients. Various frameworks were implemented to integrate the propulsion and aerodynamics of the model and to understand its effect on the trajectory of the UAV or an aircraft (Goulos et al., 2010). Kestner et al. (2012) developed an aircraft mission module using NPSS by entering aircraft assembly parameters with

aerodynamic coefficients, integrating the NPSS capability to simulate a real-time propulsion cycle. Propulsion codes such as NPSS can be integrated separately with various aerodynamic tools, such as X-Plane 11, which can be used for the full simulation of vehicles (Remiger et al., 2024). These modules and frameworks integrate the propulsion and aerodynamic tools, but do not account for the effect the propulsive system has on the flow field. Earlier investigations to observe interference effects due to propulsion systems were performed using experimental methods and Euler simulations (Rossow et al., 1994). Attempts to examine integration effects for aircrafts using viscous simulations were initially made by Lockheed Martin and the Air Force Research Laboratory for Distributed Propulsion (DP) systems. The effect of propulsion systems on external aerodynamics has been shown to be significant, due to a substantial increase in drag compared to the assumption of a geometry of the nacelle-wingbody through passage (Hooker et al., 2013; Wick et al., 2015). An initial study by Hooker et al. (2013) presents the effect on drag by engine integration, showing an increase in drag compared to a clean wing for high subsonic flow. The increase in drag also shows a positive relationship with a higher Mach number.

## 2.6 Trajectory optimization

Optimization of the trajectory of a UAV is one of the most challenging tasks in flight testing and analysis. The goal of an SSUAV is to work in a specific range of altitudes and ranges according to the application. Perez et al. (2008) developed a multidisciplinary design optimization framework to design and analyze the climb and cruise performance of the aircraft geometry, engine, and flight profile using aerodynamic data from the panel method and conducting a zero-dimensional engine analysis. Similarly, using CFD, Elmer et al. (2013) concluded that higher altitude and lower acceleration can reduce the amplitude of the sonic boom. Since lower acceleration is not desired, this optimization directly affects the overall performance and trajectory of the vehicle due to limiting its altitude. Performance can be increased for the climb phase of the supersonic aircraft if heat exchangers are added to the

engine, significantly reducing climb time (Jasa et al., 2018).

Drag reduction is also another challenge for fixed-wing aircraft; therefore, active methods of reducing drag, such as morphing trailing edges, can be used to reduce fuel consumption for non-cruise flight phases (Burdette & Martins, 2019). Langelaan (2007) introduced a simple correlation between drag and the lift coefficient for a two-dimensional system. Using the aerodynamic relation, it calculates the trajectory taking into account the thrust-to-drag margin for small angles of attack. In addition, additional parameters such as wind gusts can be taken into account using various analytical models during soaring. Xu et al. (2023) modeled transverse gusts to observe the effect on wing transients and find optimal wing maneuverability using iterative methods. The framework provided positive results to regulate lift during trapezoidal wing gusts.

Another important metric to analyze for trajectory optimization is its climb fuel efficiency. Leblie et al. (2025) analyzed the climb fuel efficiency, which is the ratio of the total energy gained by the aircraft during the climb phase to the fuel energy used. The climbing trajectory is then optimized by keeping a target speed at the end of the climb phase.

## **2.7 CFD for supersonic aircraft**

CFD is a numerical method to analyze flows for different applications. In the finite-volume approach for CFD, the computational domain is discretized into a collection of small control volumes. The integral forms of the governing conservation equations (mass, momentum, and energy) are applied to each control volume, and the fluxes are evaluated across the shared faces between adjacent volumes to ensure overall conservation throughout the flow field.

### **2.7.1 Euler Simulations**

Euler simulations were initially utilized because of their low computational cost. Turbulence is not modeled in Euler simulations; therefore, flow separations and turbulent eddies are not correctly calculated because of the absence of the shear stress term. Initial attempts were

made to implement Euler simulations in steady state. Artificial dissipation and numerical discretization error produced nonphysical results; this in turn could be prevented by more nodal points for Euler simulations (Koeck, 1985; Rizzi, 1982). For compressible flow discontinuities, such as shocks, special numerical schemes are needed for accuracy. Rizzi and Eriksson (1984) computed unsteady flow simulations specifically for the ONERA M6 wing. The major challenge for transonic flows with Euler simulations was the artificial viscosity modeled by the numerical software. Various researchers conducted additional work using Euler methods, involving supersonic analysis of wings and full aircraft (Jameson & Baker, 1987; Moens & Gardarein, 2001; Schoene et al., 1989). Aerodynamic analysis using Euler simulations was a substantial addition to the state of numerical simulations for aerospace applications. The major difference lies in the drag computation compared with numerical methods that involve turbulence. Goorjian (1988) initially presented upwind differencing algorithms for viscous computations for aerospace applications. This improved accuracy for unsteady flow calculations over transonic wings compared to the central differencing algorithm for both Euler and viscous simulations.

### **2.7.2 Turbulence**

Methods such as Reynolds averaged Navier-Stokes (RANS), large-eddy simulations (LES), and direct numerical simulation (DNS) are some of the techniques used to model turbulence. These methods have significant differences in their strategy and accuracy. Since turbulent flow features work on varying time and length scales, all scales need to be resolved or modeled to minimize errors. The initial attempt at turbulence modeling was by Prandtl (1925), who provided a mixing length model for boundary layers in bounded turbulent flows. This model provided insights into the variation of viscosity normal to the boundary. The further development of such formulations and numerical methods introduced Reynolds stress modeling and RANS. Smagorinsky (1963) proposed a hybrid method for modeling subgrid scales of turbulence and resolving larger scales. Since smaller scales are more computationally expensive to resolve, this method provided a good trade-off between accuracy and computational

cost; hence, this formulation was later used by Deardorff (1970) as LES. Formulations like DNS resolve all the turbulent scales and were first introduced in the 1970s (Orszag, 1970). The DNS method was more accurate but computationally more expensive than the previous two methods; hence, its usage has been limited. Another widely used hybrid approach is Detached Eddy Simulation (DES), which uses the RANS approach for small scales and the LES approach for larger turbulent scales away from the walls. P. R. Spalart (1997) used this hybrid method initially with the Spalart-Allmaras model for RANS formulation. Further development was carried out, and the  $k - \omega$  SST model was also used in this hybrid approach (Squires, 2004).

### 2.7.3 Reynolds Average Navier Stokes

The Reynolds-Averaged Navier–Stokes (RANS) equations are obtained by decomposing the instantaneous flow variables into mean and fluctuating components and applying Reynolds averaging to the Navier–Stokes equations. In engineering practice, RANS is often solved in steady state mode to predict statistically steady mean flows, although it can also be used in unsteady form (URANS) for time-dependent problems. The idea was started by Reynolds (1895) who decomposed the flow properties into time-averaged and fluctuating components. This formulation differs from other formulations like LES and DNS by modeling scales rather than resolving them. The initial attempts to incorporate the RANS methodology improved existing Euler simulations that do not solve for the fluid’s viscosity.

Turbulence in RANS is usually solved by adding an additional set of equations to the already existing mass, momentum, and energy conservation equations. Turbulence is modeled in various ways using different RANS formulations. The initial development was based on the numerical solution of the Reynolds stress equations by Chou (1945) and Rotta (1951). Hanjalić and Launder (1972) introduced algebraic approximations for these equations to model Reynolds stresses. The dissipation term for turbulence was still not modeled well for high-Reynolds-number flows. Although the Reynolds stress model (RSM) was able to solve for turbulence, two-equation models such as  $k - \epsilon$  were introduced in the early 1970s

(W. Jones & Launder, 1972). These models approximate Reynolds stresses by relating them to the mean strain rate through an eddy viscosity, rather than directly solving transport equations for Reynolds stresses. W. Jones and Launder (1972) provided two different formulations for high and low Reynolds numbers and were substantially less expensive to compute compared to the RSM model. The proposed  $k - \epsilon$  model was tested for accelerated boundary layer flows, although more accurate than the RSM model, it overpredicts the length scales near the wall (Squires, 2004). Wilcox (1988) developed a new model,  $k - \omega$ , using the same eddy viscosity approach but improving the formulation of the near-wall region. Furthermore, F. Menter (1993) improved the two-equation model with two variants,  $k - \omega$  BSL and SST. The BSL model was a development on the already existing model by Wilcox (1988), by adding a switch in the formulation from  $k - \omega$  to  $k - \epsilon$  in the outer region of the boundary layer. This provided a better formulation for both regions. Turbulence was widely modeled using various formulations, as it predicted the flow for adverse pressure gradients well, which the Euler equations could not predict (Araya, 2019). However, these formulations required a high number of node points to accurately predict the gradients. For aerospace applications, when geometric models have large dimensions, such large cell counts can, with two additional equations at each cell, contribute to relatively slower computations. Hence, P. Spalart and Allmaras (1992) introduced a one-equation model that directly solves eddy viscosity. The application of such turbulence formulations is limited to the problem and the computational cost incurred. Initial validation and verification of these models were limited to airfoil studies due to their lower computational cost. The  $k - \omega$  SST model has proven to be more reliable for flow separations at high angles of attack. Whereas, the Spalart-Allmaras model produces similar results for weakly attached flow when compared (Araya, 2019).

#### 2.7.4 Solvers

Software such as SU2 and OpenFOAM are some open-source CFD solvers widely preferred for external and internal fluid dynamics. Various methods for solving the Navier-Stokes equations have been formulated in the past several decades. For low speeds (generally lower

than Mach 0.3), the variation in density is negligible; hence, incompressible solvers, which are pressure-based, such as `simpleFoam`, `pimpleFoam`, etc., are widely used for external as well as internal flows. However, for compressible subsonic and supersonic regimes, density- and pressure-based solvers work well (Miettinen & Siikonen, 2015; Singh & Mukhopadhyay, 2023). These solvers are robust for both transient- and steady-state simulations. Among density-based solvers such as `rhoSimpleFoam`, `rhoPimpleFoam`, and `rhoCentralFoam`, the CFL number becomes an important parameter for stability (Stoldt, 2021). However, pressure-based solvers provide more accuracy for higher CFL numbers even for steady-state calculations (Messa, 2018).

### **2.7.5 Summary**

The chapter illustrated various programs that have contributed to the research of design and development of SSUAVs. In addition, various aerodynamic and propulsion components can be studied using various kinds of numerical tools, ranging from low-fidelity analytical methods to high-fidelity numerical simulations. The advancement of numerical schemes for faster and more accurate viscous-flow computations provides a strong basis for simulating UAVs equipped with air-breathing engines and comparing the results with existing low- and medium-fidelity methods. This approach can offer improved information on the integrated aeropropulsive performance of SSUAVs during flight.

## Chapter 3

# Analytical Propulsion Model

This section describes the method used for analytical calculations and the models used for the SSUAV and its components. The propulsion model is developed separately, and values were used at the SSUAV's boundaries to quantify the propulsion system's effects.

### 3.1 Thermophysical Modeling

The working fluid is assumed to be air with a molecular weight of  $28.96 \frac{g}{mol}$ . Ideal-gas law assumptions are made for the working fluid:

$$p = \rho RT \quad (3.1)$$

Thermodynamic calculations for specific heat at constant pressure ( $C_p$ ) and enthalpy ( $h$ ) are calculated using the NASA polynomial coefficient model (Lemmon et al., 2018).

$$\frac{C_p}{R} = a_1 + a_2T + a_3T^2 + a_4T^3 + a_5T^4 \quad (3.2)$$

$$\frac{h}{RT} = a_1 + \frac{a_2T}{2} + \frac{a_3T^2}{3} + \frac{a_4T^3}{4} + \frac{a_5T^4}{5} + \frac{a_6}{T} \quad (3.3)$$

The model assumes two different sets of coefficients for the temperature range 200  $K$  to 1000

$K$  and 1000  $K$  to 3000  $K$  (Lemmon et al., 2018). The coefficients for the calculations are shown in Table 3.1.

Table 3.1: Specific heat coefficients

Temp Range	$a_1$	$a_2$	$a_3$	$a_4$	$a_5$	$a_6$
200 $K$ to 1000 $K$	3.838	$-2.905 \cdot 10^{-3}$	$7.832 \cdot 10^{-6}$	$-7.252 \cdot 10^{-9}$	$2.471 \cdot 10^{-12}$	$4.142 \cdot 10^2$
1000 $K$ to 3000 $K$	2.718	$2.065 \cdot 10^{-3}$	$-1.038 \cdot 10^{-6}$	$2.541 \cdot 10^{-10}$	$-2.424 \cdot 10^{-14}$	$6.252 \cdot 10^2$

The ratio of specific heats ( $\gamma$ ) is calculated:

$$\gamma = \frac{C_p}{C_p - R} \quad (3.4)$$

The dynamic viscosity ( $\mu$ ) is calculated using the Sutherland equation:

$$\mu = 1.458 \cdot 10^{-6} \frac{\sqrt{T}}{T + 110.4} \quad (3.5)$$

The thermal conductivity ( $\kappa$ ) is formulated using the modified Eucken method:

$$\kappa = \mu C_v \left( 1.32 + \frac{1.77R}{C_v} \right) \quad (3.6)$$

## 3.2 Propulsion

The AMT Lynx turbojet engine is simulated in the current work (AMT Netherlands Lynx, 2020). The engine is located 1.8 m from the UAV intake and is connected with a tube equal to the diameter of the engine intake. Fanno flow is modeled between the UAV and the engine intake. After the Fanno flow, the engine cycle represented by components in Figure 3.1, is modeled using analytical relations presented in Section 3.2.4. The force is finally calculated at the end using the combined effect of the change in momentum and pressure at the engine boundaries.

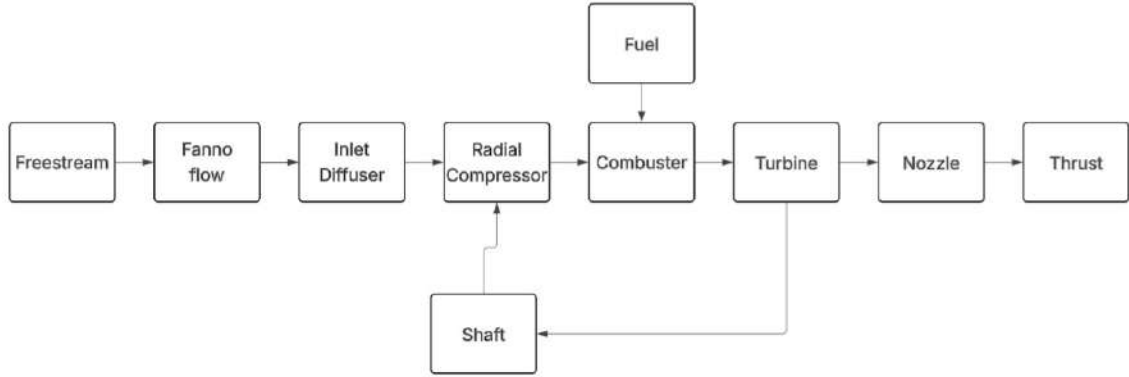


Figure 3.1: Propulsion modeling procedure

### 3.2.1 Freestream

The static properties of the free stream are taken from the US standard atmosphere (Atmosphere, 1976) at an altitude of 11,000 m. For supersonic flow, a normal shock upstream of the pitot intake is included as part of the flow path. Normal shock relations are applied in front of the UAV. The relation for static and stagnation properties before and after the shock wave is presented in Appendix C.

### 3.2.2 UAV intake

The UAV intake is modeled with only total pressure recovery approximations using Farokhi (2014). The total pressure recovery is formulated using:

$$\pi = \frac{P_{t,2}}{P_{t,0}} \quad (3.7)$$

Where,  $P_{t,2}$  and  $P_{t,0}$ , are total pressure after and before the air intake. The Mach number is limited to 0.5 at the compressor face; hence, for supersonic and subsonic flow, the Mach number in the stream tube is subsonic. Hence, the total pressure recovery factor at the UAV intake is kept 0.995.

### 3.2.3 Fanno flow

The first stage of the propulsion model is the Fanno flow in the pitot intake tube between the SSUAV inlet and the engine inlet. This section is developed to calculate the Mach number at the engine inlet. The Fanno flow is used in the study to integrate the total pressure from the free stream to the engine intake. The length of the tube is 1.8 m, which was selected based on the rear end engine size and the dimensions of the SSUAV. The Mach number varies according to Equation 3.8:

$$\frac{4fL}{D_h} = \left( \frac{1 - M^2}{\gamma M^2} \right) + \left( \frac{\gamma + 1}{2\gamma} \right) \ln \left[ \frac{M^2}{\left( \frac{2}{\gamma + 1} \right) \left( 1 + \frac{\gamma - 1}{2} M^2 \right)} \right] \quad (3.8)$$

where  $L$  is the required duct length to choke the flow. The friction factor is formulated using the Colebrook-White equation 3.9:

$$\frac{1}{\sqrt{f}} = -2 \log \left( \frac{\varepsilon}{3.7 D_h} + \frac{2.51}{Re \sqrt{f}} \right) \quad (3.9)$$

where  $\varepsilon$  is the roughness in m and  $Re$  is the Reynolds number of the conduit.

### 3.2.4 Engine cycle

An engine cycle analysis is used to calculate the thermodynamic properties at the engine face. The efficiencies of each component are taken from Farokhi (2014). The engine is modeled analytically using the turbojet Brayton cycle. The efficiencies are adjusted to give the same amount of static thrust at sea level as provided in the AMT Netherlands Lynx (2020). The efficiencies are provided in Table 3.2. The stages of the air-breathing engine integrated UAV is shown in Figure 3.2. The fuel is JP8/Jet A-1 for the current analysis, with a lower heating value assumed from Oates (1985).

Table 3.2: AMT Lynx engine coefficients

$\eta_d$	$\pi_{inlet}$	$\eta_{compressor}$	$\pi_{compressor}$	$\lambda$	$\pi_{combuster}$	$\eta_{turbine}$	$\eta_{mech}$	$\eta_{nozzle}$	$\pi_{nozzle}$	$Q_{fuel}$
1	1	0.8022	4	0.024	0.9	0.9	0.9	1	1	43260 <i>KJ</i>

## Diffuser

The first stage of the turbojet engine is a diffuser. The diffusers in engines are mainly used to decelerate flow to subsonic near Mach 0.5 for higher thrust conditions. For subsonic conditions, normal shock relations are not applied because of the absence of shock. Thus, the equation for the diffuser is as follows:

$$T_{t,2} = T_1 \left(1 + \eta_d \frac{\gamma - 1}{2} M_1^2\right)^{\frac{\gamma-1}{\gamma}} \quad (3.10)$$

$$P_{t,2} = P_1 \left(1 + \frac{\gamma - 1}{2} M_1^2\right)^{\frac{\gamma}{\gamma-1}} \quad (3.11)$$

$$h_{t,2} = C_p T_{t,2} \quad (3.12)$$

## Compressor

The compressor is used to raise the total pressure; this is the first of the four processes in an ideal Brayton cycle. The stagnation/total temperature relations across compressor with an efficiency factor included in the equation:

$$T_{t,3} = T_{t,2} \cdot \Gamma_c \quad (3.13)$$

$$\Gamma_c = \frac{\pi_{compressor}^{\frac{\gamma-1}{\gamma}} - 1}{\eta_{compressor}} + 1 \quad (3.14)$$

$$P_{t,3} = P_{t,2} \cdot \pi_{compressor} \quad (3.15)$$

$$w_{compressor} = h_{t,3} - h_{t,2} \quad (3.16)$$

## Combuster

The fuel for combustion is fed into the engine in the combustion stage. The fuel-to-air ratio  $\lambda = 0.024$  is used at this stage in accordance with the AMT design conditions. Heat addition is modeled across the stage.

$$T_{t,4} = T_{t,3} + \frac{(\eta_t \cdot Q_{fuel} \cdot \lambda)}{C_p(1 + \lambda)} \quad (3.17)$$

$$h_{t,4} = h_{t,3} + \frac{(\eta_t \cdot Q_{fuel} \cdot \lambda)}{(1 + \lambda)} \quad (3.18)$$

$$P_{t,4} = P_{t,3} \cdot \pi_{combuster} \quad (3.19)$$

$$\lambda = \frac{h_{t,4} - h_{t,3}}{\eta_{combuster} Q_{fuel} - h_{t,3}} \quad (3.20)$$

## Turbine

The turbine stage is modeled by the work utilized to run the compressor stage, using equation:

$$\Delta h = h_{t,5} - h_{t,4} = \frac{-w_{compressor}}{\eta_{mech}(1 + \lambda)} \quad (3.21)$$

$$T_{t,5} = h_{t,5}/C_p \quad (3.22)$$

$$T_{t,4} = h_{t,4}/C_p \quad (3.23)$$

$$\Gamma_t = \frac{T_{t,5}}{T_{t,4}} \quad (3.24)$$

$$e_t = \frac{\log(\Gamma_t)}{\log(1 - \frac{1-\Gamma_t}{\eta_{turbine}})} \quad (3.25)$$

$$\pi_{turbine} = \Gamma_t^{\frac{\gamma}{(\gamma-1) \cdot e_t}} \quad (3.26)$$

$$P_{t,5} = P_{t,4} \cdot \pi_{turbine} \quad (3.27)$$

## Nozzle

The nozzle is assumed to be a convergent nozzle with the same dimensions as mentioned in the AMT manual.

$$T_{t,9} = T_{t,5} \cdot \pi_{nozzle}^{\frac{\gamma-1}{\gamma}} \quad (3.28)$$

$$P_{t,9} = P_{t,5} \cdot \pi_{nozzle} \quad (3.29)$$

$$h_{t,9} = C_p T_{t,9} \quad (3.30)$$

## Thrust

Finally, the thrust is calculated using the change in momentum across the engine and the net pressure force acting on the engine using Equation 3.31:

$$F_T = \dot{m}_1 V_1 - \dot{m}_9 V_9 + (P_1 A_1 - P_9 A_9) \quad (3.31)$$

### 3.2.5 Back pressure solution

A five-stage propulsion model was devised using isentropic flow equations for a turbojet engine. Mass conservation was applied at the engine input and the exhaust by applying the Mach 1 condition at the exhaust. The mass flow rate is calculated using:

$$\dot{m} = \frac{AP_t}{\sqrt{T_t}} \sqrt{\frac{\gamma}{R}} M \left(1 + \frac{\gamma-1}{2} M^2\right)^{-\frac{\gamma+1}{2(\gamma-1)}} \quad (3.32)$$

Mass conservation is applied by adding the fuel flow rate to air flow rate from the engine intake.

$$\dot{m}_{inlet}(1 + \lambda) = \dot{m}_{exhaust} \quad (3.33)$$

The area for the inlet and exhaust faces of the engine is taken from the engine dimensions itself. The Mach number is assumed to be 1 at exhaust. Since the ratio of total pressure to static pressure always exceeds the critical pressure ratio during engine operating conditions,

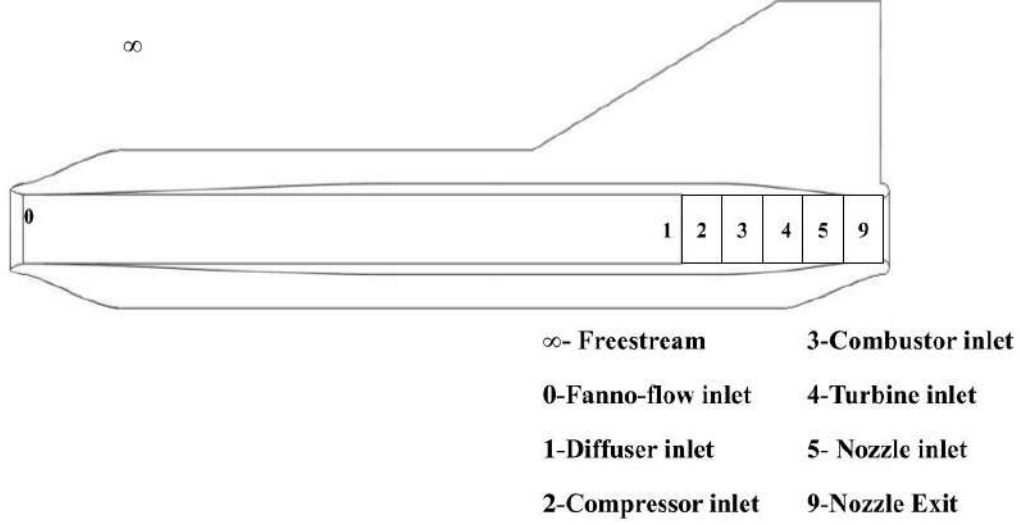


Figure 3.2: Back pressure calculation

this assumption is justified. The total conditions are directly related to both faces of the engine through the engine cycle itself. The total pressure at the UAV intake is calculated using the pressure recovery.

The combined equation is solved for the Mach number using the Fanno flow and sonic conditions at the exhaust. Equation 3.33 shows the mass equivalency in both stages, with subscript 1 representing the intake of the engine and 9 showing the face of exit of the engine. The engine stages used for the equations are shown in Figure 3.2.

$$\frac{A_1 P_{t,1}}{\sqrt{T_{t,1}}} \sqrt{\frac{\gamma_1}{R}} M_1 \left(1 + \frac{\gamma_1 - 1}{2} M_1^2\right)^{-\frac{\gamma_1 + 1}{2(\gamma_1 - 1)}} = \frac{A_9 P_{t,9}}{\sqrt{T_{t,9}}} \sqrt{\frac{\gamma_9}{R}} M_9 \left(1 + \frac{\gamma_9 - 1}{2} M_9^2\right)^{-\frac{\gamma_9 + 1}{2(\gamma_9 - 1)}} \quad (3.34)$$

The engine equations in Section 3.2.4 only use stagnation properties for each component; therefore, the relation between total pressure and total temperature is known on both faces of the engine, with the area on both faces assumed as AMT dimensions. Hence, it reduces to a constant for specific total pressure and temperature values, denoted as  $K$ .

$$M_1 \left(1 + \frac{\gamma_1 - 1}{2} M_1^2\right)^{-\frac{\gamma_1 + 1}{2(\gamma_1 - 1)}} = \frac{A_9}{A_1} K \quad (3.35)$$

The Mach number at the engine inlet becomes independent of total pressure and temperature as the engine utilizes constant efficiencies and pressure ratios. The values of  $K$  change across the freestream Mach numbers, but remain near 0.55 to 0.56.

### 3.3 Drag corrections

Corrections are applied at the exhaust and nosecone to analytically model the independent propulsion system. The nosecone simulations are carried out to obtain external aerodynamics of the UAV, further correcting the forces on the nosecone and exhaust face by adding the forces due to the turbojet engine incorporated. Drag corrections are compared with simulations that incorporate the propulsion model and the back pressure values on the face of the engine intake in Section 5.

#### 3.3.1 Air-intake

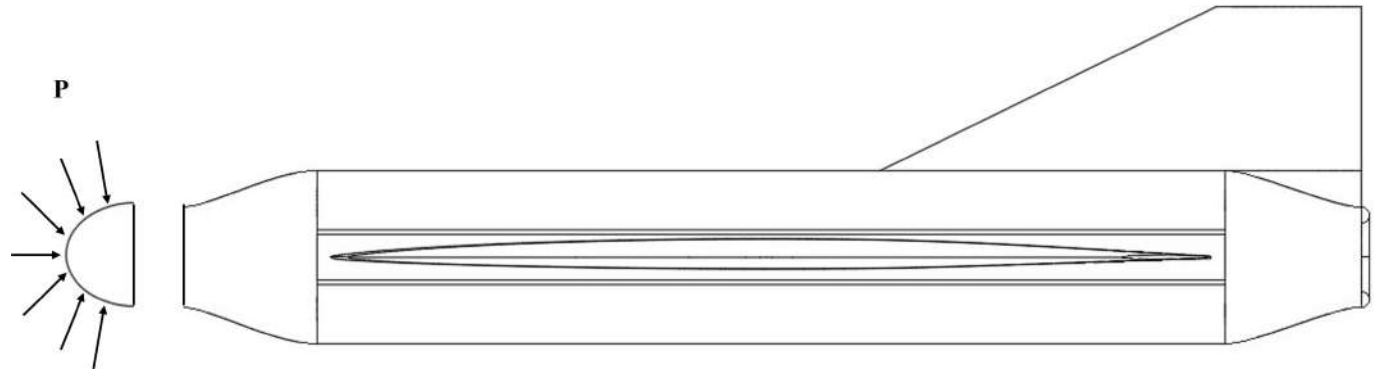
The air-intake correction in the study presents a simple method to account for the propulsion effects of the engine using analytical methods. The geometry of the nosecone is cut into two different sections, as shown in Figure 3.3a. The forces in the nosecone are then subtracted from the total force in the UAV by integrating all forces in the nosecone in the CFD, as shown in Equation 3.36.

$$F = F_x - \left( \int_{nosecone} P_{nosecone} \partial A \right)_x \quad (3.36)$$

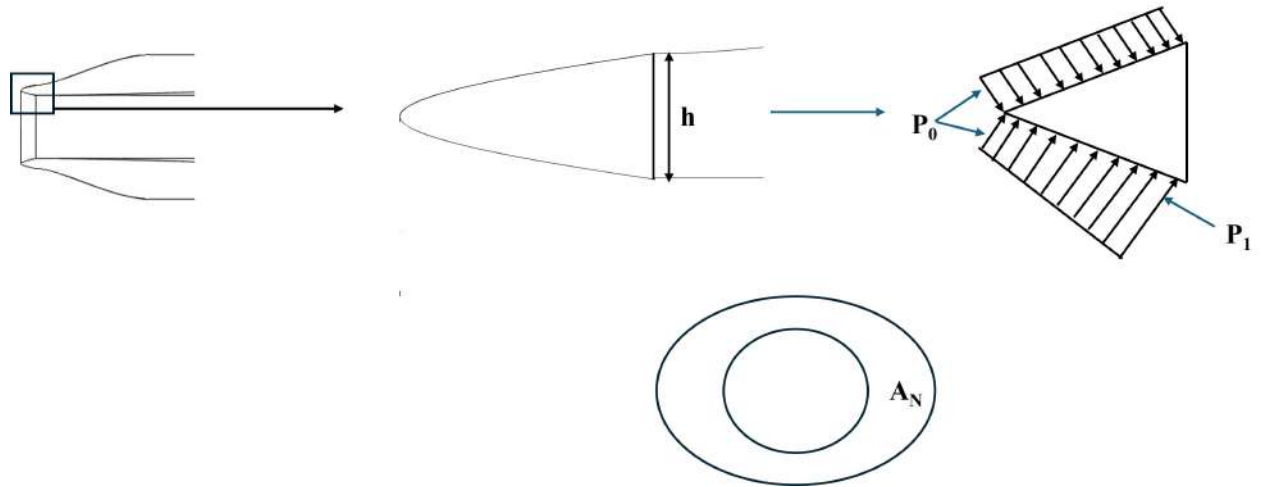
Furthermore, to accurately add the effects of propulsion, the intake geometry of the UAV is used, the lip of the UAV intake is approximated as an isosceles triangle, and the forces on the intake lip are calculated by integrating the pressure over the frontal area of the intake lip. The calculated force is analytically modeled by assuming a linearly varying pressure force from the free-stream to the Fanno-flow back pressure at the UAV intake. The pressure on the external parts of the UAV is assumed to be freestream as a simple approximation, as shown in Figure 3.3b. The effective frontal area of the intake is then calculated for the

direction of drag.

$$F_{lip} = \left( \int_{lip} P_{lip} \partial A \right)_x = (0.75P_0 + 0.25P_1) A_N \quad (3.37)$$



(a) Nosecone force reduction



(b) Intake correction

Figure 3.3: Nosecone Drag correction

where  $P_0$  and  $P_1$  are the freestream pressure and the Fanno flow pressure at the UAV intake.

### 3.3.2 Exhaust

Similar to the approach stated in Section 3.3.1, the solid exhaust face of the nose cone geometry is corrected for the effects of the plume by subtracting the forces from the face, as shown in Figure 3.4.

This provides the force on the body, without the exhaust face of the engine; this term is replaced by forces on the engine afterward in the analytical model.

$$F = F_x - \left( \int_{exhaust} P_{exhaust} \partial A \right)_x \quad (3.38)$$

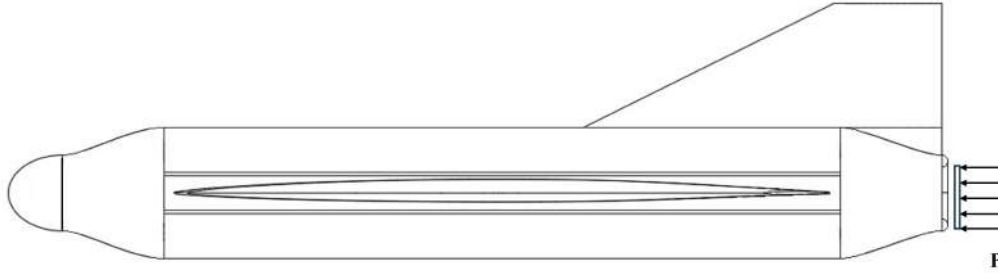


Figure 3.4: Exhaust correction

### 3.3.3 Top speed and stable angle

The calculations of the top speed and the stable angle were performed by fitting the curve between the thrust and drag margins and the lift to the weight margin. The weight of the aircraft is assumed to be 100 kg. For symmetry, 50 kg was assumed. The net forces in either direction were considered a 2<sup>nd</sup> degree polynomial of the Mach number and angle of attack.

$$\begin{aligned} f(M, \alpha) &= \sum a_{i,j} M^i \alpha^j = L - W \\ g(M, \alpha) &= \sum a_{i,j} M^i \alpha^j = F_T - D \end{aligned} \quad (3.39)$$

The top speed and stable angle are calculated by equating the fitted model to 0 and solving the equations simultaneously.

$$\begin{aligned} f(M, \alpha) &= 0 \\ g(M, \alpha) &= 0 \end{aligned} \quad (3.40)$$

### 3.4 Summary

The chapter provides an overview of the analytical methods applied to model the propulsion systems utilized for CFD simulations. The engine is modeled with the standard Brayton cycle. The pressure on the face of the engine is calculated and utilized in the CFD simulation with the engine exit conditions on the face of the exhaust of the UAV. The upstream engine face pressure is calculated by solving for the Mach number and integrating it with the UAV intake with the Fanno flow. The force on the capped nozzle modeled as a solid surface in CFD was corrected by removing integrated pressure, as the force is already accounted for in the thrust equation and is utilized in the net force calculation for the top speed and stable angle of attack. The intake is then corrected by removing the forces acting on the nose cone and adding a simple formulation of the pressure distribution for the intake. The final section of the chapter demonstrates the calculation of the top speed and the stable angle of attack at the top speed to lift the UAV.

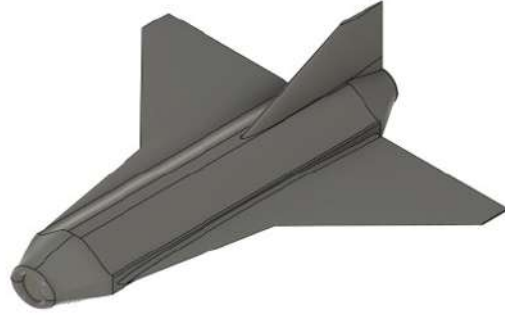
# Chapter 4

## CFD Model

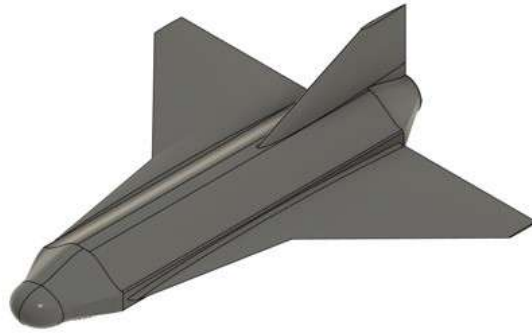
The chapter presents the overall numerical framework for CFD simulations. The description of the geometry, computational domain, mesh, boundary conditions, solver settings, etc. is presented. Furthermore, a method to calculate the discretization error and the results of the discretization errors are presented.

### 4.1 Geometry

The MUFASA B.1 geometry used for the CFD simulations was scaled to fit the AMT Lynx engine. The cruise altitude for MUFASA A was chosen to near 4000 m. An updated version is intended to operate at 11,000 m to achieve higher cruise speeds. Therefore, that altitude is selected for the current study. The scaling factor is 1.81 for the SSUAV, to fit the AMT Lynx engine. Two different geometries were simulated, one with a pitot intake and the other with a nose cone. The nose cone is a simple ellipsoid, due to the complex elliptical frontal of the UAV. Hence, other streamlined nose cones, such as haack series or conical nose, were not chosen. The cylindrical tube equal in diameter to the AMT Lynx engine intake was added to the geometry to incorporate the Fanno flow before the engine input. Only half of the geometry was utilized in the CFD simulations using a symmetry plane to reduce the computational cost. The air intake and the nose cone geometries (full body) are shown in Figure 4.1.



(a) MUFASA B.1 Air-intake geometry



(b) MUFASA B.1 nose cone geometry

Figure 4.1: MUFASA geometries

## 4.2 Mesh Generation

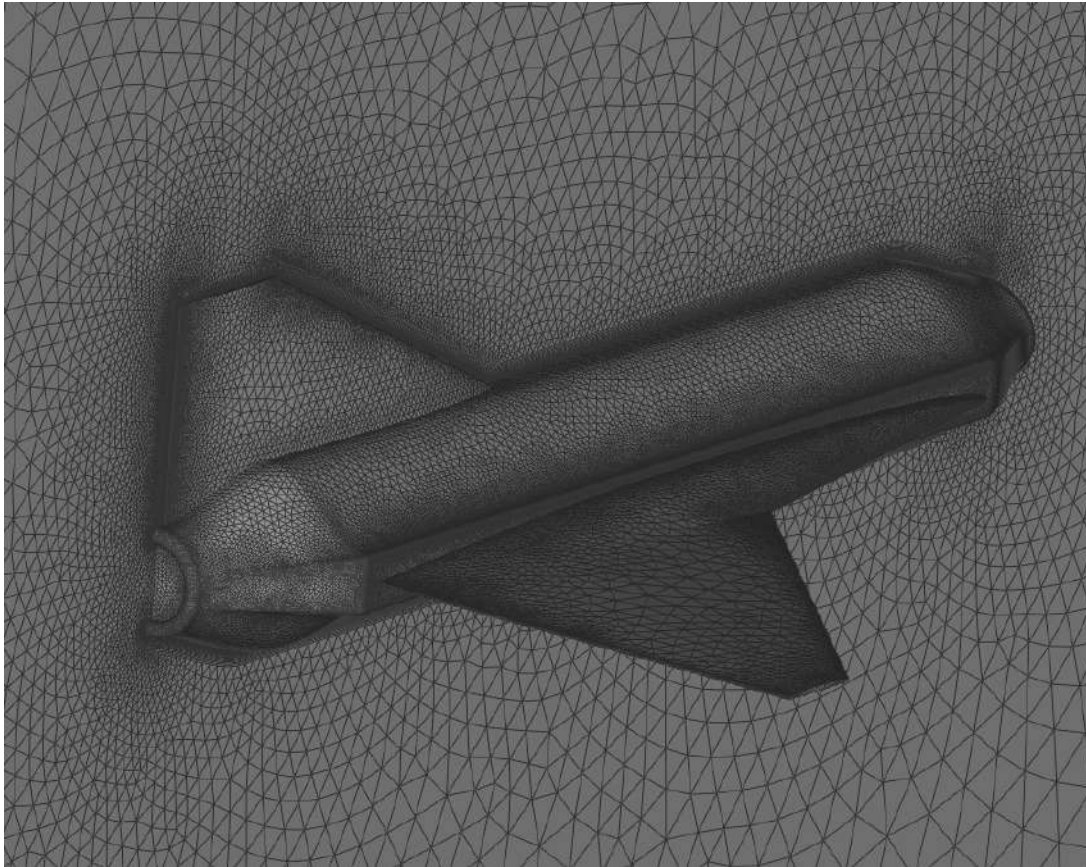
Computational meshes were generated using BETA CAE ANSAv25.0.1. The surface mesh consists of triangular elements, with inflation layers generated to capture the boundary layer using prismatic cells. The volumetric elements consist of tetrahedra. The surface mesh of MUFASA B.1 is shown in Figure 4.2a. Similarly, the surface representation of the inflation layer is presented in Figure 4.2b. The height of the first layer  $\Delta y$  is calculated using  $y^+$ :

$$y_+ = \frac{u_w \Delta y}{\nu} \quad (4.1)$$

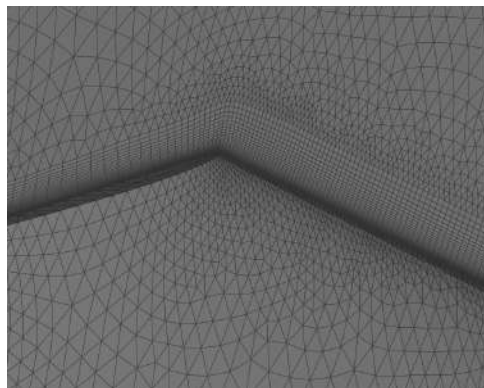
$$u_w = \sqrt{\frac{\tau_w}{\rho}} \quad (4.2)$$

$$\tau_w = \frac{1}{2} C_f \rho V^2 \quad (4.3)$$

where  $u_w$ ,  $\nu$ ,  $\rho$ ,  $C_f$ ,  $\tau_w$ , and  $V$  are local friction velocity, kinematic viscosity, density, local friction coefficient, wall shear stress, and velocity, respectively.



(a) Surface mesh



(b) Inflation layer

Figure 4.2: Fine mesh MUFASA B.1

The growth rate for the inflation layers is kept  $\leq 1.2$ , to reduce the sudden transition between cells.

### 4.3 Domain and Boundary conditions

The domain length is non-dimensionalised six times the length of the SSUAV in the mean flow direction and two times the length in the respective orthogonal axes. The symmetry boundary is considered to reduce the elements to half for faster computations. The domain and SSUAV dimensions are shown in Figure 4.3. The domain used is chosen to attain a good trade-off between computational efficiency and accuracy. Longer domains could be utilized, but, since most of the Mach numbers studied are supersonic, a shorter domain similar to Stoldt (2021) was chosen. The freestream boundary conditions for the turbulence variables are calculated using formulations presented by F. R. Menter (1994).

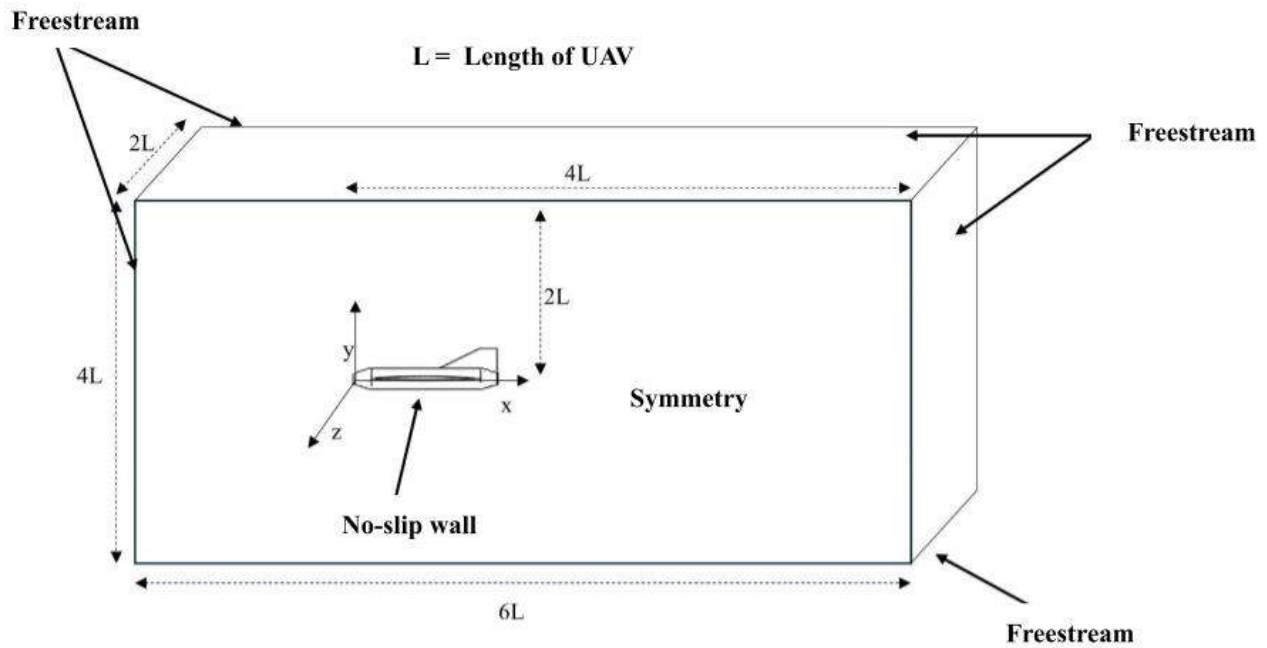


Figure 4.3: Computational Domain

The boundary conditions applied on the faces of both UAV geometries are shown in Figure 4.4. The boundary condition used in every face is shown in Figure 4.3. The solving variables

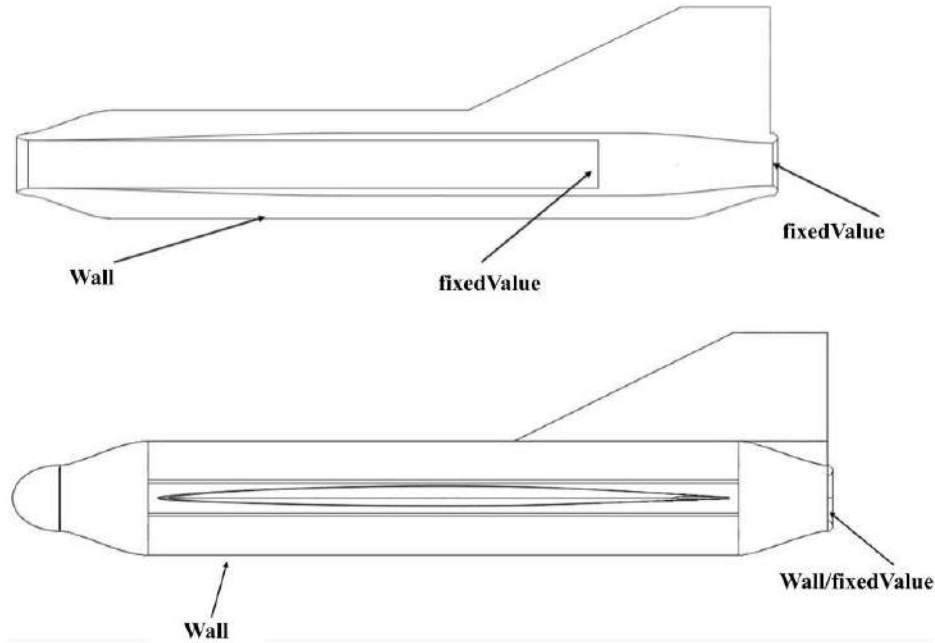


Figure 4.4: Boundary conditions on the UAV

and their values on faces as boundary conditions are shown in Table 4.1. The fixed values for engine intake and engine exhaust are calculated using the analytical propulsion model presented in the previous chapter. The boundary conditions are native to the OpenFOAM solver. Hence, the behavior of boundary conditions is as follows:

1. **fixedValue**: The condition provides a constant value on the entire face of the specific variable.
2. **freestream**: The condition provides a constant value when the flux is going inside the domain and a zeroGradient condition when the flux is moving out.
3. **noSlip** : Zero velocity condition at the face
4. **zeroGradient** : The condition provide a Neumann boundary condition of  $\nabla\psi = 0$
5. **omegaWallfunction** : A calculated wall condition as a function of the first cell height as proposed by F. R. Menter (1994)
6. **alphatWallFunction**: It is a compressible wall function that is used to model thermal conductivity near the wall boundary.

Table 4.1: Boundary conditions, all the quantities are in SI units

	Freestream	Wall	Engine inlet	Engine exhaust	Symmetry
<b>k</b>	fixedValue : $\frac{0.1U_\infty^2}{Re_L}$	fixedValue: 0	zeroGradient	zeroGradient	symmetry
<b><math>\omega</math></b>	fixedValue : $10\frac{U_\infty}{L}$	omegaWallFunction	zeroGradient	zeroGradient	symmetry
<b>Pressure</b>	freestream: 22632.1	zeroGradient	fixedValue	fixedValue	symmetry
<b>Temperature</b>	freestream: 216.65	zeroGradient	zeroGradient	fixedValue	symmetry
<b>Velocity</b>	freestream: 236.04-442.56	noSlip	zeroGradient	fixedValue	symmetry
<b><math>\nu_t</math></b>	freestream: $5 \cdot 10^{-5}$	fixedValue: 0	zeroGradient	zeroGradient	symmetry
<b><math>\alpha_t</math></b>	calculated: 0	compressible::alphiWallFunction	calculated: 0	calculated: 0	symmetry

7. **calculated:** This boundary condition calculates the variables from other variables.

## 4.4 Solvers

This section contains the solver description for the numerical simulations completed in OpenFOAM. A hybrid central solver, pimpleCentralFoam (M. Kraposhin et al., 2015; M. V. Kraposhin et al., 2018), which uses the PIMPLE algorithm, which is a hybrid solver comprising of the PISO (Pressure Implicit with Splitting of Operator) and SIMPLE (Semi-Implicit Method for Pressure-Linked Equations) scheme. PimpleCentralFoam was developed from the widely utilized rhoCentralFoam solver. Earlier, similar solvers have been utilized by various researchers with and without physical-chemistry formulations. The general Navier-Stokes equations for mass, momentum, and energy are solved as presented:

$$\frac{\partial \rho}{\partial t} + \nabla \cdot (\rho \mathbf{V}) = 0 \quad (4.4)$$

$$\frac{\partial \rho \mathbf{V}}{\partial t} + \nabla \cdot [\mathbf{V}(\rho \mathbf{V})] = -\nabla \mathbf{P} + \rho \mathbf{f} + \nabla \cdot \boldsymbol{\tau} + \mathbf{F} \quad (4.5)$$

$$\frac{\partial \rho \mathbf{E}}{\partial t} + \nabla \cdot [\mathbf{V}(\rho \mathbf{E})] = -\nabla \cdot (\mathbf{P} \mathbf{V}) + \rho \mathbf{f} \cdot \mathbf{V} + \nabla \cdot (\boldsymbol{\tau} \cdot \mathbf{V}) + \nabla \cdot \mathbf{q} + \mathbf{Q} \quad (4.6)$$

The PIMPLE algorithm solves a pressure correction loop for the momentum equation 4.5. The algorithm for PIMPLE is shown in Figure 4.5

The SIMPLE algorithm converges faster and accurately captures discontinuities for high-

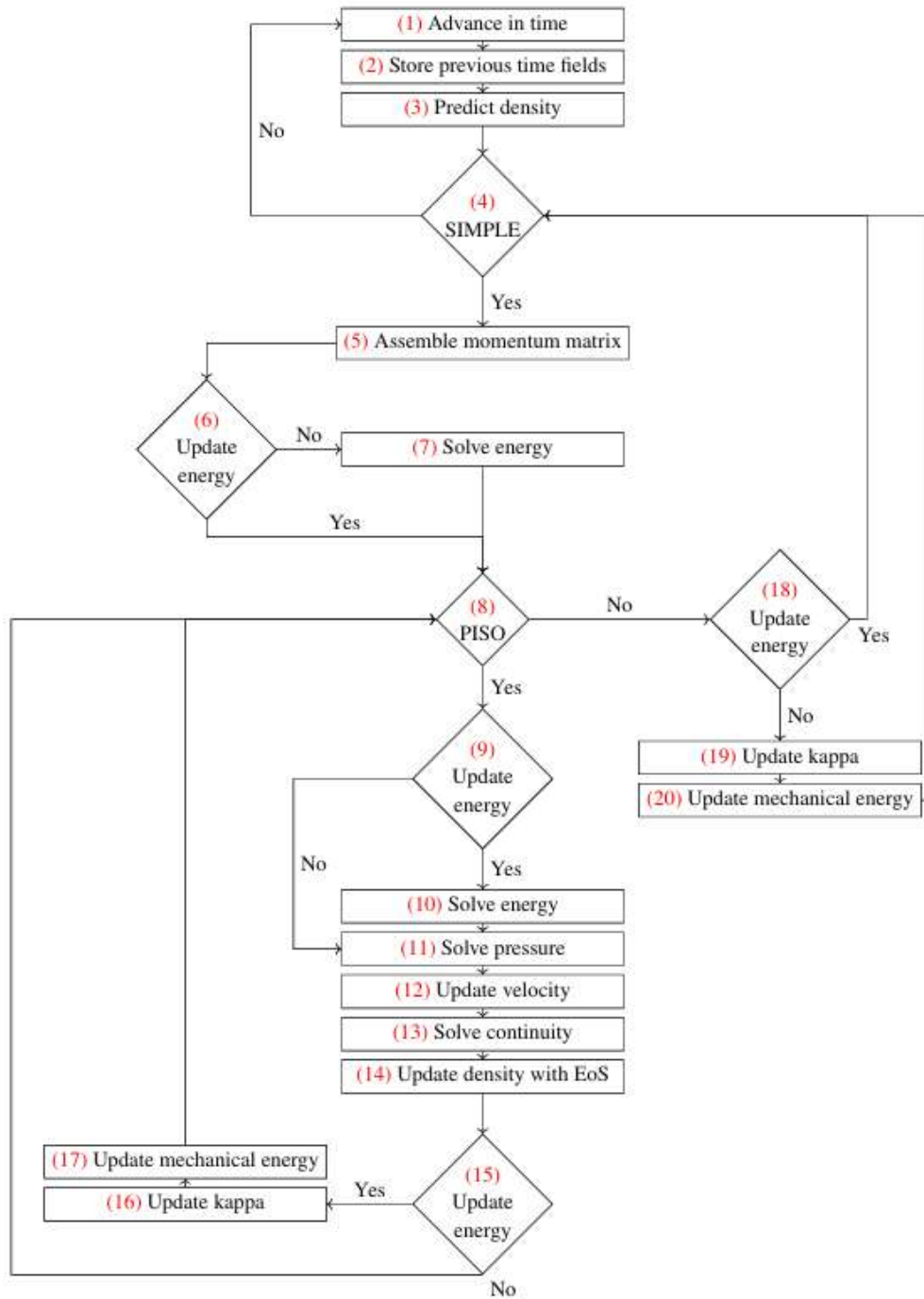


Figure 4.5: PIMPLE algorithm. Adapted from (M. V. Kraposhin et al., 2018)

speed flows but shows poor performance for low Mach numbers, whereas the PISO algorithm is inaccurate in calculating characteristics wave speed, but is good for low-speed transient flows. Hence, this hybrid approach with the outer SIMPLE loop and the inner PISO loop provides a better numerical accuracy for compressible steady-state flow. Another challenge of poor global energy conservation is addressed by M. V. Kraposhin et al. (2018), due to the operator splitting approach. To correct for this, the energy is solved after the pressure correction loop. Since `pimpleCentralFoam` is a hybrid solver, its verification is required for cases similar to the current study. The ability of the solver to accurately solve discontinuities such as shocks and turbulence is well documented in several studies, including physical chemistry and without it. The verification and validation cases of `pimpleCentralFoam` are presented in Table 4.2.

Table 4.2: Verification and validation cases

	Supersonic compressible flow	Bowshock	Separated flow	Turbulent flow	Shock wave BLinteraction
Shock Tube Problem (M. V. Kraposhin et al., 2018)	✓				
Backward facing step (M. V. Kraposhin et al., 2018)	✓				
NASAcold-jet benchmark (Lastiwka et al., 2022)	✓			✓	
Compressible confined jet case (Lastiwka et al., 2022)	✓			✓	
Nozzle with normal shock (M. V. Kraposhin et al., 2018)	✓				
Forward-facing step (M. V. Kraposhin et al., 2018)	✓	✓	✓		✓
Turbulent combustion in an ejector ramjet (Migadel, 2024)	✓			✓	

## 4.5 Discretization

### 4.5.1 Temporal Discretization

The temporal discretisation solves for the first term in Equations (4.4) to (4.6). For steady-state calculations, local time-stepping (LTS) is used with a first-order implicit Euler scheme.

This method provides time-step scaling in different cells according to the Courant-Friedrich-Levy number. The unsteady term is used to accelerate the solution towards a steady state. The formulation for the unsteady term is according to:

$$\frac{\partial\psi}{\partial t} = \frac{\psi_t - \psi_{t-1}}{\Delta t} \quad (4.7)$$

#### 4.5.2 Gradient Discretization

The gradient computation was carried out using the Green Gauss method. OpenFOAM calculates the gradient at the cell centre using:

$$\int_{\Omega} \nabla\psi d\Omega \approx \sum_f (\mathbf{A}\psi)_f \quad (4.8)$$

Furthermore, gradient limiters are another numerical tool that prevents sharp gradients and increases the boundedness of the solution for numerical stability. In this study, unidirectional cell-limited with 0.5 as the limiting coefficient is used.

#### 4.5.3 Convective Discretization

The convective discretization works on the second terms of the Navier-Stokes equation. Generally, convective discretization for compressible flow involve calculation of fluxes through cell faces for a specific conserved quantity  $\beta$ . Kurganov, Noelle and Petrova (KNP) scheme, is generally preferred in OpenFOAM for convective discretization with pimpleCentralFoam. The discretization between two cells with centroid C and N are shown in Figure 4.6.

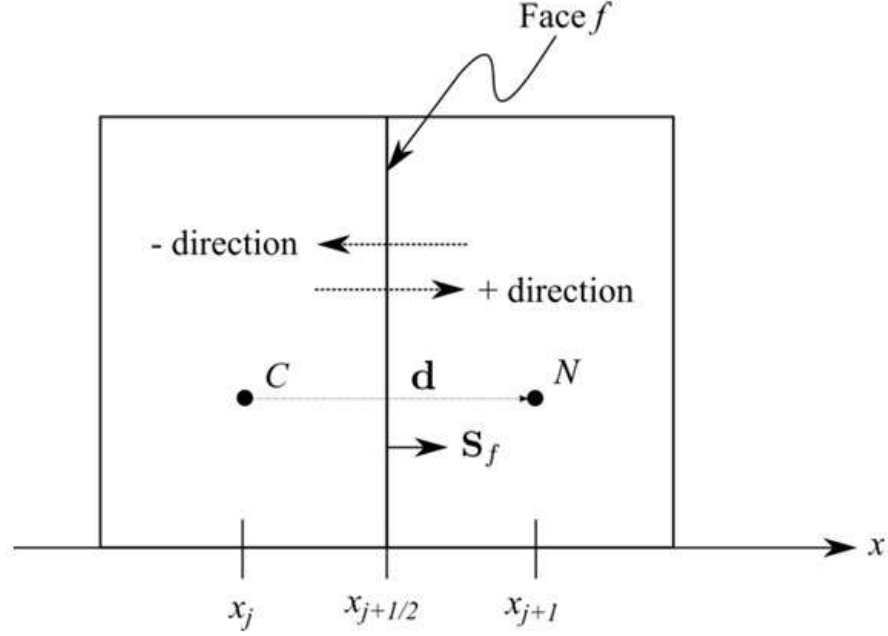


Figure 4.6: Computational cell for finite volume discretization for KNP scheme. Reproduced from (Lastiwka et al., 2022)

The KNP scheme is used in the current study. The scheme uses a central differencing method to calculate the maximum and minimum characteristic wave speeds  $|\vec{U}| + c$  and  $|\vec{U}| - c$ , to split the fluid motion. The contribution of the positive and negative sides of the cell face provides a weighted flux formulation as shown in Equation 4.10.

$$\int_V \nabla \cdot (\vec{U}\psi) dV = \sum_f \psi_f \phi_f \quad (4.9)$$

$$\sum_f \psi_f \phi_f = \sum_f (\alpha \psi_{f+} \phi_{f+} + (1 - \alpha) \psi_{f-} \phi_{f-} + \xi_f (-\psi_{f+} + \psi_{f-})) \quad (4.10)$$

where  $\psi_f$ ,  $\phi_f$ ,  $\alpha$ , and  $\xi_f$  are flow parameter, volumetric flow rate, weighted function, and the diffusion term formulated using Equations (4.11) to (4.14).

$$\alpha = \frac{a_{f+}}{a_{f+} + a_{f-}} \quad (4.11)$$

$$\xi_f = \alpha(1 - \alpha)(a_{f+} + a_{f-}) \quad (4.12)$$

where  $a_{f+}$  and  $a_{f-}$  are the local speeds of propagation (Greenshields et al., 2010).

$$a_{f+} = \max(\phi_{f+} + c_{f+}|\vec{A}_f|, \phi_{f-} + c_{f-}|\vec{A}_f|, 0) \quad (4.13)$$

$$a_{f-} = -\min(\phi_{f+} - c_{f+}|\vec{A}_f|, \phi_{f-} - c_{f-}|\vec{A}_f|, 0) \quad (4.14)$$

where  $c_{f+} = \sqrt{\gamma RT_+}$  and  $c_{f-} = \sqrt{\gamma RT_-}$  are the local speed of sound for the positive and negative sides, respectively. PimpleCentralFoam uses a switching function using  $\kappa_f$ , which utilises Mach number and Courant number (CFL). As  $\kappa_f$  approaches zero, the incompressible formulation is preferred, and as it approaches 1, the formulation changes to compressible using the following equations:

$$\kappa_f = \min\left(\frac{M_f}{CFL}, 1\right) \quad (4.15)$$

The combined contribution of the functions provides the mass flux across the face. Using a hybrid central differencing formulation:

$$\Phi_{f-} = \kappa_f \alpha \rho_{f+} (\phi_{f+} + a_{f-}) \quad (4.16)$$

$$\Phi_{f+} = (1 - \kappa_f) \alpha \rho_{f+} (\phi_{f+} + a_{f-}) + \rho_{f-} ((1 - \alpha) \phi_{f-} - \alpha a_{f-}) \quad (4.17)$$

#### 4.5.4 Interpolation Schemes

The values of the flow variable  $\phi_f$  from the cell centroid must be interpolated onto the faces using an interpolation scheme. The current study uses a vanAlbada total variable diminishing (TVD) scheme. The scheme provides a limiter  $\theta(r)$  that uses a blending function to switch between upwind interpolation for sharp gradients to linear interpolation for weaker gradients and is calculated using:

$$\theta(r) = \frac{r + r^2}{1 + r^2} \quad (4.18)$$

The limiter parameter  $r$  is calculated using :

$$r = 2 \frac{\mathbf{d} \cdot (\nabla \psi)_C}{(\nabla_d \psi)_f} - 1 \quad (4.19)$$

where  $\mathbf{d}$  is the normal vector between the cell centers,  $(\nabla_d \psi)_f$  and  $(\nabla \psi)_C$  are the gradient between cell C and N and the gradient in cell center C as show in Figure 4.6.

#### 4.5.5 Laplacian Discretization

The Laplacian discretization in `pimpleCentralFoam` is applied with a standard finite-volume Laplacian operator, that is, as the diffusivity weighted face gradients  $(\nabla \psi)_f$  are computed and integrated over the faces of the computational cell.

$$\int_{\Omega} \nabla \cdot (\rho J_{\psi} \nabla \psi) d\Omega = \sum_f (\rho J_{\psi} \nabla \psi \cdot \mathbf{A})_f \quad (4.20)$$

In addition, the gradient product with the face area vector is approximated using:

$$\nabla \psi \cdot \mathbf{A} \approx A_{orth} (\psi_{f+} - \psi_{f-}) + \sigma \cdot \nabla \psi \quad (4.21)$$

$$A_{orth} = \frac{|A|^2}{|\mathbf{A} \cdot \mathbf{d}|} \quad (4.22)$$

$$\sigma = \mathbf{A} - A_{orth} \cdot \mathbf{d}$$

The term  $\sigma$  tends to zero for orthogonal meshes.

## 4.6 Turbulence modelling

Turbulence is modeled using the SST  $k-\omega$  model. The model was developed by F. R. Menter et al. (2003). The formulation switches between its standard variant near the wall and the  $k-\epsilon$  variant away from the wall. The equations for  $k$  and  $\omega$  are added to the conservation equations:

$$\frac{D}{Dt}(\rho \omega) = \alpha \rho S^2 - \frac{\partial}{\partial x_i} [(\mu + \sigma_{\omega} \mu_t) \frac{\partial \omega}{\partial x_i}] - \rho \beta \omega^2 - (F_1 - 1) C D_{k\omega} + S_{\omega}, \quad (4.23)$$

$$\frac{D}{Dt}(\rho k) = \widetilde{P}_k + \frac{\partial}{\partial x_i} [(\mu + \sigma_k \mu_t) \frac{\partial k}{\partial x_i}] - \rho \beta^* \omega k + S_k. \quad (4.24)$$

where  $CD_{k\omega}$  is the cross-diffusion term, and  $\widetilde{P}_k$  is the turbulent production term, calculated using:

$$CD_{k\omega} = \max(2\rho\sigma_{\omega 2} \frac{\partial \omega}{\partial x_i} \frac{\partial k}{\partial x_i} \frac{1}{\omega}, 10^{-10}) \quad (4.25)$$

$$\widetilde{P}_k = \min \left( \tau_{ij} \frac{\partial U_i}{\partial x_j}, 10\beta^* k \omega \right) \quad (4.26)$$

The blending function  $\varphi$  is utilised in the model to subsequently add the contribution of each model:

$$\varphi = \varphi_1 F_1 + \varphi_2 (1 - F_1) \quad (4.27)$$

with  $F_1$  being the near-wall term that accounts for the adverse pressure gradients in the  $k - \omega$  model (F. R. Menter, 1994).

$$F_1 = \tanh \left\{ \left\{ \min \left[ \max \left( \frac{\sqrt{k}}{\beta^* \omega y}, \frac{500\nu}{y^2 \omega} \right), \frac{4\sigma_{\omega 2} k}{CD_{k\omega} y^2} \right] \right\}^4 \right\} \quad (4.28)$$

The turbulent viscosity  $\nu_t$ , calculated:

$$\nu_t = a_1 \frac{k}{\max(a_1 \omega, b_1 F_2 S)} \quad (4.29)$$

where,  $F_2$  is the variable formulated using:

$$F_2 = \tanh \left[ \left[ \max \left( \frac{2\sqrt{k}}{\beta^* \omega y}, \frac{500\nu}{y^2 \omega} \right) \right]^2 \right] \quad (4.30)$$

The near wall is resolved with  $y_+$  close to 1, as stated in Section 4.2. In this method the near-wall region is not analytically modeled using the boundary layer theory, instead the boundary layer is solved using the turbulent equations. Additional cofactors of the model are presented in Table 4.3.

Table 4.3:  $k - \omega$  SST coefficients

$\alpha_{k1}$	$\alpha_{k2}$	$\alpha_{\omega1}$	$\alpha_{\omega2}$	$\beta_1$	$\beta_2$	$\gamma_1$	$\gamma_2$	$\beta^*$	$a_1$	$b_1$	$c_1$
0.85	1	0.5	0.856	0.075	0.0828	$\frac{5}{9}$	0.44	0.09	0.31	1	10

## 4.7 Linear solver

The conservation and turbulence equations after discretization are in the form of linear equations. Hence, for systems of linear equations, matrix solvers are used to calculate a solution. The current work uses the preconditioned biconjugate gradient stabilized (PBiCGStab) method. The diagonal incomplete lower-upper (DILU) preconditioner was used to accelerate convergence. The tolerances were  $10^{-10}$  for the final iteration.

## 4.8 Temporal convergence

Since the simulations utilize a local-time-stepping approach, the solution needs to be stopped at certain iteration when the flow variable does not change significantly between iterations. Hence, the convergence conditions for variables were kept:

$$\frac{\bar{\psi}_i - \bar{\psi}_{i-j}}{\bar{\psi}_i} \leq 0.005 \quad (4.31)$$

The variable  $i$  is the iteration number, and similarly,  $j$  is set to 10000 iterations.

## 4.9 Errors

### 4.9.1 Grid uncertainty

The grid uncertainty was calculated for the air-intake geometry configuration. The grid uncertainty was evaluated using Richardson extrapolation suggested by Roache (1994). The representative grid size was calculated using the equation:

$$h = \left[ \frac{1}{N} \sum_i (\nabla V_i) \right]^{\frac{1}{3}} \quad (4.32)$$

Where  $N$  and  $\nabla V_i$  are the total volumetric cells and the cell volume of cell  $i$ . Refinement between the three meshes was done using a constant refinement ratio  $r$  that equals:

$$r_{ab} = \frac{h_a}{h_b} \quad (4.33)$$

The order of accuracy is calculated using the solution parameters obtained using the three grids and the refinement ratio between the grids.

$$p = \frac{\ln\left(\frac{\psi_3 - \psi_2}{\psi_2 - \psi_1}\right)}{\ln(r)} \quad (4.34)$$

where  $p$  is the observed order of accuracy.

The grid convergence index is then calculated using the formula:

$$GCI_{ab} = \frac{F_s \epsilon}{r^p - 1} \quad (4.35)$$

$$\epsilon = \psi_a - \psi_b \quad (4.36)$$

To calculate values of GCI in percentages, the error can be divided by the finer refinement's solution parameter:

$$\epsilon = \frac{\psi_a - \psi_b}{\psi_b} \quad (4.37)$$

Roache (1994) advised to limit the observed order of accuracy to the theoretical order of accuracy, which is 2 in the current case, when the observed order of accuracy is near ten percent of the theoretical order. The factor of safety chosen for this study is  $F_s = 1.25$ . The extrapolated solution can be calculated using the above parameters using the equation:

$$\psi_{h=0} = \frac{r_{23}^p \psi_2 - \psi_3}{r_{23}^p - 1} \quad (4.38)$$

Three different refinement levels were chosen for the current study, labeled 1, 2 and 3 for the coarse, medium, and fine mesh, respectively. The inflation layer of prismatic cells is refined using a constant refinement ratio of 1.25 as presented in Table 4.4. The Grid convergence

Table 4.4: Refinement levels

Refinement	First cell height	$y_+$	Total number of volumetric elements
1	$13.75 \times 10^{-6}$ m	1.25	$4.1 \times 10^6$
2	$11 \times 10^{-6}$ m	1	$8.06 \times 10^6$
3	$8.8 \times 10^{-6}$ m	0.8	$15.8 \times 10^6$

Table 4.5: Grid convergence index

Solution parameter	Coarse	Medium	Fine	Extrapolated solution	$GCI_{12}$	$GCI_{23}$
$C_L$	0.0276	0.0287	0.0289	0.0292	$2.44 \times 10^{-3}$	$4.44 \times 10^{-4}$
$C_D$	0.0349	0.0329	0.0317	0.0295	$4.44 \times 10^{-3}$	$2.66 \times 10^{-3}$

index is calculated using the procedure mentioned. The  $GCI_{12}$  and  $GCI_{23}$  for the lift and drag coefficients are presented in Table 4.5.

The grid convergence indices for drag and lift coefficients are within 14% for medium and fine grid level refinements. For lift, both the uncertainties are less than 8.5%. For the current study, the reason for the high uncertainty of drag is the deviation of the observed order of accuracy and the limitation of the p to the theoretical order of accuracy. Since the mesh is unstructured, refinements might not be perfectly structured, hence a deviation in order of accuracy can be expected, producing higher uncertainty for smaller refinement ratios such as 1.25. This uncertainty provides enough error bounds to compare analytically applied drag corrections with CFD. The medium mesh is considered for the current study due to the trade-off between uncertainty for the current study and computational efficiency.

## 4.10 Summary

The chapter presents the numerical model utilized using OpenFOAM. The geometry and flow domain were meshed and imported into the OpenFOAM framework. Further numerical discretization was performed using the pimpleCentralFoam solver. The boundary conditions were applied on the faces of the geometry and domain. The  $k - \omega$  SST model was utilized for the study. The discretization error was calculated using Richardson extrapolation. The uncertainty due to discretization was presented and Medium mesh was selected for further

study.

# Chapter 5

## Results

The chapter provides the simulation and analytically corrected propulsion effects for SSUAV MUFASA B.1. Two distinct properties of an air-breathing propulsion system are modeled: 1) the geometry of the forebody as nosecone or intake and 2) the capped/uncapped face of the nozzle of the engine. The parameters resulted in 4 different SSUAV variations 1) air-intake and capped nozzle 2) air-intake and uncapped nozzle 3) nosecone as forebody geometry and capped nozzle 4) nosecone as forebody geometry and uncapped nozzle with plume. Of the four configurations, three are simulated using viscous CFD simulations, and the respective names of the three configurations are presented in Table 5.1. Furthermore, two corrections are applied to the third configuration.

Two corrections were applied to the nosecone geometry, at the exhaust face and on the nosecone forebody, to analyze the effect on drag due to the propulsion system, which are shown in the last two rows of Table 5.1. Aerodynamic coefficients for lift and drag force were analyzed for three different angle of attack, 0, 0.5 and 1 degree, respectively. The angles were chosen to study the effect of trim angles on the performance.

Table 5.1: MUFASA B.1, configurations simulated using high-fidelity CFD and corrected using low-fidelity analytical method

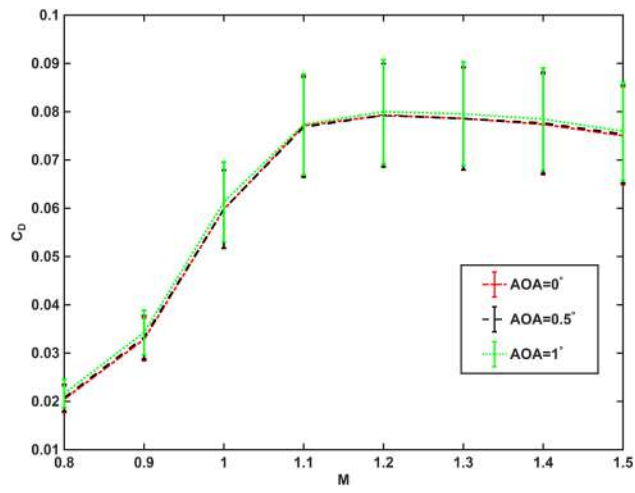
Analysis	symbol
Air-Intake and uncapped nozzle- CFD	$B_1$
Nose cone and uncapped nozzle - CFD	$B_2$
Nose cone and capped nozzle - CFD	$B_3$
$B_3$ exhaust corrected	$B_4$
$B_4$ intake corrected	$B_5$

## 5.1 Effect of angle of attack on integral aerodynamic quantities

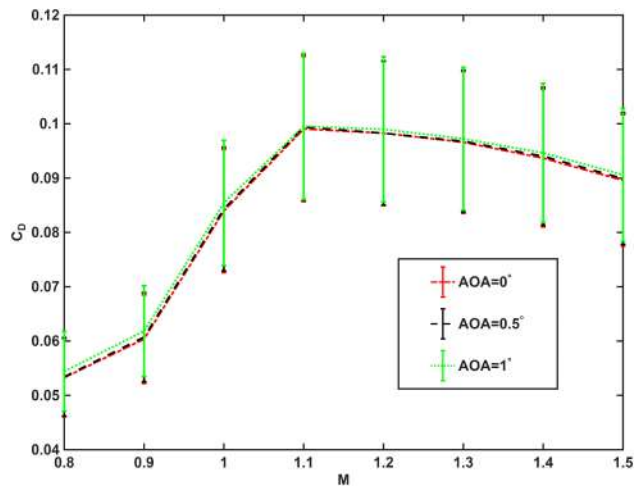
The section presents aerodynamic analysis of the simulated geometry using CFD in the three angles of attack. The lift and drag forces are analyzed, and the forces are converted to aerodynamic coefficients as stated in the Appendix A.

### 5.1.1 Drag

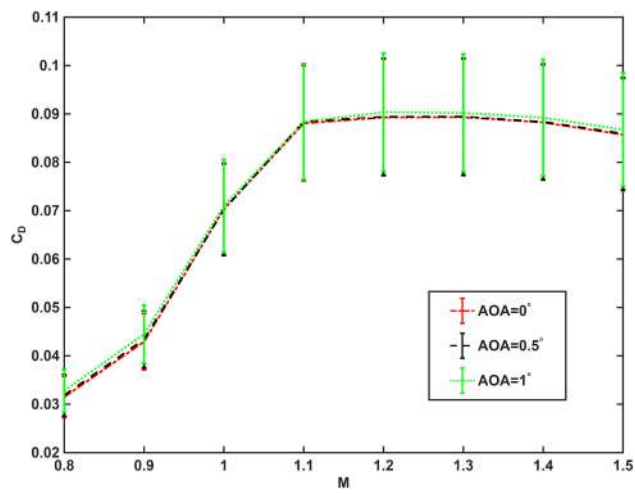
The drag coefficient across eight Mach numbers and three angles of attack are presented for the first three cases  $B_1$ ,  $B_2$ , and  $B_3$  as shown in Figure 5.1. As stated in Section 2.2.1, an induced drag component is responsible for the increase in drag, as the angle of attack increases. Since the angle of attack for the current study is relatively small, this induced drag component is insignificant. Hence, the drag values across all angles of attack are nearly the same, with  $< 5\%$  error. The drag values peak near Mach 1.1 for  $B_2$  and at Mach 1.2 for the  $B_1$  and  $B_3$  configurations. The drag values show a steady decline ( $\approx 2\%$  in each consecutive pair of Mach numbers for the  $B_2$  configuration and  $1\%$  in each pair of consecutive Mach numbers for  $B_1$  and  $B_3$ ) after Mach 1.1 for  $B_2$  and post Mach 1.2 for  $B_1$  and  $B_3$ . At higher Mach numbers, the difference in drag values between the configurations can become significantly more prominent. Although the decline in drag values after the peak drag is similar for  $B_1$  and  $B_3$ , since the absolute values are significantly different and the formulation differs in calculating integral quantities, further investigation is needed.



(a)



(b)



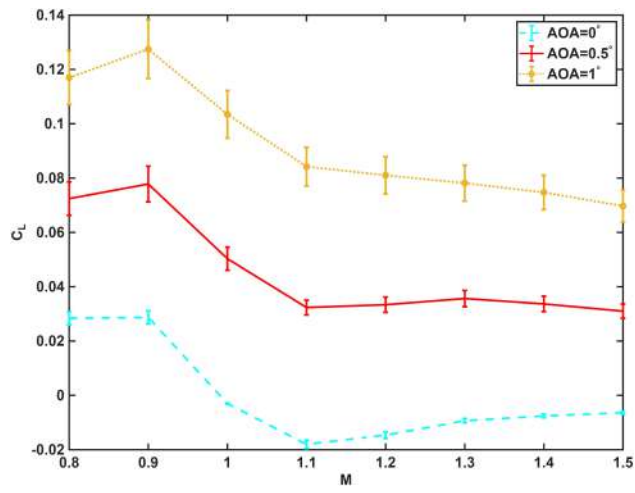
(c)

Figure 5.1: Drag coefficient values across Mach numbers (a)  $B_1$  (b)  $B_2$  (c)  $B_3$

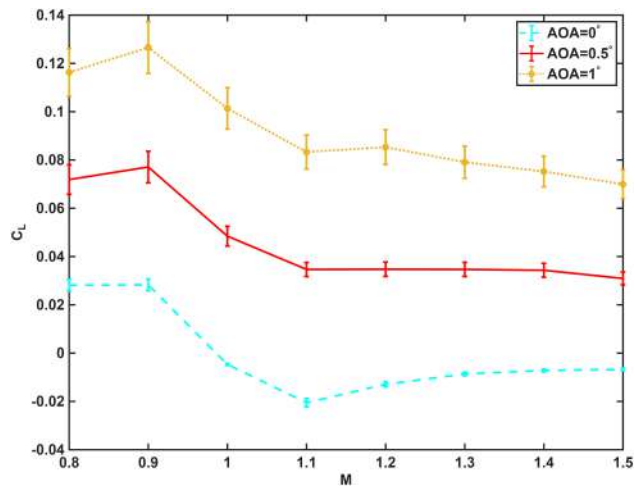
### 5.1.2 Lift

Similar to the drag coefficients, the lift coefficients between the Mach numbers and the angle of attacks are plotted in Figure 5.2. The slope of the lift force vs. angle of attack, for thin airfoils and wings, using the inviscid theory, is equal to  $2\pi$  for incompressible flow (Anderson, 2011). This presents a linear relationship of lift with angle of attack. In compressible flow, this behavior is not always observed. However, as the angle of attack increases, an increase in lift still shows a linear behavior in most of the wings and airfoils. Similar behavior can be observed in all three configurations; the lift coefficient varies linearly with the angle of attack for a particular Mach number.

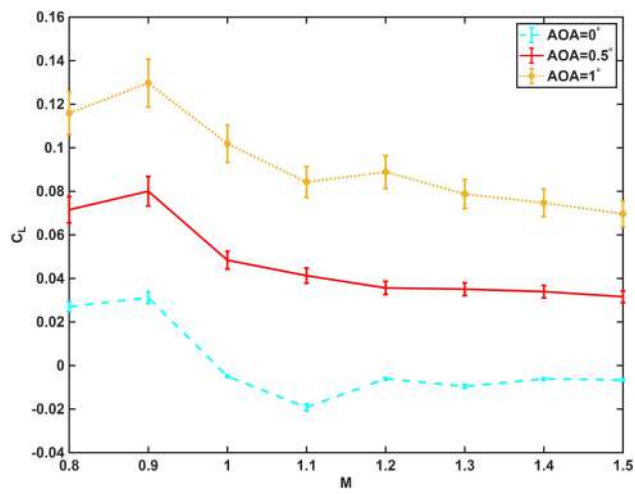
The peak lift values are observed at Mach 0.9 for all configurations. Another important phenomenon is observed at supersonic speeds, post Mach 1, a drop in lift is observed for all the configurations, and all angles of attack. This occurs because of a phenomenon called "shock stall," in which a strong bow shock forms near the trailing edge of the wing, leading to flow separation and a significant drop in lift. As a result, the pressure behind the wing decreases, reducing overall lift. This loss of lift is maximum for zero angle of attack, across simulated configurations, when the aircraft exceeds Mach 0.9. The reduction in lift is observed to be close to 60-70% for zero angle of attack, and shows the least reduction for  $B_2$  and  $B_3$  at  $AOA = 1$  ( $\approx 35\%$ ). Whereas  $AOA = 1$  for  $B_1$  and  $AOA = 0.5$  for  $B_3$ , shows a steady decline. The lift coefficients show almost a similar trend with respect to angle of attack for all configurations, indicating that the overall aerodynamic behavior remains similar irrespective of additional geometrical features. However, the absolute lift values differ at specific Mach numbers, particularly at  $M = 0.9$  and  $M = 1.2$ . This suggests that plume interactions can influence the lift differently in these regimes without significantly altering the lift curve. In contrast, the drag coefficients display a different behavior. Across all Mach numbers considered, the drag values differ between configurations, but remain relatively similar across angles of attack. This implies that certain Mach numbers ( $M = 1.2$  and  $M = 0.9$ ) need further investigation to analyze the effect of nosecone and plume on the external aerodynamics of the SSUAV.



(a)



(b)



(c)

Figure 5.2: Lift coefficient values across Mach numbers (a)  $B_1$  (b)  $B_2$  (c)  $B_3$

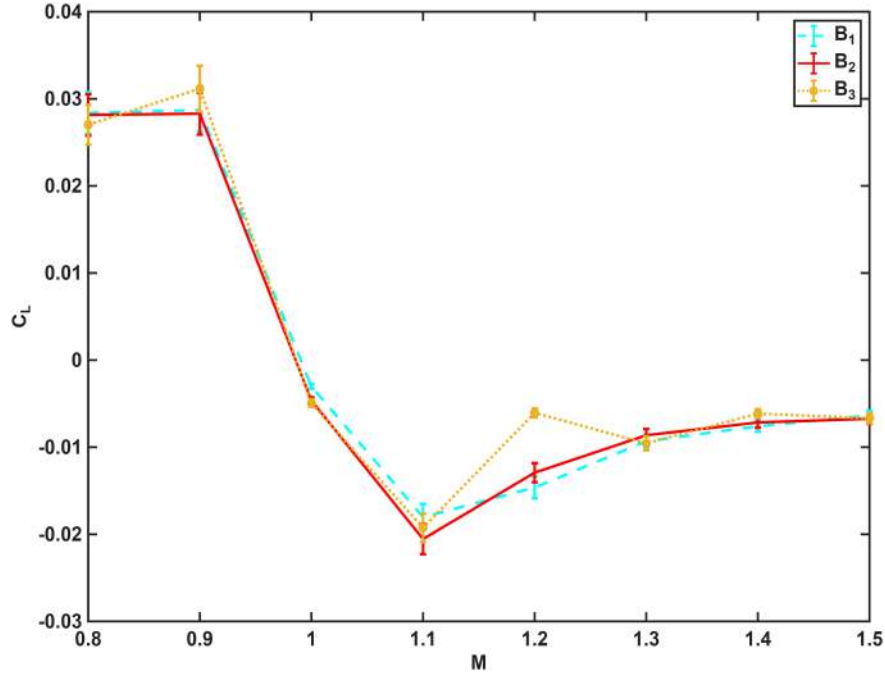


Figure 5.3: Comparison of lift between configurations

## 5.2 Effects of Configuration on Integral Quantities

For comparison between configurations, only the zero angle of attack cases will be compared to analyze the effect of modeling.

### 5.2.1 Lift

Section 5.1.2 showed a linear relationship between the angle of attack and the lift. This section describes the effect on lift associated with simulating the SSUAV across simulated configurations for a zero angle of attack. Figure 5.3 shows the lift coefficient values for the  $B_1$ ,  $B_2$ , and  $B_3$  configurations. The lift values for  $B_3$ , for Mach 0.9 and 1.2, show a deviation of 8% and 53% compared to  $B_1$  and  $B_2$ . The lift force shows an insignificant deviation between  $B_1$  and  $B_2$ ; therefore, the geometry of the forebody does not significantly affect the lift force.

The only distinction between the  $B_2$  and  $B_3$  configurations is the plume; hence, the analysis of the lift force for different components of the SSUAV must be conducted. The forces on the various components of the UAV are also represented in Table 5.2. For Mach

Table 5.2: Lift force on different SSUAV components for  $B_2$  and  $B_3$  configuration

	$B_2$			$B_3$		
	Body	Boattail	Wing	Body	Boattail	Wing
$M = 0.8$	-25 $N$	60.5 $N$	147 $N$	-26.5 $N$	58 $N$	144 $N$
$M = 1.2$	-151 $N$	24.7 $N$	-62 $N$	-97.4 $N$	8.49 $N$	0.4 $N$
$M = 1.5$	-193 $N$	58.9 $N$	-20 $N$	-188 $N$	68.1 $N$	-31.9 $N$

number 0.8 the forces are similar between configurations for each component of the SSUAV. For Mach 1.2 and 1.5, the forces on the boattail and wing have shown a significant deviation between the configurations  $B_2$  and  $B_3$ . Hence, further investigation of the components is required to assess the effect of the plume.

### Boattail

The boattail has shown a deviation of up to 16  $N$  and 10  $N$  for  $M = 1.2$  and  $M = 1.5$  between the configurations presented in Table 5.2. The lift force on the boattail increased from configuration  $B_2$  to  $B_3$  for  $M = 1.5$ . For  $M = 1.2$ , the lift force decreased on the boattail across  $B_2$  and  $B_3$ . Hence, the pressure on the top and bottom surfaces of the boattail needs to be analyzed to understand the deviation caused by the plume. Since the vertical tail spans to the end of the boattail, a plane is utilized at 0.02  $m$  away from the symmetry plane to study the pressure and velocity field. Figure 5.4-5.6 represents the pressure plot on the top and bottom surfaces of the boattail and streamlines for Mach 0.8, 1.2, and 1.5. The pressure is plotted against a non-dimensionalized length  $s$ , using the length of the boattail, with the top and bottom surfaces represented by  $s_+$  and  $s_-$ . The pressure on the upper and lower surfaces is higher for the  $B_2$  configuration for supersonic Mach numbers. But the behaviors for both the Mach numbers differ significantly.

The pressure plot for Mach 0.8 shows a higher pressure value for the top and bottom surface near the front end of the boattail for the  $B_2$  configuration. A higher deviation in pressure is observed for the top surface near the front end between the configurations. For the top surface, larger pressure difference is observed at the rear end of the boattail for Mach 1.5. However, the pressure values at the rear end of the boattail for Mach 1.2 are similar.

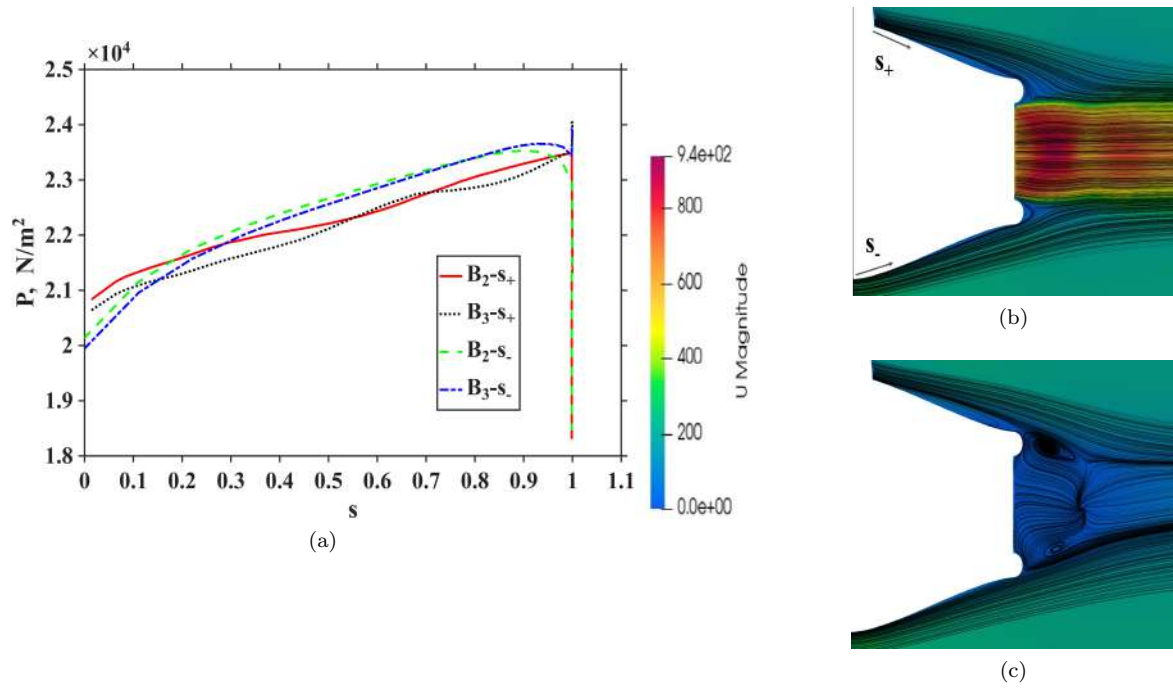


Figure 5.4:  $M = 0.8$ (a) Pressure plot over boat tail (b) Streamlines for  $B_2$  (c) Streamlines for  $B_3$

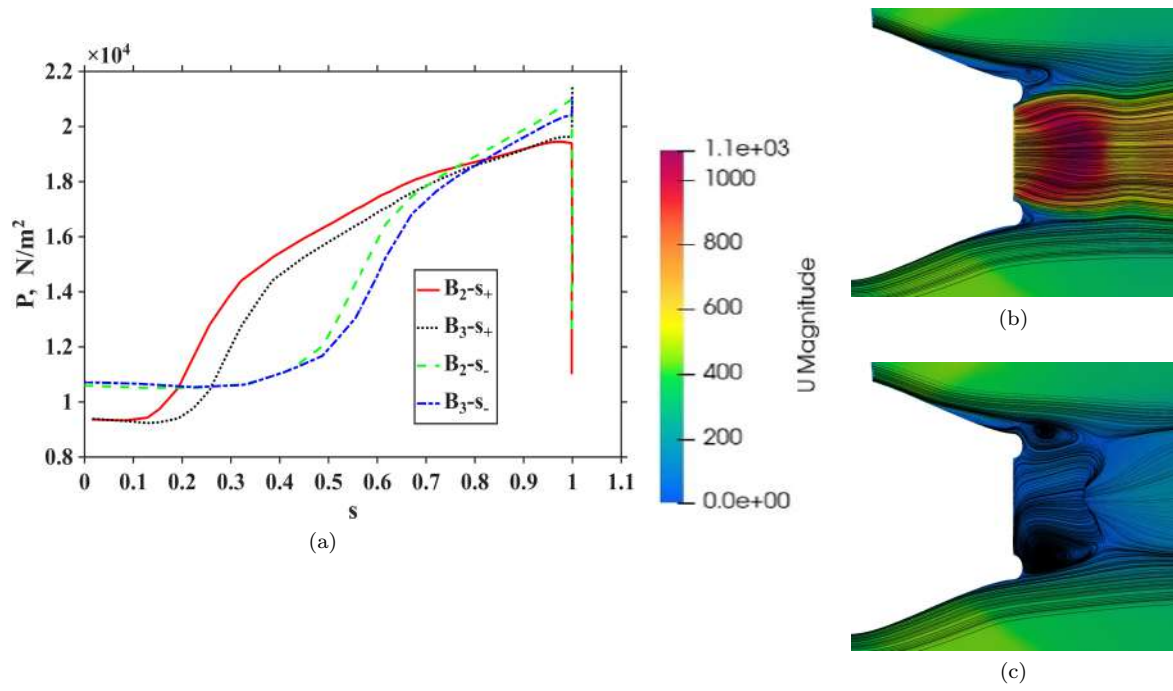


Figure 5.5:  $M = 1.2$ (a) Pressure plot over boat tail (b) Streamlines for  $B_2$  (c) Streamlines for  $B_3$

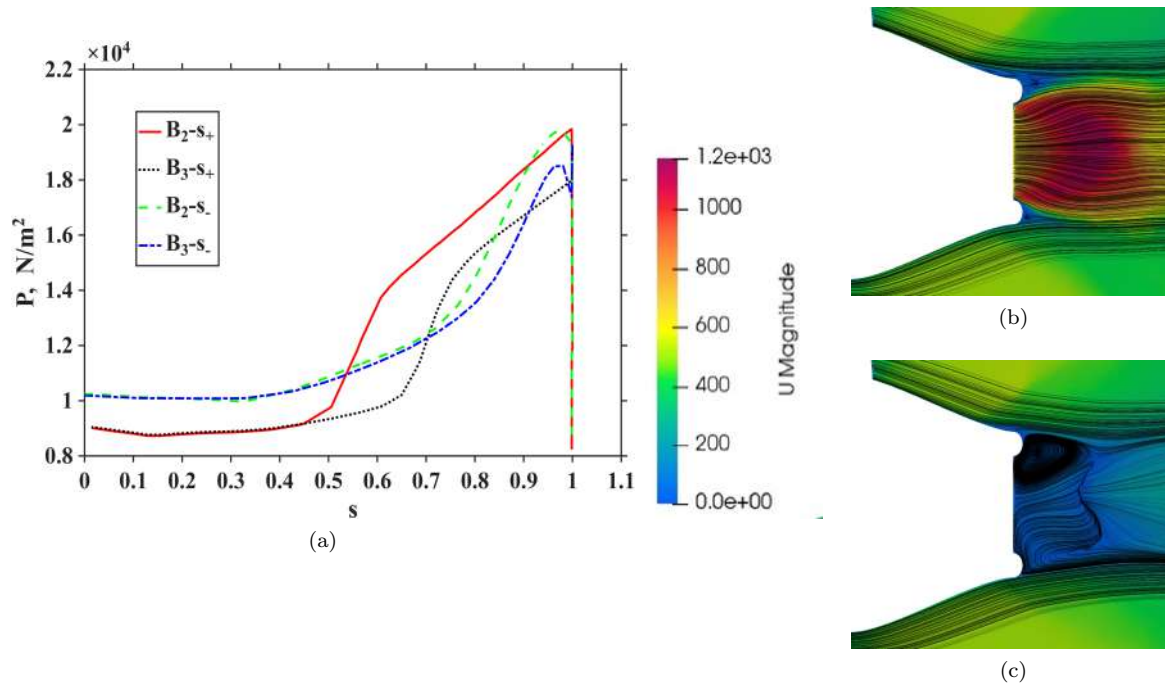


Figure 5.6:  $M = 1.5$ (a) Pressure plot over boat tail (b) Streamlines for  $B_2$  (c) Streamlines for  $B_3$

The bottom surface, on the other hand, shows similar behavior for the pressure, with the difference in pressure beginning to occur around  $s = 0.5$ . Subsequently, the deviation in pressure is larger for Mach 1.5, and peaks near the rear end of the boattail. However, the difference in pressure for Mach 1.2 peaks near  $s = 0.65$ . This implies that the plume shows a direct effect on the pressure at the rear end of the boattail for Mach 1.5, whereas for Mach 1.2, the deviation in pressure can be caused by the changed velocity field.

The streamlines plotted in Figures 5.4-5.6 show that the underexpanded plume does affect the flow around it. Recirculation zones that are observed in Figures 5.4c, 5.5c and 5.6c, near the rear end of the boattail, are absent; because of the higher pressure of the plume, the flow seems to be "pushed back". This can also be observed in the pressure plots, as the increase in pressure on the bottom and top occurs earlier for the  $B_2$  configuration. Although the recirculation zone has shrunk, a drop in pressure is seen at the very rear end of the hull for the  $B_2$  configuration. This region of low pressure could be caused by the plume, as the slower-moving air near the boundary suddenly encounters a sonic plume. As seen for Mach 1.2, the deviation in pressure can occur away from the plume as well; other components that show a higher deviation in lift force should also be investigated to understand the effect of

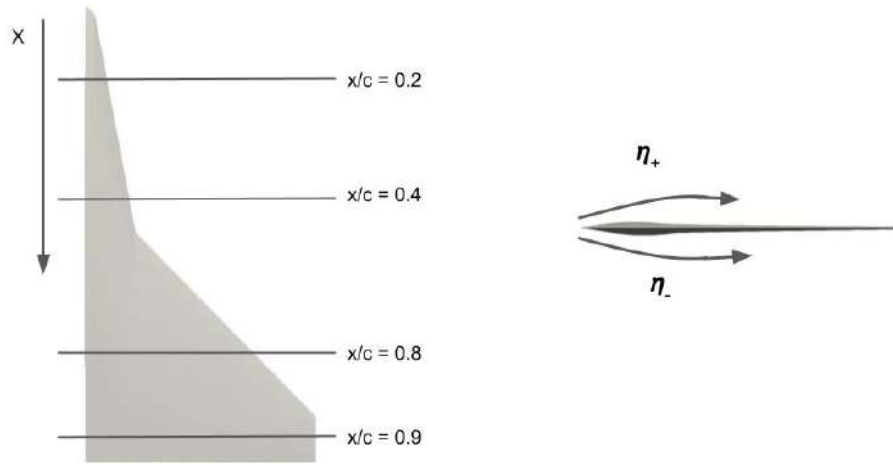


Figure 5.7: Wing cross section along the root chord for pressure plots

the plume away from the boattail.

### Wing

The wing shows a nearly 60  $N$  difference in pressure between the configurations. The observed behavior of pressure on the boattail shows that the plume can affect the pressure at regions away from it. Hence, four cross section along the root chord is chosen to analyze the pressure across the wing span, as shown in Figure 5.7. Non-dimensional distances of  $x/c = 0.2, 0.4, 0.8$  and  $0.9$  were chosen to analyze the pressure across the wingspan. Figures 5.8 to 5.11, show pressure across the wing span for Mach 0.8, 1.2 and 1.5. The wing span varies for different values  $x/c$ , as shown in Figure 5.7. Hence, the wing span is non-dimensionalised, with the span at each  $x/c$  location. Similarly to Section 5.2.1, the top and bottom surfaces of the wing are plotted with  $\eta_+$  and  $\eta_-$ ,  $\eta$  being the non-dimensional span of the wing.

For  $M = 0.8$ , the pressure values show an insignificant deviation between the configurations across all  $x/c$  values, except 0.4. At  $x/c = 0.4$ , the  $B_3$  configurations show lower pressure values for both top and bottom surfaces. The bottom surface shows a higher pressure difference, compared to the top surface for  $M = 0.8$  at  $x/c = 0.4$ .

The effect of plume is insignificant near the tip of the wing for both Mach numbers across

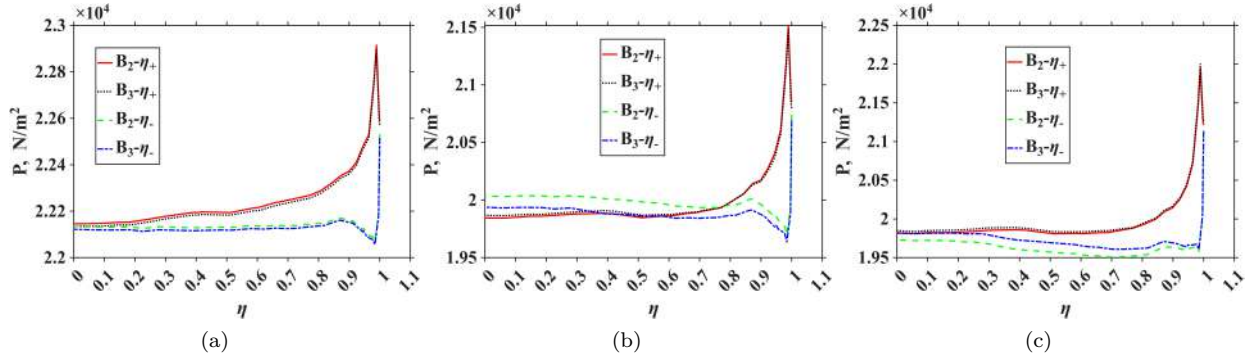


Figure 5.8: Pressure plot over span  $x/c = 0.2$ (a)  $M = 0.8$  (b)  $M = 1.2$  (c)  $M = 1.5$

configurations, signifying negligible effect of the plume near the tip. For supersonic Mach numbers,  $M = 1.2$  and  $M = 1.5$ , the  $x/c$  locations near the front end of the wing show a significant variation in pressure between configurations. For  $M = 1.2$  at  $x/c = 0.2$ , the configuration  $B_2$  has a higher pressure throughout the span of the bottom surface compared to  $B_3$ . However, for  $M = 1.5$ , the behavior is opposite to  $M = 1.2$ , a lower pressure is observed for the configuration  $B_2$  on the bottom surface. The top surface of the wing for both supersonic Mach numbers does not show a significant deviation in pressure between the configurations for  $x/c = 0.2$ . For  $x/c = 0.4$ , a significant deviation can be seen in pressure on both surfaces. The deviation in pressure between the configurations gets bigger near the root chord of the wing. The disturbances on the body of the SSUAV due to the plume, as observed in the previous section, can, in turn, affect the flow around the wing near the root of the wing. The pressure for  $B_2$  shows a higher value than the configurations  $B_3$  for the upper and lower surface of the wing for  $M = 1.5$ . This behavior is opposite to  $M = 1.2$  in  $x/c = 0.4$ .

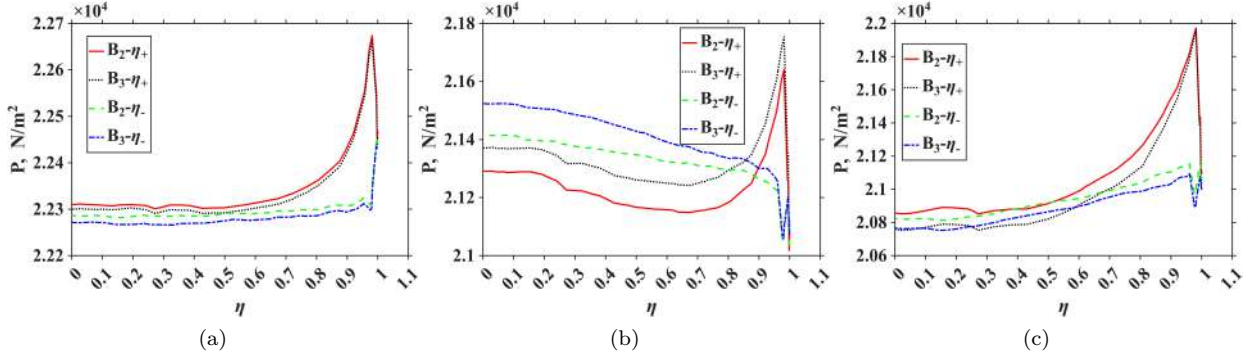


Figure 5.9: Pressure plot over span  $x/c = 0.4$ (a)  $M = 0.8$  (b)  $M = 1.2$  (c)  $M = 1.5$

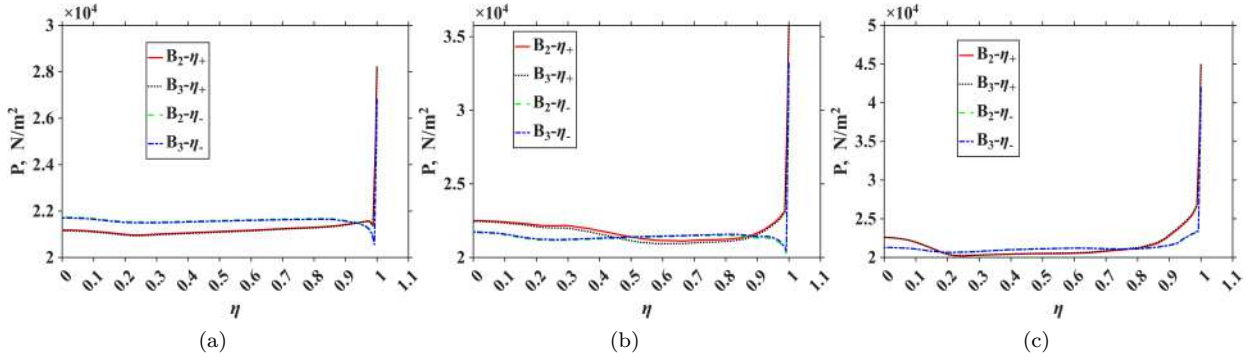


Figure 5.10: Pressure plot over span  $x/c = 0.8$ (a)  $M = 0.8$  (b)  $M = 1.2$  (c)  $M = 1.5$

In Figure 5.10, for  $M = 1.2$  at  $x/c = 0.8$ , the pressure shows an insignificant deviation between the configurations. The  $B_3$  configuration shows lower pressure values on the top surface in a region between  $\eta = 0.3$  and  $\eta = 0.8$ . At higher  $x/c$  locations, the wing span is also longer; therefore, the deviation in pressure is actually integrated over a longer region. This, in turn, can contribute significantly to the deviation in lift force. Subsequently, for  $M = 1.2$  at  $x/c = 0.9$ , the pressure values for the  $B_2$  configuration show higher values compared to  $B_3$  on the bottom surface further away from the SSUAV ( $\eta = 0.5$  to  $\eta = 0.9$ ) and this difference becomes negligible near the root of the wing. However, for  $M = 1.5$ , the pressure is nearly the same for both configurations, between configurations.

Most of the  $x/c$  locations for the supersonic Mach numbers show some deviation in pressure on the wing's surface. However, for  $M = 0.8$ , the deviations are small in all  $x/c$  locations except for 0.4. The pressure behavior for  $M = 1.2$  and  $M = 1.5$  is opposite for  $x/c = 0.2$  and  $x/c = 0.4$ . This signifies that the effect of the plume is inconsistent between the Mach

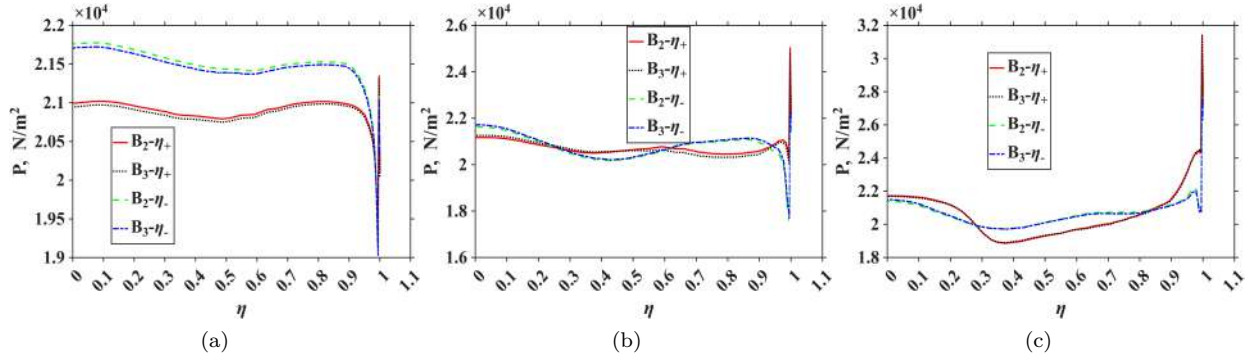


Figure 5.11: Pressure plot over span  $x/c = 0.9$ (a)  $M = 0.8$  (b)  $M = 1.2$  (c)  $M = 1.5$

numbers. Further investigation using better methods can be conducted to quantify this effect; no clear relationship was found. This also means that although the total lift force is similar for the  $B_2$  and  $B_3$  configurations for  $M = 1.5$ , the flow is significantly different.

### 5.2.2 Drag

The integrated force in the direction of flow is the drag experienced by the SSUAV. The contribution of the drag force is due to the propulsion system and the external body. The drag for the three configurations for zero angle of attack are plotted in Figure 5.12. Since two distinct geometries are used, and the propulsion is modeled with simulation and analytically as well, the drag forces are calculated by only integrating forces on the wall. Hence, the drag due to the propulsion system is already calculated in the thrust equation. The nosecone and solid face modeled in the  $B_3$  configurations add additional drag components that in real flight do not exist. The pressure contours of the  $B_1$  and  $B_3$  configurations are shown in Figure 5.13. The  $B_1$  configuration, which does not include the pressure term in the calculation, shows the least drag between Mach numbers. Similarly, the  $B_2$  and  $B_3$  configurations show higher drag, due to a bow shock near the nosecone, producing a high pressure stagnation region. This high pressure region integrated over the nosecone increases the overall drag force. Additionally, the  $B_3$  configuration has a negative drag component that is integrated on the capped nozzle face that is modeled as a solid wall surface. Hence, this term reduces drag, as it acts in the opposite direction. To correctly account for propulsion effects, the

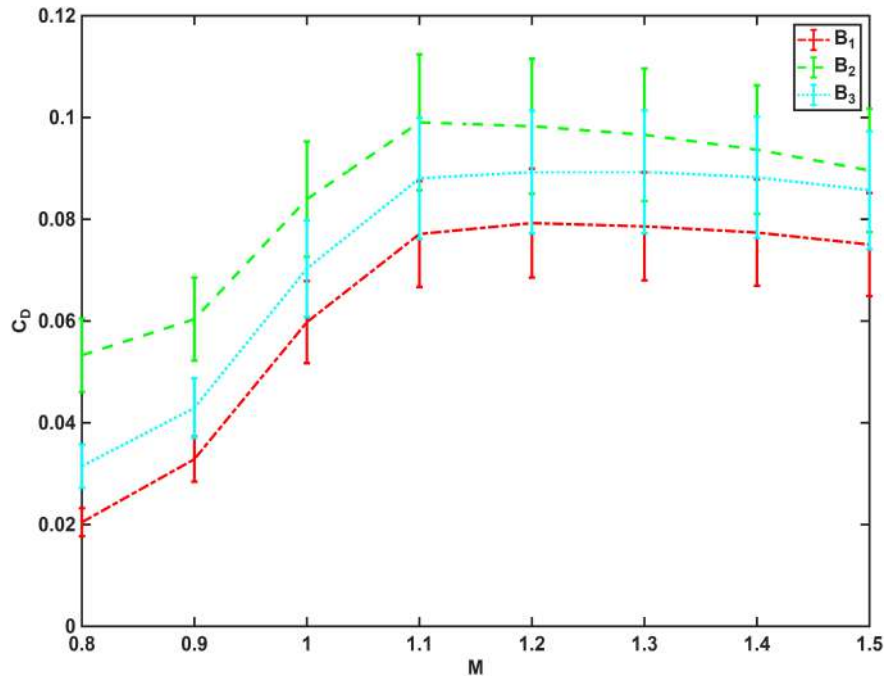


Figure 5.12: Comparison of drag between configurations

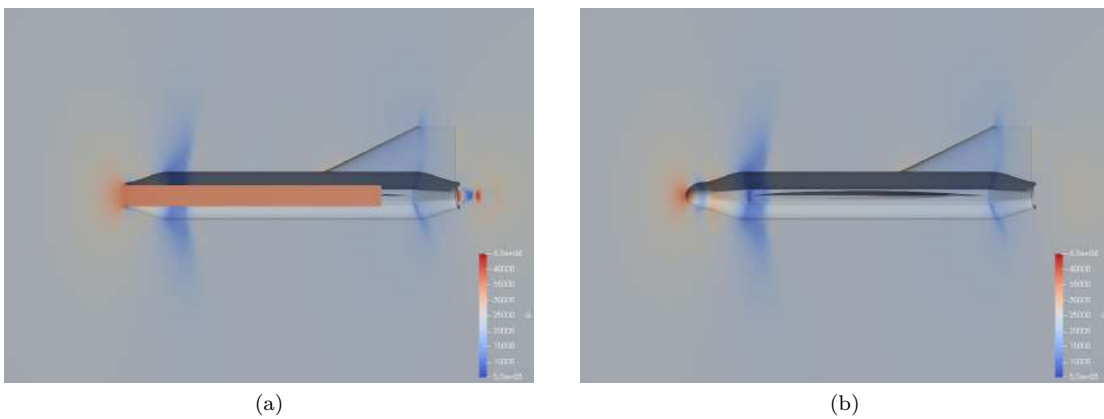


Figure 5.13: Pressure contours  $M = 0.9$  (a)  $B_1$  (b)  $B_3$

forces on the nose cone and the capped face of the nozzle should be corrected analytically to get the drag values close to  $B_1$ .

### 5.3 Exhaust Correction

Most available, low- and medium-fidelity software, such as DATCOM, PANAIR, AVL, and OpenVSP, model the SSUAV and similar aircraft geometries as a closed solid surface. This approach is similar to the  $B_3$  configuration that is simulated. Hence, the force on the capped nozzle face, which acts against the drag as mentioned in the previous section, is a non-essential drag component that needs to be corrected. The exhaust correction stated in Section 3.3.2, is utilized to correct for the capped nozzle face. This component of drag works against the total drag force; therefore, the drag values of the  $B_3$  configuration are expected to increase after correction of the capped nozzle. The drag for configurations  $B_3$ ,  $B_2$ , and  $B_4$  is plotted in Figure 5.14. The integrated pressure force on the capped nozzle is removed from the  $B_3$  drag values. The drag values of configuration  $B_2$  and corrected configuration  $B_4$  are nearly the same ( $< 2\%$ ) for all Mach numbers. This signifies that incorrect integrated pressure values have a significant effect on the external drag of the SSUAV. The increase in drag values is up to 60%, which significantly affects the aerodynamic characteristics of the SSUAV. This in turn can affect the design and development of the SSUAV.

### 5.4 Intake Correction

Conducting CFD simulations for different propulsion and aerodynamic parameters to study their effect on the aeropropulsive characteristics of the SSUAV will require a significant amount of simulations, accounting for different altitudes and speeds. The geometry can be modeled with a nose cone to isolate the propulsion system and only calculate the forces on the external body. Further adding the propulsion effects using analytical methods can help in reducing the amount of simulations. The accuracy of the approach must be analyzed before using such an techniques.

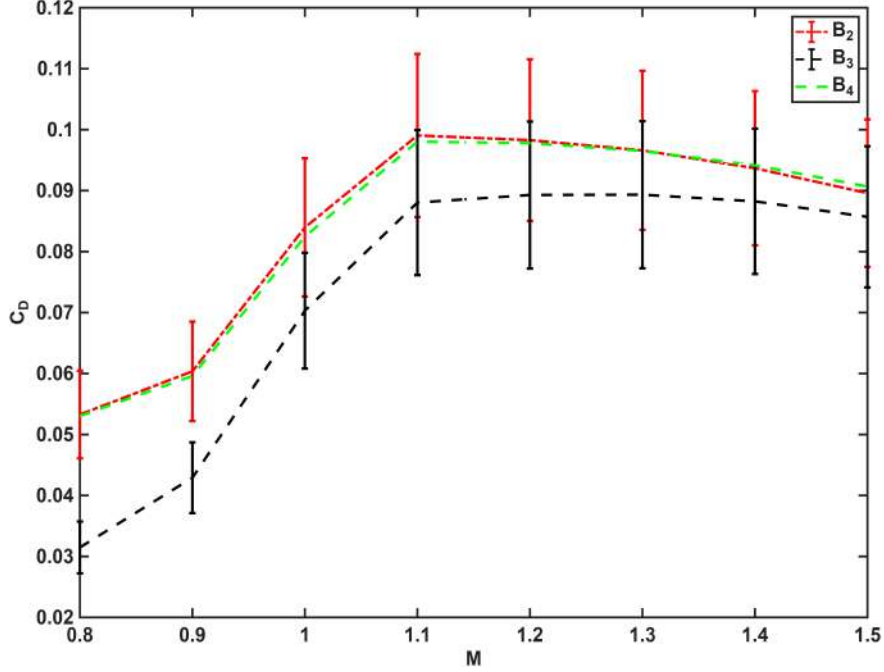


Figure 5.14: Comparison of drag between  $B_3$ ,  $B_4$  and  $B_2$

The configurations  $B_2$  and  $B_3$ , are modeled with a nosecone, hence, as stated earlier, the high pressure stagnation region on the nosecone contributes to an additional term for the total drag force. This term needs to be corrected because this term is already included in the thrust equation on the engine intake face. Calculating the total drag force for the SSUAV without the pressure term included in the thrust equation is necessary to perform rapid predictions of the aeropropulsive performance of the SSUAV using different engine parameters and drag values by simplifying the geometry. The intake correction is applied to the  $B_4$  configuration, using the methodology in Section 3.3.1.

The intake corrected configuration  $B_5$  is plotted against  $B_3$  and the simulated CFD configuration  $B_1$ , in Figure 5.15. Only external drag coefficients are compared since the drag contribution of the propulsion system is taken into account in the thrust equation. The pressure corrected inside the SSUAV that utilizes the Fanno flow pressure is not utilized in the low- and medium-fidelity software and should be modeled analytically.

The drag values of the intake corrected configuration  $B_5$  have shown only a 10% deviation from the simulated configuration  $B_1$ . Hence, the drag calculated without the intake, by

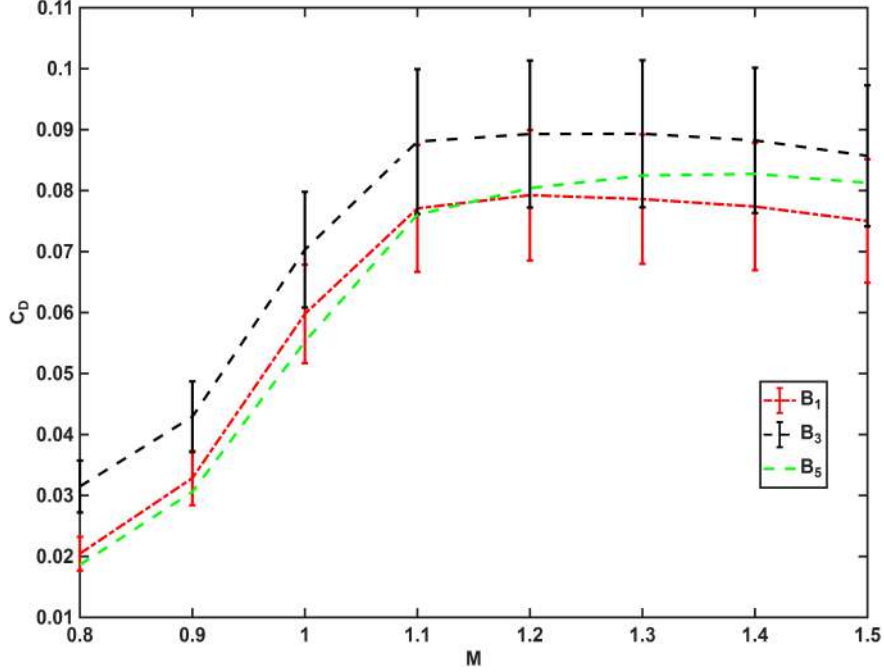


Figure 5.15: Drag comparison between  $B_1$ ,  $B_3$  and  $B_5$

modeling a nose-cone forebody and with a capped nozzle, can be corrected to get closer values approaching drag values of high-fidelity simulations that include propulsion effects with external aerodynamics. Since the modeled correction only utilizes analytical and geometrical parameters, computationally expensive methods compared to analytical methods such as CFD can be avoided. The corrected drag values can be utilized directly with the propulsion and external aerodynamic parameters such as Fanno flow pressure and freestream pressure, to accurately model the total net force of the SSUAV. Although the error is small, but as observed in Figure 5.15, the drag values of configuration  $B_5$  deviates from configuration  $B_1$  for higher Mach numbers. Similarly, the drag is underpredicted for Mach numbers less than 1.1, and this absolute error in drag for the  $B_5$  configuration, for lower drag values, will be significant. More research of the corrected drag force is needed to get better insight into the accuracy of the analytical model.

The pressure on the intake lip of the  $B_1$  configuration should be compared with the analytical pressure described in Section 3.3.1, to understand the reason for the under and overprediction of the drag values in the Mach numbers. A non-dimensionalized distance  $j$ ,

using the total arc length of the lip, is used from the top of the intake lip as shown in Figure 5.17. The comparison between the analytically modeled pressure in the SSUAV intake and the CFD calculated pressure at  $M = 0.9$  for configuration  $B_1$  is plotted in Figure 5.16. The constant freestream pressure modeled on the lip to account for the force contributed by the freestream pressure ( $22632.1 Pa$ ) is higher than the CFD pressure as shown in Figure 5.18. Similarly, the Fanno flow pressure modeled inside the SSUAV actually underpredicts the actual pressure values when compared with CFD. The region of  $j = 0.6$  shows a pressure peak that was not modeled in the correction. This region is a stagnation region, caused by spillage of the flow. To better understand spillage, the streamlines are plotted for  $M = 0.9$  in Figure 5.17. The region  $j = 0.6$  lies between the free stream and the SSUAV stream tube. This point shows that some flow is turning back into the freestream, and the rest of the flow is moving inside the SSUAV. This stagnation region caused an increase in static pressure on the lip that was not modeled in the analytical correction. The combined effect of the modeled freestream pressure, which overpredicts the pressure, and the Fanno-flow pressure inside the SSUAV, which underpredicts the pressure on the lip, causes an overall underprediction of the drag.

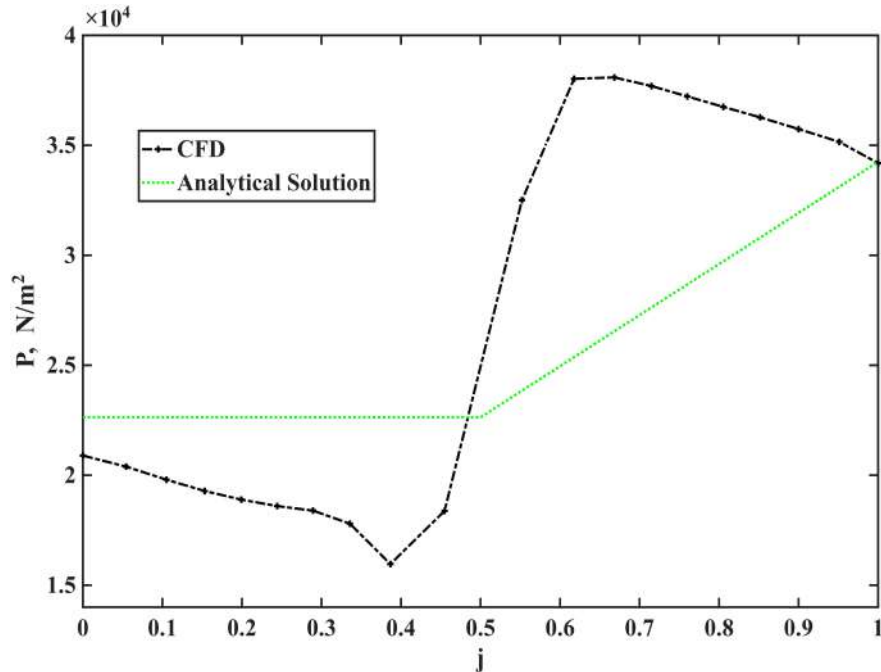


Figure 5.16: Comparison of analytical vs CFD computed pressure plot on intake lip,  $M = 0.9$

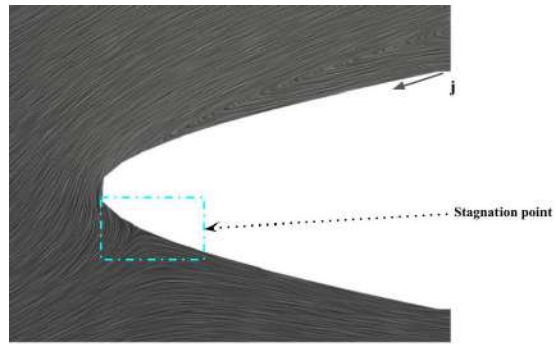


Figure 5.17: Stagnation point and spillage for  $M=0.9$

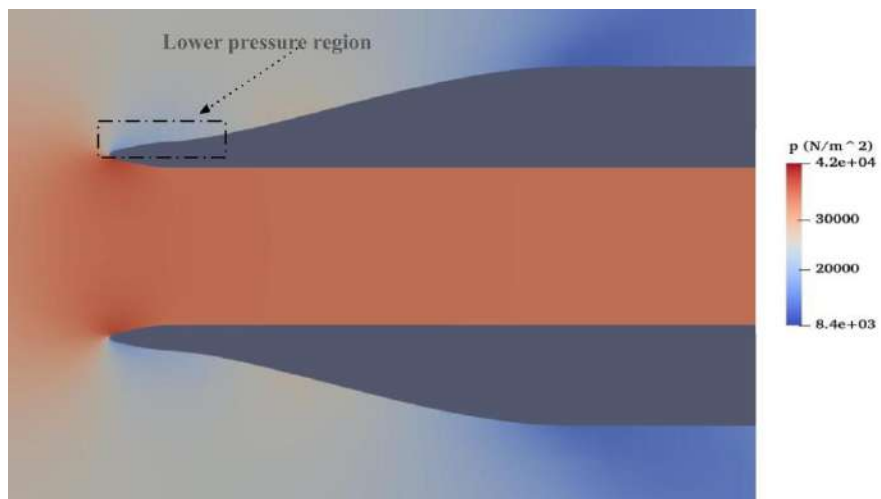


Figure 5.18: Pressure contours for  $M = 0.9$

Mach numbers higher than 1.1 show overprediction of drag for the  $B_5$  configuration compared to the  $B_1$  configuration. Similarly, the analytical pressure utilized for  $M = 1.5$  is compared with the pressure obtained from the CFD simulations in Figure 5.19. For  $M = 1.5$ , a stagnation region develops in a manner similar to the  $M = 0.9$  case, with the stagnation point again occurring at  $j = 0.6$ . In the  $M = 1.5$  case, the overprediction observed for higher Mach numbers is caused by the region modeled between  $j = 0$  and  $j = 0.5$ . The stagnation region present for both Mach numbers signifies, a better modelling of the lip is required. Hence, the CFD simulations conducted for intake geometry, helped in improving the analytical model by showing two distinct region (before and after the stagnation point) which needs to be modeled, instead of assuming a constant and varying pressure on each half of the lip. For  $M = 0.9$ , this region was relatively small, whereas, for  $M = 1.5$ , this region shows a much lower pressure than the freestream pressure, as shown in Figure 5.18. As stated previously, the combined effect of these two regions contributed to the deviation in drag. Since, for  $M = 1.5$  the region that is modeled by the freestream pressure shows an over-predicted pressure between the obtained CFD and the analytically modeled pressure, in general, the drag is over-predicted for  $M = 1.5$ .

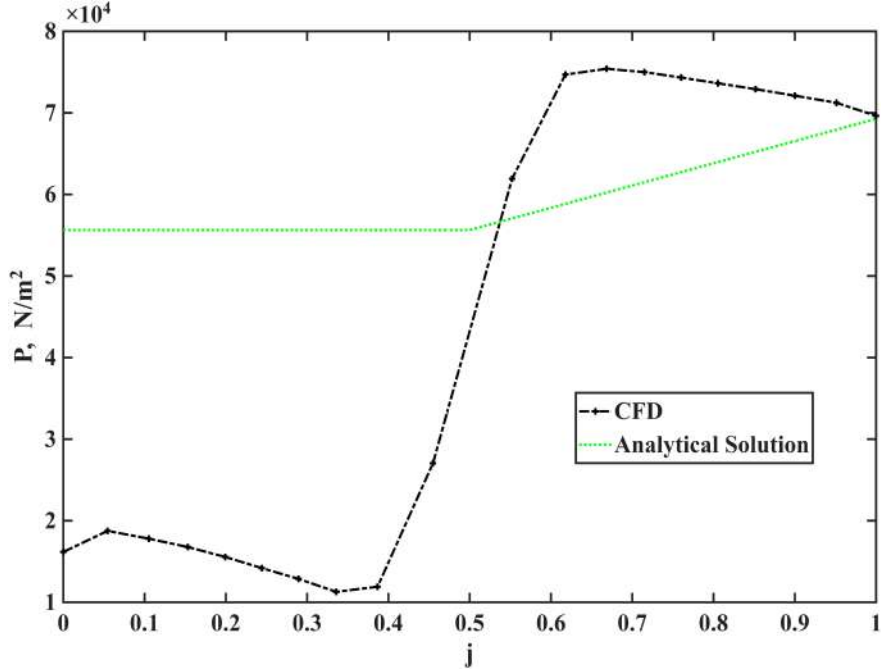


Figure 5.19: Comparison of analytical vs CFD computed pressure plot on intake lip,  $M=1.5$

#### 5.4.1 Engine Thrust

The engine thrust is calculated as presented in Section 3.2.4. The error between the CFD simulations of  $B_1$  and the analytical model is less than 4%, for the mass flow rate and the thrust of the engine. The comparison between CFD and the analytical engine model is shown in Figure 5.20. The error is lowest for Mach 0.9 ( $\approx 1.5\%$ ) and highest for Mach 1.5 ( $\approx 3.5\%$ ). This agreement was expected between the analytical thrust and the CFD-calculated thrust, as the fixed condition was applied to the engine face, which limited the static and total pressure in the tube. Similarly, Fanno-flow is also based on conservation of mass, momentum and energy, which CFD also utilizes; this in turn made the thrust predictions much accurate, while at the junction of stream tube and freestream, the pressure showed deviation as seen in previous section. Since small angle of attacks are considered in the study, the one-dimensional code produces similar results for all the angles. For larger angle of attacks better formulations for back pressure calculation accounting for velocities in other orthogonal directions are needed. This comparison provides insight that a similar procedure can be used to model geometries without an intake to produce similar propulsion

effects.

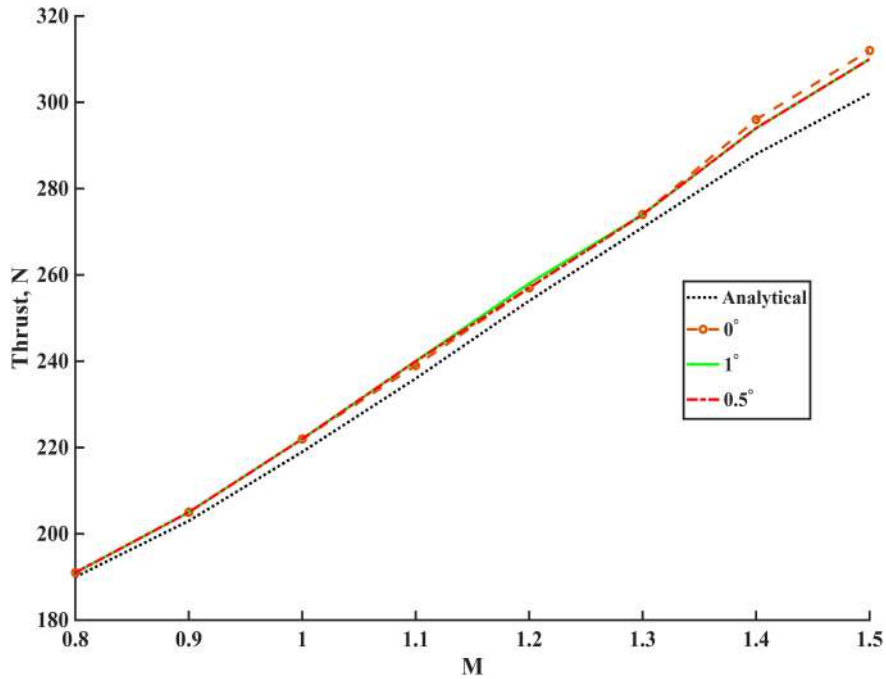


Figure 5.20: Comparison between analytical and CFD computed thrust

#### 5.4.2 Top Speed and stable flight

The net force across Mach numbers are curve fitted using a quadratic polynomial and optimized for top speed and stable flight angle at top speed. The weight assumed for the UAV is 100 kg, the margin between lift and weight and drag and thrust is assumed to be a function of Mach number as shown in Section 3.3.3. The top speeds of the  $B_5$  and  $B_1$  configurations are presented in Table 5.3. The maximum speed for both configurations shows a deviation

Table 5.3: Top speed and stable angle

	M	AOA
$B_5$	0.8517	0.4567
$B_1$	0.8434	0.4464

of  $< 1\%$ , while the angle of attack for stable flight shows a higher deviation ( $< 2.3\%$ ) due to the difference in lift values for the  $B_3$  configuration which were not corrected using any analytical relation. The deviation in lift between  $B_1$  and  $B_3$  is relatively low across the angle of attacks and Mach numbers compared to the drag. Hence, after correcting  $B_3$  for exhaust

and intake, the maximum speed and angle of attack are very close.

## 5.5 Summary

The simulation carried out for  $B_1$  configurations includes the combined effect of the propulsion system and external aerodynamics. The drag and lift values of the configuration were analyzed across the angle of attacks and Mach number to study the behavior in the transonic regime. The lift reduces after Mach 1 due to the formation of the shock. The drag peaks around Mach 1.1. The lift increased with the angle of attack, while the drag showed an insignificant deviation. The behaviour was also observed for the  $B_2$  and  $B_3$  (producing  $B_4$ ) configurations as well. The plume affects the lift between the  $B_2$  and  $B_3$  configurations by increasing the pressure on the top surface of the UAV around the boattail. Drag values differ between configurations because of the nosecone and the modeling of propulsion independently. The exhaust correction implemented for  $B_3$  gives a similar drag to  $B_2$  because the forward force acting on the solid face is subtracted. Furthermore, an intake correction for the nose-cone configuration was implemented by analytically modeling the lip of the UAV intake as an isosceles triangle. Assuming constant pressure outside the UAV, and linearly increasing pressure from freestream to fanno-flow tube. The drag predicted by the correction is close to the drag configuration  $B_1$  calculated using CFD. The numerical correction gives similar drag values, but the pressure distribution varies both inside and outside the UAV. The spillage must be considered for further modeling. The top speed and stable angle of attack at the top speed are calculated for the corrected configuration as well as the calculated CFD configuration.

The corrections applied, using a low-fidelity method on the CFD results for a simplified forebody geometry, have led to a significant improvement in drag prediction accuracy. This suggests that low-fidelity methods can be utilized to correct for intake and exhaust, to speed up the initial design phase of the SSUAV. This can reduce a large number of iterations without compromising accuracy.

## Chapter 6

# Conclusions and Recommendations

The MUFASA B.1 SSUAV (small-scale unmanned aerial vehicle) configuration was evaluated to assess the applicability of low-fidelity aeropropulsive methods for rapid mission and trajectory analysis in tools such as SUAVE (Stanford University Aerospace Vehicle Environment). Due to its large central intake, propulsion strongly influences both external aerodynamics and net thrust–drag characteristics. Baseline low-fidelity approaches, which replace the intake with solid nose or pass-through geometries (as in configuration  $B_3$ ), showed drag deviations of 13–50% across Mach number and angle of attack when compared with OpenFOAM CFD. These discrepancies arise from unmodeled propulsion–airframe interactions, particularly spillage and plume effects.

Analytical corrections were developed to address these limitations. Removal of the solid exhaust face in the  $B_3$  approximation, along with nose cone corrections, significantly reduced the drag prediction error. Adding Fanno flow pressure in the corrections further improved the estimates, reducing the underprediction below Mach 1.1 and the overprediction above Mach 1.1 to within 10% of CFD results. The lift deviations observed under some conditions also indicate the influence of the plume on external aerodynamics absent from the baseline methods.

The resulting corrected low-fidelity model enables faster and more accurate prediction of aeropropulsive performance for MUFASA B.1. This approach extends to similar SSUAV

geometries, providing improved fidelity for rapid design and trajectory evaluation without full CFD dependence.

# Bibliography

- AMT Netherlands Lynx. (2020). Lynx gas turbine.
- Anderson, J. (2011). *Fundamentals of aerodynamics*.
- Araya, G. (2019). Turbulence model assessment in compressible flows around complex geometries with unstructured grids. *Fluids*, 4(2), 81.
- Atik, H., Basoglu, O., Erdem, B., Ilgaz, M., Karbancioglu, I., Katirci, A., Mahmutyazicioglu, E., & Yalcin, L. (2008). Prediction capabilities and comparison of panel, semi-empiric and cfd codes for missile aerodynamic analyses. *26th AIAA Applied Aerodynamics Conference*, 6224.
- Atmosphere, U. S. (1976). *Us standard atmosphere*. National Oceanic; Atmospheric Administration.
- Barbosa, L. M. F., Maciel, F. M. O., & de Barros, J. E. M. (2014). *Study of unmanned supersonic aircraft configuration* (tech. rep.). SAE Technical Paper.
- Barton, J. T., & Pulliam, T. H. (1986). Airfoil computation at high angles of attack, inviscid and viscous phenomena. *AIAA journal*, 24(5), 705–712.
- Bravo-Mosquera, P., Muñoz, H., Darío, C., & Catalano, F. (2016). Analytical and numerical design of a mixed-compression air intake for a supersonic fighter aircraft. *1o SiPGEM 1o Simpòsio do Programa de Pós-Graduação em Engenharia Mecânica*.
- Briones, A. M., Caswell, A. W., & Rankin, B. A. (2021). Fully Coupled Turbojet Engine Computational Fluid Dynamics Simulations and Cycle Analyses Along the Equilibrium Running Line. *Journal of Engineering for Gas Turbines and Power*, 143(6), 061019. <https://doi.org/10.1115/1.4049410>
- Burdette, D. A., & Martins, J. R. R. A. (2019). Impact of Morphing Trailing Edges on Mission Performance for the Common Research Model. *Journal of Aircraft*, 56(1), 369–384. <https://doi.org/10.2514/1.C034967>
- Cai, G., Dias, J., & Seneviratne, L. (2014). A Survey of Small-Scale Unmanned Aerial Vehicles: Recent Advances and Future Development Trends. *Unmanned Systems*, 02(02), 175–199. <https://doi.org/10.1142/S2301385014300017>

- Campbell, J. F. (1976). Augmentation of Vortex Lift by Spanwise Blowing. *Journal of Aircraft*, 13(9), 727–732. <https://doi.org/10.2514/3.58703>
- Chou, P.-Y. (1945). On velocity correlations and the solutions of the equations of turbulent fluctuation. *Quarterly of applied mathematics*, 3(1), 38–54.
- Clancy, L. J. (1975). *Aerodynamics*.
- Dalman, B. (2021). *Conceptual design methods for small-scale supersonic uncrewed aerial vehicles* [Master's thesis]. University of Calgary.
- Deardorff, J. W. (1970). A numerical study of three-dimensional turbulent channel flow at large reynolds numbers. *Journal of Fluid Mechanics*, 41, 453–480. <https://doi.org/10.1017/S0022112070000691>
- Devan, L., Sun, J., & Moore, F. (1979). Aerodynamic prediction code for tactical weapons. *17th Aerospace Sciences Meeting*. <https://doi.org/10.2514/6.1979-361>
- Durante, B. J. (2023). *Flying and handling qualities of small-scale supersonic uncrewed aerial vehicles* [Master's thesis]. University of Calgary. <https://dx.doi.org/10.11575/PRISM/40789>
- Elmer, K., Welge, H., Salamone, J., & Cowart, R. (2013). SCAMP: Supersonic Passenger Transport Transonic Acceleration Flight Profiles with Considerations of Focused Sonic Boom. *51st AIAA Aerospace Sciences Meeting including the New Horizons Forum and Aerospace Exposition*. <https://doi.org/10.2514/6.2013-1065>
- Farokhi, S. (2014). *Aircraft Propulsion*.
- Fox, R. W., & Kline, S. J. (1962). Flow Regimes in Curved Subsonic Diffusers. *Journal of Basic Engineering*, 84(3), 303–312. <https://doi.org/10.1115/1.3657307>
- Fyfe, R. L. (2025). *Low-Speed Flight Testing and System Identification of a Small-Scale Supersonic Uncrewed Aerial Vehicle* [Master's thesis]. University of Calgary.
- Gair, S. R. (2023). *Manufacture, refinement and low-speed flight testing of a small-scale, high-speed uncrewed aerial vehicle* [Master's thesis]. University of Calgary. <https://dx.doi.org/10.11575/PRISM/41705>
- Garcia, A., Fyfe, R. L., Korobenko, A., & Johansen, C. T. (2024). Design and testing of the multipurpose uncrewed fixed-wing advanced supersonic aircraft. *AIAA AVIATION FORUM AND ASCEND 2024*. <https://doi.org/10.2514/6.2024-4332>
- Ghoreyshi, M., Da Ronch, A., Badcock, K., Dees, J., Berard, A., & Rizzi, A. (2009). Aerodynamic Modelling for Flight Dynamics Analysis of Conceptual Aircraft Designs. *27th AIAA Applied Aerodynamics Conference*. <https://doi.org/10.2514/6.2009-4121>
- Glauert, H. (1928). The effect of compressibility on the lift of an aerofoil. *Proceedings of the Royal Society of London. Series A, Containing Papers of a Mathematical and Physical Character*, 118(779), 113–119.

- Goorjian, P. M. (1988). *A streamwise upwind algorithm for the euler and navier-stokes equations applied to transonic flows* (tech. rep.).
- Goulos, I., Pachidis, V., Celis, C., D'Ippolito, R., & Stevens, J. (2010). Simulation Framework Development for Aircraft Mission Analysis. *Volume 1: Aircraft Engine; Ceramics; Coal, Biomass and Alternative Fuels; Education; Electric Power; Manufacturing Materials and Metallurgy*, 341–351. <https://doi.org/10.1115/GT2010-23379>
- Gounko, Y., Mazhul, I. I., & Kharitonov, A. M. (2013). Aerodynamic design and experimental modelling of an innovative supersonic three-dimensional air-intake. *The Aeronautical Journal*, 117(1192), 559–584. <https://doi.org/10.1017/S0001924000008216>
- Greenshields, C. J., Weller, H. G., Gasparini, L., & Reese, J. M. (2010). Implementation of semi-discrete, non-staggered central schemes in a colocated, polyhedral, finite volume framework, for high-speed viscous flows. *International Journal for Numerical Methods in Fluids*, 63(1), 1–21. <https://doi.org/https://doi.org/10.1002/fld.2069>
- Guimarães, T. A., Cesnik, C. E., & Kolmanovsky, I. (2021). Low speed aerodynamic modeling for control-related considerations in supersonic aircraft design. *AIAA Aviation 2021 Forum*, 2531.
- Hanjalić, K., & Launder, B. E. (1972). A Reynolds stress model of turbulence and its application to thin shear flows. *Journal of Fluid Mechanics*, 52(4), 609–638. <https://doi.org/10.1017/S002211207200268X>
- Hassanalain, M., & Abdelkefi, A. (2017). Classifications, applications, and design challenges of drones: A review. *Progress in Aerospace Sciences*, 91, 99–131. <https://doi.org/10.1016/j.paerosci.2017.04.003>
- Hearn, T. A., Hendricks, E., Chin, J., & Gray, J. S. (2016). Optimization of Turbine Engine Cycle Analysis with Analytic Derivatives. *17th AIAA/ISSMO Multidisciplinary Analysis and Optimization Conference*. <https://doi.org/10.2514/6.2016-4297>
- Henne, P. (2003). The Case for Small Supersonic Civil Aircraft. *AIAA International Air and Space Symposium and Exposition: The Next 100 Years*. <https://doi.org/10.2514/6.2003-2555>
- Honda, K., Yoshida, N., & Carbone, M. (2016). Multiparty asynchronous session types. *Journal of the ACM (JACM)*, 63(1), 1–67.
- Hooker, J. R., Wick, A., Zeune, C. H., & Agelastos, A. (2013). Over Wing Nacelle Installations for Improved Energy Efficiency. *31st AIAA Applied Aerodynamics Conference*. <https://doi.org/10.2514/6.2013-2920>
- Ishikawa, H., Kwak, D.-Y., & Yoshida, K. (2008). Numerical Analysis on Flight-Test Results of Supersonic Experimental Airplane NEXST-1. *Journal of Aircraft*, 45(5), 1505–1513. <https://doi.org/10.2514/1.33595>

- Jameson, A., & Baker, T. (1987). Improvements to the aircraft Euler method. *25th AIAA Aerospace Sciences Meeting*. <https://doi.org/10.2514/6.1987-452>
- Jasa, J. P., Mader, C. A., & Martins, J. R. R. A. (2018). Trajectory Optimization of a Supersonic Aircraft with a Thermal Fuel Management System. *2018 Multidisciplinary Analysis and Optimization Conference*. <https://doi.org/10.2514/6.2018-3884>
- Jones, R. T. (1956). *Theory of wing-body drag at supersonic speeds* (tech. rep.).
- Jones, S. M. (2007). *An introduction to thermodynamic performance analysis of aircraft gas turbine engine cycles using the numerical propulsion system simulation code* (tech. rep.).
- Jones, W., & Launder, B. (1972). The prediction of laminarization with a two-equation model of turbulence. *International Journal of Heat and Mass Transfer*, *15*(2), 301–314. [https://doi.org/10.1016/0017-9310\(72\)90076-2](https://doi.org/10.1016/0017-9310(72)90076-2)
- Karino, H., Yairi, T., Ninomiya, T., & Hori, K. (2020). Estimating Aerodynamic Coefficients from Uncertain Data of D-SEND Aircraft with Gaussian Process Regression. *Transactions of the Japan Society for Aeronautical and Space Sciences*, *63*(6), 257–264. <https://doi.org/10.2322/tjsass.63.257>
- Kawaguchi, J., Suzuki, H., Ninomiya, T., & Tomita, H. (2017). Post-flight Evaluation of the Guidance and Control for D-SEND#2 2nd Drop Test. *AIAA Atmospheric Flight Mechanics Conference*. <https://doi.org/10.2514/6.2017-0939>
- Kestner, B., Nam, T., Flett, A., Wilson, J., & Mavris, D. (2012). Integrated Engine and Aircraft Mission Performance Analysis Using NPSS. *50th AIAA Aerospace Sciences Meeting including the New Horizons Forum and Aerospace Exposition*. <https://doi.org/10.2514/6.2012-841>
- Kline, S. J. (1959). On the Nature of Stall. *Journal of Basic Engineering*, *81*(3), 305–319. <https://doi.org/10.1115/1.4008459>
- Koeck, C. (1985). Computation of three-dimensional flow using the Euler equations and a multiple-grid scheme. *International Journal for Numerical Methods in Fluids*, *5*(5), 483–500. <https://doi.org/10.1002/flf.1650050507>
- Kraposhin, M., Bovtrikova, A., & Strijhak, S. (2015). Adaptation of kurganov-tadmor numerical scheme for applying in combination with the piso method in numerical simulation of flows in a wide range of mach numbers. *Procedia Computer Science*, *66*, 43–52.
- Kraposhin, M. V., Banholzer, M., Pfitzner, M., & Marchevsky, I. K. (2018). A hybrid pressure-based solver for nonideal single-phase fluid flows at all speeds. *International Journal for Numerical Methods in Fluids*, *88*(2), 79–99. <https://doi.org/10.1002/flf.4512>
- Langelaan, J. (2007). Long Distance/Duration Trajectory Optimization for Small UAVs. *AIAA Guidance, Navigation and Control Conference and Exhibit*. <https://doi.org/10.2514/6.2007-6737>

- Langston, S. (2015). Low-Speed Stability and Control of Exploratory Tailless Long-Range Supersonic Configurations.
- Langston, S., Nelson, C. P., & Livne, E. (2016). Low-Speed Stability and Control of a Reduced Scale Long-Range Supersonic Configuration with Reduced-Size or No Vertical Tail. *AIAA Atmospheric Flight Mechanics Conference*. <https://doi.org/10.2514/6.2016-1036>
- Lastiwka, D., Korobenko, A., & Johansen, C. T. (2022). Validation and Verification of pimpleCentralFOAM and a 1D-ERAM Solver for Analysis of an Ejector-Ramjet. *AIAA AVIATION 2022 Forum*. <https://doi.org/10.2514/6.2022-3347>
- Leblic, S., Edwards, J., & Johansen, C. T. (2025). Optimal trajectories for two configurations of a small-scale supersonic uncrewed aerial vehicle [Presented at EUCASS 2025]. *Proceedings of the 11th European Conference for Aeronautics and Aerospace Sciences (EUCASS)*.
- Lee, M., & Ho, C.-M. (1990). Lift force of delta wings. *Applied Mechanics Reviews*, 43(9), 209–221.
- Lemmon, E. W., Bell, I. H., Huber, M., & McLinden, M. (2018). Nist standard reference database 23: Reference fluid thermodynamic and transport properties-refprop, version 10.0, national institute of standards and technology. *Standard Reference Data Program, Gaithersburg*, 45–46.
- Levin, D., & Katz, J. (1981). Vortex-Lattice Method for the Calculation of the Nonsteady Separated Flow over Delta Wings. *Journal of Aircraft*, 18(12), 1032–1037. <https://doi.org/10.2514/3.57596>
- Li, W., Shields, E., & Geiselhart, K. (2010). A Mixed-Fidelity Approach for Design of Low-Boom Supersonic Aircraft. *48th AIAA Aerospace Sciences Meeting Including the New Horizons Forum and Aerospace Exposition*. <https://doi.org/10.2514/6.2010-845>
- Litt, J. S. (2018). Toolbox for the modeling and analysis of thermodynamic systems (t-mats) users' workshop presentations. *Toolbox for the Modeling and Analysis of Thermodynamic Systems (T-MATS) Users Workshop*, (E-19488).
- Livne, E., & Nelson, C. (2012). From blank slate to flight ready new small research uavs in twenty weeks - undergraduate airplane design at the university of washington. *50th AIAA Aerospace Sciences Meeting including the New Horizons Forum and Aerospace Exposition*. <https://doi.org/10.2514/6.2012-845>
- Mavriplis, N., Ting, K.-Y., Moustafa, A., Hill, C., Soltani, R., Nelson, C. P., & Livne, E. (2022). Supersonic Configurations at Low Speeds (SCALOS): Test / Simulation Correlation Studies. *AIAA SCITECH 2022 Forum*. <https://doi.org/10.2514/6.2022-1801>
- Meerts, C., Steelant, J., & Hendrick, P. (2011). Preliminary design of the low speed propulsion air intake of the lapcat-mr2 aircraft. *7th European Symposium on Aerothermodynamics, number ESA-SP-692 in ESA Special Publications, European Space Agency*.

- Menter, F. R. (1994). Two-equation eddy-viscosity turbulence models for engineering applications. *AIAA journal*, 32(8), 1598–1605.
- Menter, F. R., Kuntz, M., Langtry, R., et al. (2003). Ten years of industrial experience with the sst turbulence model. *Turbulence, heat and mass transfer*, 4(1), 625–632.
- Menter, F. (1993). Zonal two equation kw turbulence models for aerodynamic flows. *23rd fluid dynamics, plasmadynamics, and lasers conference*, 2906.
- Messa, T. (2018). *A comparison between pressure-based and density-based solvers in openfoam applied to the expansion in supersonic nozzles* [Master's thesis]. Politecnico di Milano.
- Miettinen, A., & Siikonen, T. (2015). Application of pressure- and density-based methods for different flow speeds. *International Journal for Numerical Methods in Fluids*, 79(5), 243–267. <https://doi.org/10.1002/flid.4051>
- Migadel, T. (2024). *Turbulent Combustion Modeling of an Ejector Ramjet Propulsion System* [Master's thesis]. University of Calgary.
- Moens, F., & Gardarein, P. (2001). Numerical simulation of the propeller/wing interactions for transport aircraft. *19th AIAA Applied Aerodynamics Conference*. <https://doi.org/10.2514/6.2001-2404>
- Moura, A., & Rosa, M. (2013). A computer program for calculating normal and oblique shock waves for airflows in chemical and thermodynamic equilibrium. <https://doi.org/10.13140/2.1.1737.0243>
- Nelson, C. P., Ting, K.-Y., Mavriplis, N., Soltani, R., & Livne, E. (2022). Supersonic Configurations at Low Speeds (SCALOS): Project Background and Progress at University of Washington. *AIAA SCITECH 2022 Forum*. <https://doi.org/10.2514/6.2022-1803>
- Oates, G. C. (1985). *Aerothermodynamics of aircraft engine components*. AIAA.
- Ohnuki, T., Hirako, K., & Sakata, K. (2006). National experimental supersonic transport project. *Proceedings on 25th International Council of the Aeronautical Sciences*, 2006–1.
- Orszag, S. A. (1970). Analytical theories of turbulence. *Journal of Fluid Mechanics*, 41(2), 363–386. <https://doi.org/10.1017/S0022112070000642>
- Perez, R., Henderson, R., & Martins, J. R. R. A. (2008). Multidisciplinary Design Optimization of Airframe and Engine for Emissions Reduction. *12th AIAA/ISSMO Multidisciplinary Analysis and Optimization Conference*. <https://doi.org/10.2514/6.2008-6014>
- Polhamus, E. C. (1953). *Drag due to lift at mach numbers up to 2.0*. National Advisory Committee for Aeronautics.
- Polhamus, E. C. (1971). Predictions of vortex-lift characteristics by a leading-edge suction analogy. *Journal of Aircraft*, 8(4), 193–199. <https://doi.org/10.2514/3.44254>

- Prandtl, L. (1925). 7. bericht über untersuchungen zur ausgebildeten turbulenz. *ZAMM - Journal of Applied Mathematics and Mechanics / Zeitschrift für Angewandte Mathematik und Mechanik*, 5, 136–139. <https://doi.org/10.1002/zamm.19250050212>
- Prandtl, L. (1920). *Theory of lifting surfaces* (tech. rep.).
- Raymer, D. (2012). *Aircraft design: A conceptual approach*. American Institute of Aeronautics; Astronautics, Inc.
- Remiger, J., Grois, A., Stöbel, M., Kožulović, D., & Krummenauer, M. (2024). Impact of various intake configurations on the flight mission performance of an unmanned aircraft. *Volume 1: Aircraft Engine*. <https://doi.org/10.1115/GT2024-122647>
- Rettie, I. H., & Lewis, W. G. E. (1968). Design and development of an air intake for a supersonic transport aircraft. *Journal of Aircraft*, 5(6), 513–521. <https://doi.org/10.2514/3.43977>
- Reynolds, O. (1895). Iv. on the dynamical theory of incompressible viscous fluids and the determination of the criterion. *Philosophical transactions of the royal society of london.(a.)*, (186), 123–164.
- Rizzi, A. (1982). Damped Euler-equation method to compute transonic flow around wing-body combinations. *AIAA Journal*, 20(10), 1321–1328. <https://doi.org/10.2514/3.7981>
- Rizzi, A., & Eriksson, L.-E. (1984). Computation of flow around wings based on the Euler equations. *Journal of Fluid Mechanics*, 148, 45–71. <https://doi.org/10.1017/S002211208400224X>
- Roache, P. J. (1994). Perspective: A method for uniform reporting of grid refinement studies. *Journal of Fluids Engineering*, 116(3), 405–413. <https://doi.org/10.1115/1.2910291>
- Rossow, C.-C., Godard, J.-L., Hoheisel, H., & Schmitt, V. (1994). Investigations of propulsion integration interference effects on a transport aircraft configuration. *Journal of Aircraft*, 31(5), 1022–1030. <https://doi.org/10.2514/3.46605>
- Rotta, J. (1951). Statistical theory of inhomogeneous turbulence. *Z. Phys.*, 129, 257–572.
- Schoene, J., KROLL, N., ROSSOW, C., LI, H., & SONAR, T. (1989). A central finite volume tvd scheme for the calculation of supersonic and hypersonic flow fields around complex configurations. *9th Computational Fluid Dynamics Conference*. <https://doi.org/10.2514/6.1989-1975>
- Sepahi-Younsi, J., & Forouzi Feshalami, B. (2019). Performance Evaluation of External and Mixed Compression Supersonic Air Intakes: Parametric Study. *Journal of Aerospace Engineering*, 32(5), 04019066. [https://doi.org/10.1061/\(ASCE\)AS.1943-5525.0001048](https://doi.org/10.1061/(ASCE)AS.1943-5525.0001048)
- Seraj, S., & Martins, J. R. (2022). Aerodynamic shape optimization of a supersonic transport considering low-speed stability. *AIAA Scitech 2022 Forum*, 2177.

- Singh, A., & Mukhopadhyay, S. (2023). Comparison of pressure-based and density-based solvers for scramjet modeling. *Proceedings of the 2nd International Conference on Recent Advances in Fluid and Thermal Sciences 2020 (iCRAFT2020)*, 2584(1), 030007.
- Smagorinsky, J. (1963). GENERAL CIRCULATION EXPERIMENTS WITH THE PRIMITIVE EQUATIONS: I. THE BASIC EXPERIMENT\*. *Monthly Weather Review*, 91(3), 99–164. [https://doi.org/10.1175/1520-0493\(1963\)091<0099:GCEWTP>2.3.CO;2](https://doi.org/10.1175/1520-0493(1963)091<0099:GCEWTP>2.3.CO;2)
- Soban, D., Biezad, D., & Gelhausen, P. (1995). Computer optimization of aircraft handling qualities during preliminary design. *1995 IEEE International Conference on Systems, Man and Cybernetics. Intelligent Systems for the 21st Century*, 3, 2670–2675. <https://doi.org/10.1109/ICSMC.1995.538186>
- Soltani, M. R., Younsi, J. S., Farahani, M., & Masoud, A. (2013). Numerical simulation and parametric study of a supersonic intake. *Proceedings of the Institution of Mechanical Engineers, Part G: Journal of Aerospace Engineering*, 227(3), 467–479. <https://doi.org/10.1177/0954410012436620>
- Spalart, P., & Allmaras, S. (1992). A one-equation turbulence model for aerodynamic flows. *30th aerospace sciences meeting and exhibit*, 439.
- Spalart, P. R. (1997). Comments on the feasibility of les for wings and on the hybrid rans/les approach. *Proceedings of the First AFOSR International Conference on DNS/LES, 1997*, 137–147.
- Squires, K. D. (2004). Detached-Eddy Simulation: Current Status and Perspectives [Series Title: ERCOFTAC Series]. In R. V. A. Oliemans, W. Rodi, R. Friedrich, B. J. Geurts, & O. Métais (Eds.), *Direct and Large-Eddy Simulation V* (pp. 465–480, Vol. 9). Springer Netherlands. [https://doi.org/10.1007/978-1-4020-2313-2\\_49](https://doi.org/10.1007/978-1-4020-2313-2_49)
- Stoldt, H. H. R. (2021). *Verification and Validation of Open-Source Simulation Tools for Supersonic Aircraft Aerodynamic Analysis* [Master's thesis]. University of Calgary.
- Suzuki, H., & Ninomiya, T. (2018, February). Guidance Law Based on Real-time Trajectory Prediction for D-SEND#2. <https://doi.org/10.20637/JAXA-RR-17-010E/0001>
- Ting, K.-Y., Mavriplis, N., Soltani, R., Nelson, C. P., & Livne, E. (2022). Supersonic Configurations at Low Speeds (SCALOS): Model Geometry and Aerodynamic Results. *AIAA SCITECH 2022 Forum*. <https://doi.org/10.2514/6.2022-1800>
- Valorani, M., Nasuti, F., Onofri, M., & Buongiorno, C. (1999). Optimal supersonic intake design for air collection engines (ACE). *Acta Astronautica*, 45(12), 729–745. [https://doi.org/10.1016/S0094-5765\(99\)00185-X](https://doi.org/10.1016/S0094-5765(99)00185-X)
- Vos, R., & Farokhi, S. (2015). *Introduction to Transonic Aerodynamics* (Vol. 110). Springer Netherlands. <https://doi.org/10.1007/978-94-017-9747-4>

- Walter, S., & Starkey, R. (2012). GOJETT: A Supersonic Unmanned Aerial Flight System. *50th AIAA Aerospace Sciences Meeting including the New Horizons Forum and Aerospace Exposition*. <https://doi.org/10.2514/6.2012-22>
- Whitcomb, R. T. (1956). *A study of the zero-lift drag-rise characteristics of wing-body combinations near the speed of sound* (tech. rep.).
- Wick, A. T., Hooker, J. R., & Zeune, C. H. (2015). Integrated Aerodynamic Benefits of Distributed Propulsion. *53rd AIAA Aerospace Sciences Meeting*. <https://doi.org/10.2514/6.2015-1500>
- Wiersema, K., Ting, K.-Y., Nelson, C., & Livne, E. (2025). Supersonic Configurations at Low Speeds(SCALOS): Correlation of CFD and Wind Tunnel Test Results. *AIAA SCITECH 2025 Forum*. <https://doi.org/10.2514/6.2025-2362>
- Wilcox, D. C. (1988). Reassessment of the scale-determining equation for advanced turbulence models. *AIAA Journal*, *26*(11), 1299–1310. <https://doi.org/10.2514/3.10041>
- Williams, M., & Stevens, K. (2006). Computational Prediction of Subsonic Intake Spillage Drag. *24th AIAA Applied Aerodynamics Conference*. <https://doi.org/10.2514/6.2006-3871>
- Xu, X., Gementzopoulos, A., Sedky, G., Jones, A. R., & Lagor, F. D. (2023). Design of optimal wing maneuvers in a transverse gust encounter through iterated simulation or experiment. *Theoretical and Computational Fluid Dynamics*, *37*(4), 465–484. <https://doi.org/10.1007/s00162-023-00659-w>
- Yoshida, K., Yoshikazu, M., & Shimbo, Y. (2002). An Experimental Study on Unmanned Scaled Supersonic Experimental Airplane. *32nd AIAA Fluid Dynamics Conference and Exhibit*. <https://doi.org/10.2514/6.2002-2842>

# Appendix A

## Force Calculation

Aerodynamic forces are usually calculated by integrating the pressure and viscous terms over the desired surface. This can include walls, and boundary faces in the computational domain. Since calculation involves angle of attack simulations, lift and drag forces need to be calculated using specific methods, usually by resolving integrated terms in proposed directions with respect to the flow. Figure A.1 depicts, an airfoil experiencing a flow at an angle  $\alpha$ , a small area element  $dA$  is chosen, the pressure  $P$  and shear stress  $\tau$ , acting normal and along the curve of the airfoil. The integral of the pressure and shear stress terms give the total force on the body, in normal and axial directions.

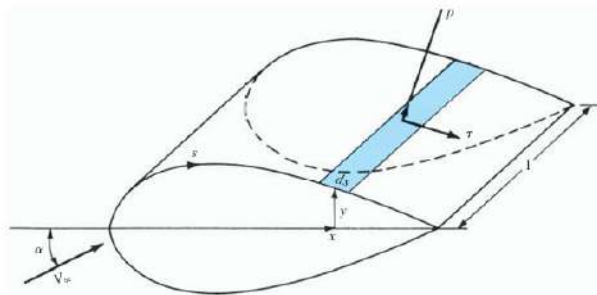


Figure A.1: Aerodynamic force calculation. Reproduced from (Anderson, 2011).

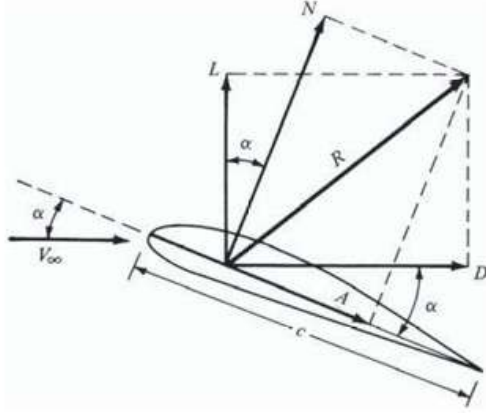


Figure A.2: Force resolution for Drag and Lift adapted from (Anderson, 2011),

## A.1 Lift and Drag

The lift force is generally considered to be perpendicular to the flow, whereas the drag force must lie on the same axis as the incoming flow. With an example of an airfoil represented in fig A.2, a body at an angle  $\alpha$ , can give rise to axial force  $A$  and normal force  $N$ .

By using simple vector resolution the Normal Force  $N$  and the Axial force  $A$  can be used to calculate drag and lift. Hence, the final equation for drag and lift calculation, is derived:

$$L = N \cos \alpha - A \sin \alpha \quad (\text{A.1})$$

$$D = N \sin \alpha + A \cos \alpha$$

## A.2 Aerodynamic Coefficients

The aerodynamic forces are made dimensionless using freestream parameters of the incoming flow. Generally, freestream dynamic pressure is taken as non-dimensionalising quantity for aerodynamic forces. Some non-dimensional aerodynamic coefficients are :

Coefficient of Lift :

$$C_L = \frac{L}{q_\infty} \quad (\text{A.2})$$

Normal force coefficient :

$$C_N = \frac{N}{q_\infty} \quad (\text{A.3})$$

Axial force coefficient :

$$C_A = \frac{A}{q_\infty} \quad (\text{A.4})$$

Coefficient of Drag :

$$C_D = \frac{D}{q_\infty} \quad (\text{A.5})$$

Coefficient of Pitching Moment :

$$C_M = \frac{M}{q_\infty l} \quad (\text{A.6})$$

$q_\infty = \frac{1}{2}\rho_\infty V_\infty^2 A$ ,  $l$  and  $A$  being the reference length and area.

## Appendix B

### Fanno flow

Fanno flow is adiabatic non-reversible flow in a constant area duct. The relation between Mach number, static properties and total properties between two points is determined using a friction factor relationship. The fanno flow relations are:

$$\begin{aligned}\frac{p}{p^*} &= \frac{1}{M} \frac{1}{\sqrt{\left(\frac{2}{\gamma+1}\right) \left(1 + \frac{\gamma-1}{2} M^2\right)}} \\ \frac{\rho}{\rho^*} &= \frac{1}{M} \sqrt{\left(\frac{2}{\gamma+1}\right) \left(1 + \frac{\gamma-1}{2} M^2\right)} \\ \frac{T}{T^*} &= \frac{1}{\left(\frac{2}{\gamma+1}\right) \left(1 + \frac{\gamma-1}{2} M^2\right)} \\ \frac{V}{V^*} &= M \frac{1}{\sqrt{\left(\frac{2}{\gamma+1}\right) \left(1 + \frac{\gamma-1}{2} M^2\right)}} \\ \frac{p_0}{p_0^*} &= \frac{1}{M} \left[ \left(\frac{2}{\gamma+1}\right) \left(1 + \frac{\gamma-1}{2} M^2\right) \right]^{\frac{\gamma+1}{2(\gamma-1)}}\end{aligned}$$

# Appendix C

## Normal Shock Relations

Normal shock is a thin discontinuity present in the flow, across which the property of fluid changes rapidly. The upstream region is shown with subscript 1, and the downstream region of the shock is shown with subscript 2. A shock wave is shown in Figure C.1. The relation between upstream and downstream values is as follows:

$$M_2 = \sqrt{\frac{M_1^2 (\gamma - 1) + 2}{2\gamma M_1^2 - (\gamma - 1)}} \tag{C.1}$$

$$\frac{p_2}{p_1} = \frac{2\gamma M_1^2}{\gamma + 1} - \frac{\gamma - 1}{\gamma + 1} \tag{C.2}$$

$$\frac{\rho_2}{\rho_1} = \frac{(\gamma + 1) M_1^2}{(\gamma - 1) M_1^2 + 2} \tag{C.3}$$

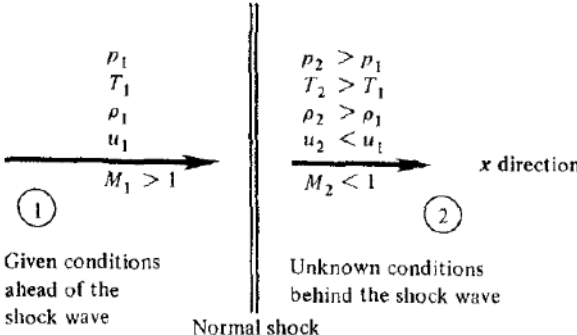


Figure C.1: Normal shock wave. Reproduced from (Moura & Rosa, 2013)

$$\frac{T_2}{T_1} = \frac{\left(1 + \frac{\gamma-1}{2}M_1^2\right) \left(\frac{2\gamma}{\gamma-1}M_1^2 - 1\right)}{M_1^2 \left(\frac{2\gamma}{\gamma-1} + \frac{\gamma-1}{2}\right)} \quad (\text{C.4})$$

$$\frac{p_{0,2}}{p_{0,1}} = \left(\frac{\frac{\gamma+1}{2}M_1^2}{1 + \frac{\gamma-1}{2}M_1^2}\right)^{\frac{\gamma}{\gamma-1}} \left(\frac{1}{\frac{2\gamma}{\gamma+1}M_1^2 - \frac{\gamma-1}{\gamma+1}}\right)^{\frac{1}{\gamma-1}} \quad (\text{C.5})$$

$$T_{0,1} = T_{0,2} \quad (\text{C.6})$$

Where  $\gamma$ ,  $M$ ,  $p$ ,  $p_0$ ,  $T$ , and  $T_0$ , are the ratio of specific heat, Mach number, static pressure, total pressure, temperature, and total temperature.